Inorganic Trace Substances in a Sorption Enhanced Gasification Process and their Removal

Anorganische Spurenstoffe in einem sorptionsunterstützten Vergasungsprozess und ihre Entfernung

Von der Fakultät für Maschinenwesen der Rheinisch-Westfälischen Technischen Hochschule Aachen zur Erlangung des akademischen Grades eines Doktors der Ingenieurwissenschaften genehmigte Dissertation

vorgelegt von

Markus Alexander Kopsch

Berichter: Priv.-Doz. Dr. rer. nat. Michael Müller

Univ.-Prof. Dr.-Ing. Andreas Peschel

Tag der mündlichen Prüfung: 16.12.2024

Diese Dissertation ist auf den Internetseiten der Universitätsbibliothek online verfügbar.

„Speak softly and carry a big stick.“

Theodore Roosevelt

Abstract

The energy supply by biomass, especially by biomass residues, currently enjoys high acceptance among the German population due to the energy crisis. A process that enables the use of biomass residues for power generation is the Ca-looping gasification process proposed in the European GICO-Project. This process requires a hot gas conditioning (HGC) unit for a gasifier and a calciner to remove inorganic trace substances.

To this end, extensive equilibrium calculations with FactSage were conducted for the GICO gasifier (650 °C), and calciner (920 °C), showing that aluminosilicates, Sr-, and Ba-based sorbents could reduce the alkali, respectively sour gas (H_2S/SO_2, HCl) concentration to sub ppm_v levels. Condensation calculations reveal the need for temperature-resistant H_2S sorbents since conventional ones, e.g. Zn_2TiO_4, tend to evaporate, leading to the condensation of unwanted salts, and oxides.

Since the release behavior of inorganic trace species and their adsorptive removal under gasification-like conditions between 650 °C and 700 °C has hardly been investigated, the experimental focus of this work is placed on the gasifier operating at 650 °C.

The release behavior of inorganic trace substances from raw, water-leached, and hydrochar biomass samples was investigated using molecular beam mass spectrometry (MBMS). The sorption capacity of aluminosilicates, alkaline earth, and rare earths-based sorbents was determined by mass spectrometry (MS) in fixed bed lab-scale investigations. The investigations showed that aluminosilicates are suitable for alkali removal. Furthermore, the results indicate that Ca-stabilized Sr- and Ba-sorbents reduce H_2S sufficiently. In both cases, concentrations could be brought below 1 ppm_v.

Compatibility experiments between filter material (Al- and Ca-Mg-silicate fibers) and sorbents were conducted to investigate the possibility of integrating the sorbents into the filter candles in order to allow a more compact HGC design. Since the Zn-sorbents are not reacting with the filter candle material, they can be integrated into the filter candle. However, aluminum- and silicate-phases are formed when using Sr- and Ba-based sorbents leading to potential risks such as the formation of cracks.

Based on the modeling calculations, release, sorption, and compatibility experiments, chemical HGC concepts for different sorbents are proposed.

Kurzfassung

Die Energiebereitstellung durch Biomasse bzw. durch Biomasserückstände genießt derzeit aufgrund der Energiekrise hohe Akzeptanz in der deutschen Bevölkerung. Ein Prozess, welcher die Nutzung von Biomasserückständen als Brennstoffquelle für die Stromerzeugung ermöglicht, ist der derzeit im europäischen GICO-Projekt entwickelte Ca-Looping-Vergasungsprozess. In dieser Arbeit werden Modellierungs- und Versuchsergebnisse zum Freisetzungsverhalten anorganischer Spurenstoffe und zur Sorptionsmittelauswahl zusammengefasst, die zur Entwicklung eines geeigneten Heißgasreinigungskonzepts des Vergasers und Kalzinators verwendet werden können.

Umfangreiche Gleichgewichtsberechnungen mit FactSage für den GICO Vergaser (650 °C) und Kalzinator (920 °C) belegen, dass Alumosilikate und Sr- und Ba-basierte Sorbentien die Konzentration von Alkali- und Sauergasen (H_2S/SO_2, HCl) auf Werte unter 1 ppm_v reduzieren können. Kondensationsberechnungen betonen den Bedarf an temperaturbeständigen H_2S-Sorbentien, da herkömmliche Sorptionsmaterialien, z. B. Zn_2TiO_4, zur Verdampfung neigen. Diese kann im späteren Prozess zur Kondensation von unerwünschten Salzen und Oxiden führen.

Das Freisetzungsverhalten von anorganischen Spurenstoffen aus (un)behandelten Biomassen wurde mittels Molekularstrahl-Massenspektrometrie (MBMS) untersucht. Die Sorptionsgrenzen von Alumosilikaten, Erdalkali- und Seltenerdoxiden nach der Vergasung wurden in Festlaborbettuntersuchungen bei 650 °C mittels Massenspektrometrie (MS) bestimmt. Die Untersuchungen zeigen, dass Alumosilikate für die Alkalientfernung geeignet sind. H_2S kann mittels CaO-stabilisierter SrO- und BaO-Sorbentien ausreichend reduziert werden. Die Konzentrationen werden jeweils unter 1 ppm_v abgesenkt.

Kompatibilitätsexperimente zwischen Filtermaterial (Al- und Ca-Mg-Silikat Fasern) und Sorbentien wurden durchgeführt, um eine mögliche Integration der Sorbentien in die Filterkerze zu untersuchen. Während Zn-Sorbentien in die Filterkerze integriert werden können, da sie nicht mit den Filterkerzenmaterialien reagieren, bilden sich bei Verwendung von Sr- und Ba-Sorbentien Aluminium- und Silikatphasen.

Auf Grundlage der Modellierungsberechnungen, Freisetzungs-, Sorptions- und Kompatibilitätsexperimente werden schließlich chemische Heißgasreinigungskonzepte für verschiedene Sorptionsmittel vorgestellt.

Content

List of figures

List of tables

List of symbols and abbreviations

Symbols

ΔH°_{298}	Standard Enthalpy of Reaction [kJ/mol]
p	Pressure [atm]
t	Time [min]
T	Temperature [°C]
$\dot{V}_{tot}$	Total Flow Rate [ml/min]

Abbreviations

BET	Brunauer, Emmett, Teller
BFB	Bubbling Fluidized Bed
BJT	Barrett, Joyner, Halenda
CaL	Calcium Looping
CCS	Carbon Capture and Storage
CFB	Circulating Fluidized Bed
CSIC	Spanish Council for Scientific Research
DDGS	Dried Distillers Grains with Solubles
DFB	Dual Fluidized Bed
EDX	Energy Dispersive X-Ray Spectroscopy
EDXRF	Energy Dispersive X-Ray Fluorescence Spectroscopy
FFB	Fast Fluidized Bed
GHSV	Gas hourly space velocity
GICO	Gasification Integrated with CO_2 capture and Storage (EU-Project)
HGC	Hot Gas Cleaning/Conditioning
HGF	Hot Gas Filter

HTC	Hydrothermal carbonization
ICP-OES	Inductively Coupled Plasma with Optical Emission Spectroscopy
ICP-MS	Inductively Coupled Plasma with Mass Spectrometry
INCAR	Carbon Science and Technology Institute, Spain
LMGC	Low and Medium Temperature Gas Cleaning/Conditioning
m/z	Mass-to-Charge Ratio
MBMS	Molecular Beam Mass Spectrometry
MP	Melting Point
MS	Mass Spectrometry
O_2/C	Oxygen-to-Carbon Ratio
OFMSW	Organic Fraction of Municipal Solid Waste
ppb_v	parts per billion (volume based)
ppm_v	parts per million (volume based)
ppt_v	parts per trillion (volume based)
SEG	Sorption Enhanced Gasification
SEM	Scanning Electron Microscope
SOFC	Solid Oxide Fuel Cell
TG	Thermogravimetry
TGA	Thermogravimetric Analyzer
TWh	Terawatt hours
WGS	Water Gas Shift
XRD	X-Ray Diffraction
ZEA	Central Institute of Engineering, Electronics and Analytics

1 Introduction

Paul Fennell and Ben Anthony introduce their book “Calcium and Chemical Looping Technology for Power Generation and Carbon Dioxide (CO_2) Capture” [1] with a very vivid picture of the CO_2 amount released by humans:

> *"Imagine the Goodyear Blimp in the sky. Now imagine it joined by (roughly) 99 more Goodyear Blimps, and all full of CO_2. Now imagine one of these sets of 100 Goodyear Blimps passes your head once every second. This is the rate at which mankind releases CO_2 into the atmosphere."*

Although the climate-damaging effect of CO_2 gas is widely known in the general population of the industrial countries, the CO_2 concentration in the air has continued to rise over the years. The amount of CO_2 gas has declined during the Corona pandemic of 2019-2022, however, its concentration has continued to increase. This is mainly due to the high residence time of CO_2 in the atmosphere. [2]

The IPCC report published in March 2023 concludes that the world must rapidly shift away from burning fossil fuels, the number one cause of the climate crisis. Under pathways that limit warming to 1.5 degrees Celsius (allowing no or limited overshoot), only 510 $GtCO_2$ can be emitted before carbon dioxide emissions reach net zero in the early 2050s. However, future carbon dioxide emissions only from existing and planned fossil fuel infrastructure could exceed this limit by 340 $GtCO_2$ and reach 850 $GtCO_2$. [3]

The capture and storage of carbon dioxide (CCS) from stationary sources such as power plants or large industrial processes has been proposed as a potential strategy to mitigate CO_2 releases. In CCS, the CO_2 is generated from combustion, transported to a storage area, and injected deep underground (> 1 km) into a stable geological formation. [1]

Greenhouse gases and air pollutants are released during the conversion of energy sources into electricity and heat. Around 84 % of German greenhouse gas emissions were attributed to them in 2021. Since 1990, the trend has been slightly down warded. Energy industry emissions account for the majority of energy-related greenhouse gases. [4]

Growth in global energy consumption halved in 2022 (from +4.9 % in 2021 to 2.1 % in 2022), and remains higher than the average rate for 2010-2019 (+1.4 %). Energy consumption growth slowed down in the two largest consuming countries in 2022: China, the world's biggest energy consumer (25 % in 2022), increased its energy consumption by 3 % (compared to +5.2 % in 2021), while the USA increased its consumption by 1.8 % (+4.9 % in 2021). The strong economic growth in India (+7.3 %), Indonesia (+21 %), Saudi Arabia (+8.4 %), and to a lesser extent in Canada (+3.8 %), and Latin America (+2.7 %, including +2.4 % in Brazil and +4.5 % in Argentina), led to an increased energy consumption. However, primary energy consumption in Europe declined (-4 %, including -4.4 % in the EU and around -3 % in the UK and Turkey), as fear of a recession following Russia's invasion of Ukraine, rising energy prices and milder temperatures caused industrial and residential consumers to reduce their energy usage. [5]

According to the German government's coalition agreement of 2021, the use of energy is expected to reach 680-750 terawatt hours (TWh) by 2030. Of this, 80 % is to come from renewable energies. Germany exceeded its 2020 renewable energy target of 35 % by supplying 46 % of its electricity from renewable sources. In 2000, the figure was just six percent. Biomass energy is an important supplement to wind and solar power. Because bioenergy is easily stored, it can be used whenever it is needed, especially in the absence of wind and sunlight. Renewable energies contributed 16 % to primary energy consumption in 2021. Biomass energy continues to be the biggest contributor to renewable energy, with a share of 52 %, ahead of wind power (just under 28 %), solar energy (photovoltaics and solar thermal, 12 %), hydropower (4%), and geothermal energy (4%). [6]

One technology that has emerged in the last two decades is biomass gasification. By comparison with biomass combustion, biomass gasification provides an alternative option for biomass use as a source of electricity and heat, or as a source of synthesis gas.

1.1 Background

One project which seeks to develop an advanced approach to convert energy from biomass into biofuel and on-demand power production by integrating biomass gasification technology is the European GICO-Project [7]. Figure 1.1 gives an overview of the different units in the GICO-Process. In the GICO-Process, two hot gas streams have to be cleaned from contaminants to protect downstream equipment (e.g. membranes, SOFC, plasma reactor). The use of CaO as a primary sorption material in the so-called sorption enhanced gasification (SEG) reactor reduces the CO_2 amount by forming $CaCO_3$, which is then fed, together with the produced char, into the calcination unit. CaO already reduces the H_2S and HCl concentration in the gasifier by forming CaS, respectively $CaCl_2$.

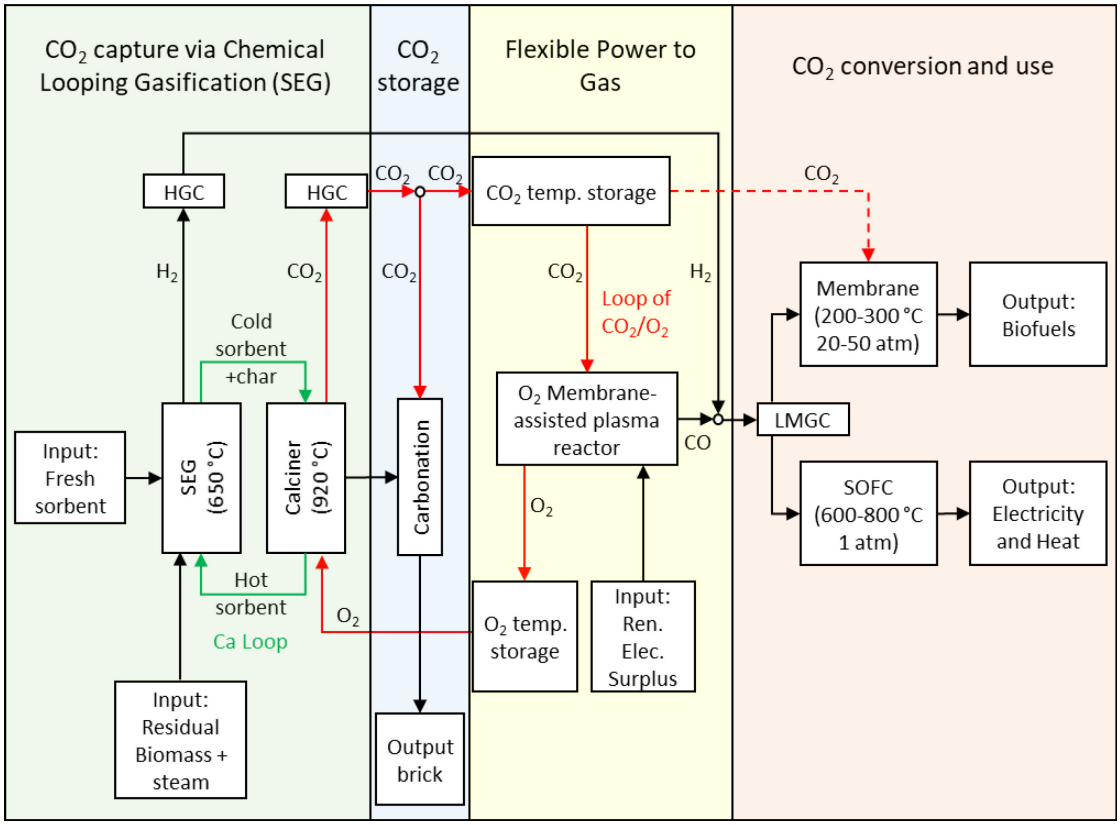

Figure 1.1: Overview of the GICO-Process, adapted from [7].

However, as these reactions are not sufficient, secondary hot gas cleaning is necessary. Via the gaseous slip, char, reacted bed material (mainly $CaCO_3$), and trace substances are transferred to the calcination unit, which also makes hot gas cleaning necessary after the calciner operating at 920 °C. Fresh bed material is continuously fed in, while the used bed material is withdrawn from the process after a few cycles. Therefore, the GICO-Process belongs to the category of carbon negative processes.

1.2 Aim of the thesis

Biomass gasification, as used in the GICO-Process, produces a complex mixture of solid, liquid, and gaseous phases. Vapor species that contain Na, K, S, and Cl are of particular interest, because they are highly volatile under the given conditions and can form sticky and corrosive layers when they reach cooler parts of the plant. The aim of this work is to show the scope for action for hot gas conditioning (HGC) for the GICO gasifier and GICO calciner. Modeling calculations and laboratory experiments were used to identify the opportunities and risks of chemical HGC concepts utilizing different sorbents.

In order to gain a better understanding of the type and amount of inorganic impurities during SEG and calcination, but also to find suitable sorbents for their removal, a FactSage model was developed. The aim was to preselect potential metals/metal oxides as well as natural occurring alkali, and alkaline earth compounds for HGC and to determine their limits of adsorptive alkali and sulfur removal for syngases produced during the GICO-Process. The preselected sorbents were then used in laboratory experiments. The calculations cover the investigation of the bed material composition, ash melting behavior, and gas concentrations. In addition, they include the gas condensation behavior before and after HGC for both gas streams, i.e. gasifier and calciner.

As CO_2 capture by CaO is driven by the difference between the partial pressure of CO_2 in the gasifier and the equilibrium partial pressures of CO_2, rather low gasification temperatures are required. Therefore, SEG is usually operated at gasification temperatures between 600-800 °C [8]. As these temperatures are below the conventional operating temperatures of most fluidized gasifiers, the release behavior of inorganic trace substance has hardly been investigated, making further investigations necessary. Consequently, there is a need for secondary sorbents for the medium temperature range, as sorbents for the low (< 600 °C) [9,10] and high temperature ranges (800-900 °C) [11,12] have already been well investigated.

Accordingly, the experimental focus of this work was on the release of inorganic trace substances under gasification-like conditions and on the investigation of secondary sorbents for the removal of detrimental inorganic trace species after gasification at 650 °C and atmospheric pressure. Two different mass spectrometers were used for these experiments.

Interactions between the most suitable sorption materials and filter candles, as determined in the calculations and sorption experiments, are investigated by means of exposure experiments. The aim was to investigate the possibility of integrating the sorption materials into the filter candles in order to allow a more compact design of the HGC unit.

2 Fundamentals of Ca-looping gasification and hot gas cleaning

In this chapter, the fundamentals of Ca-looping (CaL) gasification are presented. Moreover, the term biomass is defined in more detail, before physicochemical requirements for effective gasification are discussed. The interactions between trace substances contained in raw syngases/flue gases and downstream equipment, e.g. reactor components and catalysts are discussed. Furthermore, the influence of water-leaching and hydrothermal carbonization (HTC) of biogenic feedstock on the release behavior during gasification is explained. Finally, the fundamentals of (adsorptive) hot gas cleaning (HGC) in biomass gasification and calcination are presented.

2.1 Ca-looping technology for power generation and CO_2 capture

The first part of this chapter reviews the fundamental principles and carbon dioxide carriers (primary sorbents) which are relevant in the calcium looping technology. In the second part, the working principle of a dual fluidized bed (DFB) system will be discussed. A suggestion for improvement presented in the literature is briefly introduced. Finally, recommendations for the GICO DFB gasifier are presented.

2.1.1 Introduction to Ca-looping technology

Ca-looping (CaL) gasification is a postcombustion technology which was originally proposed in 1999 [1,13]. The main idea of CaL gasification is to use the reversibility of the reaction between CaO and CO_2. CO_2 is captured in one reactor (gasifier) and is transferred to a second reactor (calciner) in which the reversible reaction is promoted. This produces a fairly pure CO_2 stream.

The temperature of the gasifier is often given as close to 650 °C, that of the calciner as about 900 °C. The reaction between CaO and CO_2 is exothermic (reaction 2.1), the regeneration reaction endothermic.

$$CaO_{(s)} + CO_{2(g)} \leftrightarrow CaCO_{3(s)} \qquad \Delta H^{\circ}_{298} = -179\ kJ/mol \qquad (2.1)$$

Reducing CO_2 with CaO influences the water gas shift (WGS) equilibrium (reaction 2.2) in the sense of higher CO conversion and H_2 output according to Le Chatelier's principle.

This has been demonstrated in some thermodynamic modeling studies [14,15].

$$CO_{(g)} + H_2O_{(g)} \leftrightarrow CO_{2(g)} + H_{2(g)} \qquad \Delta H^{\circ}_{298} = -41 \ kJ/mol \qquad (2.2)$$

The basic assumption of these thermodynamic equilibrium calculations is that the conversion of CO to CO_2 in the WGS reaction, or the reaction of CaO and CO_2, is sufficiently fast to reach thermodynamic equilibrium. Experimental data on sorption enhanced water gas shift (SEWGS) show that this assumption is adequately fulfilled for CaO sorbents at temperatures above 500 °C. Reaction parameters included are temperature, pressure, fed gas composition, residence time, and CaO sorbent precursor. [16]

A major problem of Ca-looping is the degradation of the sorbent with the number of cycles. Limestone loses about 15-20 % of its CO_2 sorption capacity with each cycle that the material undergoes calcination and carbonation. However, there is a residual capacity of 8-10 % compared to fresh sorption material after many cycles. [1]

Early studies of the cyclic CO_2 uptake of CaO were carried out as early as 1973 using thermo-gravimetric analyzer (TGA) [17]. Ten years later, the incomplete conversion of CaO to $CaCO_3$ was attributed to the closure of narrow pores owing to the large difference in the molar volume of the product $CaCO_3$ and the reactant CaO [18]. It has been shown several times that the carbonation reaction is initially fast, but turns into a significantly slower reaction which occurs when the CO_2 diffuses through the product layer of the formed $CaCO_3$ [18–20].

An intensive effort has been currently put into the production of synthetic sorption materials based on CaO, which exhibit a high and cyclic stable CO_2 uptake. Different synthesis techniques such as hydrolysis, sol-gel or co-precipitation [21] are applied. These will ensure a sorbent that has a nanosized structure to minimize the CO_2 uptake in the slow, diffusion-controlled reactions stage of the carbonation reaction. Furthermore, the sorbent should have a high Tammann temperature matrix to guarantee a stable morphology after repeated cycles.

The basic idea of using unsupported CaO is to keep the manufacturing costs low. However, differences of the CaO skeleton and the residual CO_2 uptake with respect to the used calcium precursor, from which CaO is derived (e.g. $Ca(OH)_2$, CaO, $CaAc_2 \cdot H_2O$, $CaCO_3$, and $Ca(NO_3)_2 \cdot 4H_2O$), have been observed. According to the outcome, CaO derived from calcium acetate has the highest CO_2 uptake after 27 carbonation/ calcination

cycles (0.49 g CO_2/ g sorbent). On the other hand, CaO derived from $Ca(NO_3)_2$ shows a reduced CO_2 uptake only after the first cycle. These statements are in good agreement with BET and BJT measurements with N_2. CaO derived from $CaAc_2$ has a surface area of 20 m^2/g and a pore volume of 0.23 cm^3/g. CaO derived from $Ca(NO_3)_2$ has the smallest BET surface area of less than 1 m^2/g. [1,22]

The CaO uptake problem can be mitigated by CaO stabilization on an inert, high Tammann temperature support. In a bulk crystal lattice, the Tammann temperature is an approximation of the absolute temperature at which atoms become sufficiently mobile to diffuse readily, making them more chemically reactive and susceptible to recrystallization, agglomeration, or sintering [23,24]. A special focus in recent years has been particularly on Al_2O_3- and MgO-stabilized CaO.

Dolomite, a naturally occurring material consisting of equal molar parts of $CaCO_3$ and $MgCO_3$, is a potential CO_2 sorbent: $MgCO_3$ in dolomite has a high Tammann temperature (1276 °C), so that MgO can stabilize the pore structure effectively. Moreover, $MgCO_3$ provides pore volume during its decomposition to MgO. Unlike limestone, the molar conversion does not decrease sharply [25] making it one of the most promising CO_2 sorbents. However, due to the high MgO content in calcined dolomite, the total uptake of CO_2 is low. [1]

Another aspect that plays a role in the selection of a suitable CaO sorbent is mechanical strength. Since fluidized bed reactors are often considered suitable for the Ca-looping process [1,26], there is a need for attrition-resistant materials. However, the attrition resistance of synthetic sorbents as well as the manufacturing costs, and scale up for these new materials in form of a detailed techno-economic analysis have hardly been studied so far and therefore needs more attention.

2.1.2 Ca-looping reactor design for fluidized bed systems

Originally developed for coal gasification in the 1950s [27], the dual fluidized bed (DFB) gasifier has been adapted for biomass gasification later [28]. Figure 2.1 illustrates the working principle of a typical DFB gasification system. The (DFB) gasifier consists of two interconnected fluidized beds: A bubbling fluidized bed (BFB) gasifier that produces raw syngas gas from e.g. biomass (1) and a circulating fluidized bed (CFB) or fast fluidized

bed (FFB) combustor (riser) that oxidizes residual char by providing heat for an endothermic gasification reaction by an oxidizing agent or a fluidizing agent (2) [27]. More detailed descriptions of fluidized bed reactors, which also include challenges and perspectives, can be found in the literature, e.g. [29–31].

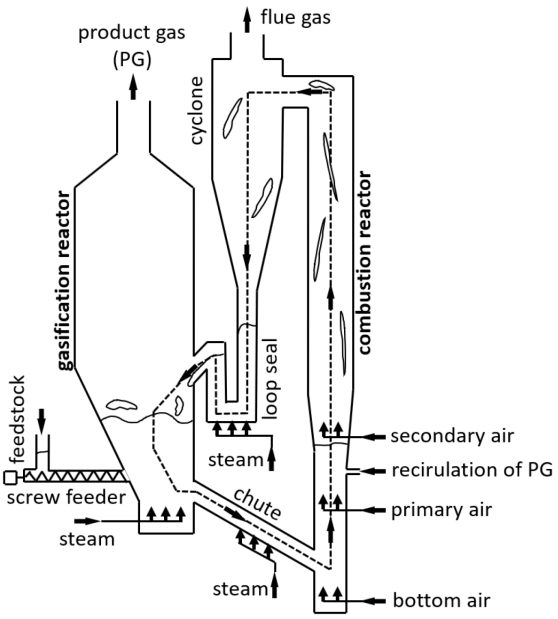

Figure 2.1: Example of a DFB reactor system, adapted from [32].

Through a screw feeder, the feedstock (e.g. biomass) is fed into the gasifier. The two fluidized beds are controlled separately, but are connected by a non-mechanical valve (e.g. loop seal) to ensure the circulation of bed material particles. The riser section uses a cyclone separator for separating heat-carrying materials from flue gases. While the flue gases are directed to the heat recovery system, the heat-carrying material is returned to the gasifier. The product gas predominantly consists of small amounts of tar, H_2, CO, CO_2, CH_4, H_2O, and other undesirable constituents. This gas is directed to the hot gas cleaning (HGC) unit to produce syngas. The riser is provided with an additional/excess fuel inlet to maintain reactor temperature. [27,33]

In order to operate at high temperatures, a large flow of heat must be supplied to the calciner. Oxyfuel combustion of fuel in the calciner is the standard Ca-looping configuration to supply the energy for calcination. However, various concepts for Ca-looping processes have been proposed recently. Many of these concepts attempt to reduce or even prevent the use of an air separation unit (ASU) which is used to produce O_2 for the calciner. In an advanced Ca-looping process, the combustor and the calciner might be separated from each other [34,35]. The heat for the calciner is then supplied by the combustor

(e.g. from power plants) and is transferred via a suspension preheater to recirculated calcined solids in a calciner (see Figure 2.2).

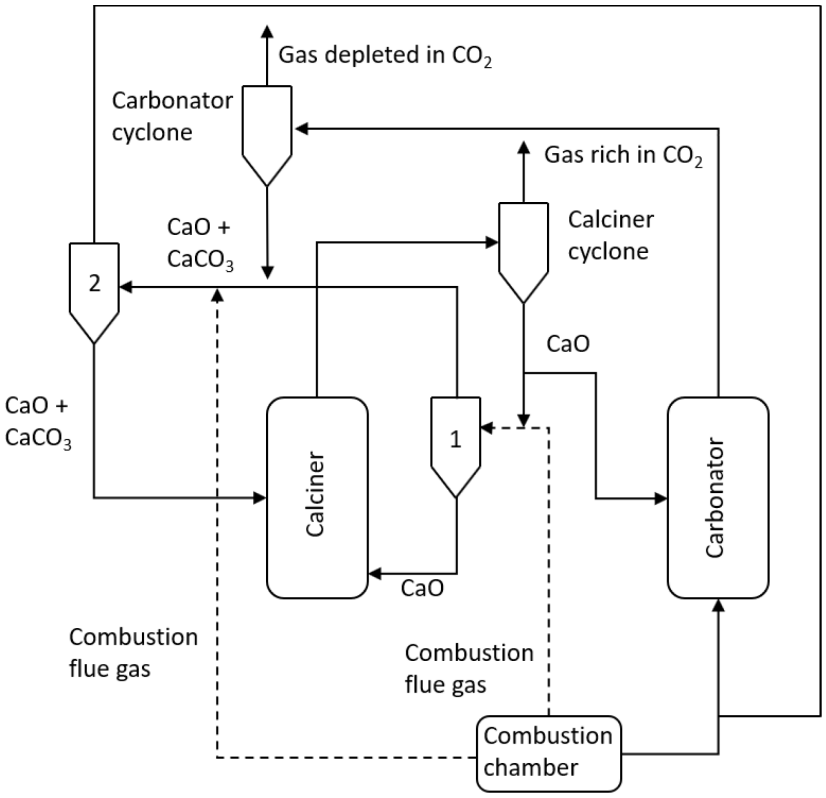

Figure 2.2: Schematic layout of the CaL process configuration based on the use of cyclonic preheaters for transferring heat from combustion flue gases to solid streams flowing to the calciner, adapted from [1,36].

In cyclone 1, the solid stream should be heated to a temperature above the calcination temperature so that it provides the necessary heat for $CaCO_3$ calcination. A second preheater (labeled as 2) should be used to heat the carbonated solids flowing to the calciner to a temperature as close to the calcining temperature as possible to reduce the heat required for solid heating. Carbonated solids cannot reach greater temperatures in this second preheater due to $CaCO_3$ calcination, since higher temperatures negatively affect CO_2 capture efficiency. This system shows great potential for efficiency improvement without requiring high-cost materials since this configuration operates without fuel consumption in the calciner. [1,36].

2.1.3 Ca-looping gasification in the European GICO-Project

The GICO-Project considered a variety of alternatives for the reactor type [37], primary sorption material [38], and biomasses [39] for a new DFB test plant. Since a part of the

investigated biomass used in the GICO-Project was also used in this work as feedstock for release experiments, it will be discussed in a separate section (Chapter 3.1).

Two different types of reactors are investigated to verify the technical feasibility of the SEG process including a rotary drum reactor (RDR) and a bubbling fluidized bed reactor (BFB). Both were used to exploit advantages and manage their disadvantage in order to optimize the product gas yield and the gas composition. At this stage, however, no final decision has been made on the type of reactor to be used.

To prevent the handling of two solids with different chemical and physical properties (e.g. attrition), GICO investigated the integration of catalyst materials within the structure of a sorbent.

Core-in-shell structured particles containing reactive CaO as the core material and an Al_2O_3-supported Ni catalyst have been investigated as preliminary sorbent/catalyst materials. Moreover, a hybrid CaO-$Ca_{12}Al_{14}O_{33}$-NiO material and $CaZrO_3$ with different CaO loads were synthesized and tested. A self-combustion method was used to synthesize CaO–$CaZrO_3$ sorbents with different CaO contents (40, 60, and 80 wt-%).

FactSage-Calculations demonstrated good CO_2 sorption properties for $CaZrO_3$ and CaO. Figure 2.3 shows the resulting gas composition caused by the interaction of $CaZrO_3$ with CO_2 in the gasifier atmosphere. $CaZrO_3$ only decompose below the gasification temperature (approx. 580 °C) and forms carbonates ($CaCO_3$) and sulfides (CaS) as a result.

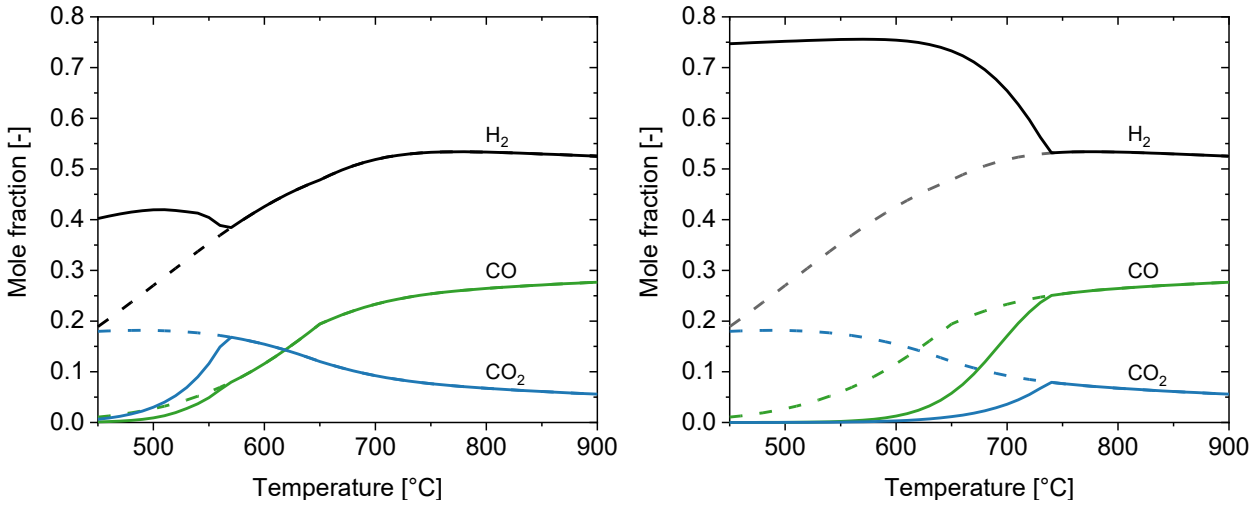

Figure 2.3: Interaction between $CaZrO_3$ and the synthesis gas (l.) and interaction between CaO and the synthesis gas (r.). The dotted lines show the concentrations without sorption material.

The reduction of CO_2 causes a shift to higher H_2 concentrations. At the gasification temperature (650 °C), on the other hand, the $CaZrO_3$ is stable and does not interact with the gas atmosphere. Therefore, from a thermodynamic point of view, it can be used as a carrier for the CaO-sorbent.

The best stability was attributed to the correct balance between CaO, the active component, and the $CaZrO_3$ nanoparticles. However, due to the lower performance of CaO/ $CaZrO_3$ compared to CaO/$Ca_{12}Al_{14}O_{33}$, the latter system composed of 40% CaO-60% $Ca_{12}Al_{14}O_{33}$ and 10% Ni/90% $Ca_{12}Al_{14}O_{33}$ is recommended.

2.2 Physicochemical requirements of biomass for enhanced gasification

As described in the previous chapter, biomass is increasingly finding its way into combustion and gasification processes. Therefore, potential problems of this fuel will be discussed in more detail in this chapter.

Moreover, this subchapter is intended to provide an initial assessment of the biomass influencing parameters for efficient biomass gasification. It discusses the advantages and disadvantages of different biomasses and explains the potential problems of trace substances during gasification and the influence of the pretreatment methods leaching and hydrothermal carbonization (HTC).

2.2.1 Biomass specifications for efficient gasification

The term “biomass” is used in a variety of contexts**.** It can refer to living organisms as well as matter from dead organisms in bioenergy. Depending on the context, it summarizes organic matter, e.g. only from plants, from plants and algae or from plants and animals. In addition to moisture, size, density, and shape, the calorific value plays an important role in virtually every energy conversion process. With regard to chemical processes such as gasification, it can be seen that many influencing variables affect each other: Moisture, for example, has a direct influence on the fuel “quality”, i.e. the amount of energy stored in a given mass of fuel, as well as the quantity. Fuels with a high moisture amount may have to be partially dried by excess energy of the process. The density of the fuel affects its storability. In addition, it should be similar to the density of the bed material in the fluidized bed gasifier to ensure good mixing.

The suitability of various biomasses for gasification is determined by their range of sizes and shapes. In order to ensure that the gasifier functions efficiently and guarantees a homogeneous thermochemical transformation and energy generation, the biomass must be processed to a uniform size and shape, thus, shredding may be necessary. However, a chips size of less than 4 cm is currently the best compromise [40,41].

Another crucial consideration is the chemical composition (C, O, H, N, S, Cl) of the biomass. In lignocellulosic biomass, the dry and ash-free contents usually consist of around 40-50 wt-% C, 30-45 wt-% O, 5-6 wt-% H, 0.1-1 wt-% N, and 0.01-0.2 wt-% S and Cl. This composition is generally more stable than that of other solid fuels such as municipal solid waste (MSW) or coal. [42,43]

Moreover, the majority of biomass constitutes volatile matter, comprising over 80 wt-%, with the remainder being charcoal. In contrast, coal typically contains only 20 wt-% volatile compounds, while the remaining 80 wt-% consists of unreactive coke, which poses greater difficulties in gasification compared to charcoal. [43]

Despite having lower sulfur and chlorine contents than coal and MSW, ash and tar contents remain major barriers to the economic and practical implementation of biomass gasification technologies. Feedstocks with high ash content require special attention due to inorganic impurities that can lead to sintering, agglomeration, deposition, erosion, and corrosion issues. Furthermore, higher ash content results in more problematic gas cleaning processes as inorganic impurities are elutriated by the production gas. Additionally, tar condenses at lower temperatures, causing blockages and damage to downstream equipment. [43]

The impurities associated with herbaceous feedstocks are primarily ash-forming elements. As a result, they are difficult to use in thermal conversion processes. Moreover, biomass from herbaceous plants releases a greater amount of inorganic trace elements and a higher moisture content than woody biomass. Biomass from wood contains fewer problematic impurities, which cause difficulties, such as corrosion at high temperatures, the formation of ash deposits, and air emissions (SO_x and NO_x). [44]

In conclusion, the ideal biomass for gasification must be available in significant quantities (t/year) and possess appropriate physical characteristics such as low water content and

high bulk density, along with desirable chemical features like high calorific values, volatile substances, and C/N ratio, in addition to low ash, chlorine, and sulfur contents. [43]

Gasification feedstocks in this context may initially be derived from lignocellulosic wastes like shells (hazelnut, walnut, pine, and almond shells), straws (wheat, corn, rye, barley, rice), agroindustrial residues (such as dried olives), concentrate (such as dried, leached olives), and cuttings from forestry and agriculture, including beech, oak, spruce, fir, poplar, willow, eucalyptus, grapes, and olives.

2.2.2 Significance of trace substances in biomass gasification and calcination

During the process of biomass gasification, not only inorganic trace compounds are released but also organic pollutants like tars [45–49]. The type and amount of these trace species depend on various factors such as soil composition, plant type, growth rate, and climate conditions. Even with the same plant type, the concentration of trace compounds can vary largely depending on the crop year [49–51].

The release of these compounds can have a significant impact on the gasifier and downstream components. Trace elements such as sulfur (S), chlorine (Cl), potassium (K), and sodium (Na) can lead to high temperature corrosion (e.g. carburization, chlorination, sulfidation), catalyst deactivation, and deposition by agglomeration. High-temperature corrosion, which is caused by physical, electrochemical, and chemical processes, can be dangerous for all hot material interfaces. Sulfidation, chlorination, and carburization are specific risks associated with biomass gasification and are independent of the trace material content. [52]

Sulfidation (or sulfidization) is a common problem for nickel and iron-based materials. In general, sulfidation means modifying or transforming a metal through exposure to sulfur compounds. As a result of sulfidation, nickel sulfides (NiS), iron sulfides (FeS), and chromium sulfides (Cr_2S_3) are formed. Due to the higher diffusion coefficient in the base material compared to the oxide layer, the process accelerates after penetration, leading to scale formation. [49,53,54]

During gasifier start-up, the oxidizing conditions favor sulfation of alkali chloride deposits [55]. Sulfatic deposits can lead to dissolution of the oxide layer in nickel-based alloys [56]. Reactions 2.3 and 2.4 explain the sulfation process:

$$SO_{2(g)} + 1/2\ O_{2(g)} \leftrightarrow SO_{3(g)} \quad (2.3)$$

$$2\ AlkCl_{(s)} + H_2O_{(g)} + SO_{3(g)} \leftrightarrow Alk_2SO_{4(s)} + 2\ HCl_{(g)} \quad (2.4)$$

Where Alk represents Na or K.

Type I and Type II corrosion can occur depending on the temperature and partial pressure of the components. Type I, occurring between 800-950 °C with low SO_3 partial pressures and high Na_2O activities, results in the formation of thermodynamically favored $NaNiO_2$, which is soluble in Na_2SO_4. A type II reaction occurs below 800 °C with high SO_3 partial pressures, resulting in nickel sulfate. This, combined with a Na_2SO_4 coating, results in a low-melting eutectic with a melting point of 671 °C, leading to material failure.

Carburization, which causes the material to lose its oxidation resistance, is not only related to the trace material content. Instead, it is a result of the increased carbon activity in the synthesis gas of the gasifier, which is determined by the CO_2-CO ratio. This activity leads to the formation of iron or chromium carbides in the protective layer of the material. As a consequence, the material undergoes embrittlement and develops cracks, eventually leading to "metal dusting". During this process, the material decomposes into metal and graphite dust. [49,57,58]

During chlorination of the material, iron chloride ($FeCl_2$) is formed. The corrosion rate in these processes depends on the fuel chlorine content and the material temperature.

Depending on the biomass composition and temperature profile, ash agglomeration and deposit formation are favored. Due to the filtering of synthesis gas after gasification, catalyst deactivation by particles is limited. However, fouling on the catalyst surface is still possible, since the synthesis gas contains alkali species that can condense at temperatures above 800 °C. As a result of deposit formation, the active surface of the catalyst decreases, resulting in a reduction in the reforming of the synthesis gas. In addition to deposits, chemical reactions with the catalyst material can also lead to its deactivation. This usually involves the sulfidation and chlorination of the catalyst material [59–62].

Alkali compounds that condense in vapor-phases generate deposits on heat exchanger surfaces [63], which can cause severe fouling problems. This is especially true for gasification of grassy biomasses, which have high silicate contents and high alkali contents [49]. Alkali metal cations, such as potassium, sodium, and corresponding alkali salts, such

as KCl/NaCl, sulfates, and carbonates, have been identified as problematic. Other consequences are ash softening and melt formation (slagging). Softened ash particles make filter candles separation harder, since they clog the pores or react directly with the filter candle material [49]. Furthermore, glassy coatings can form on heat exchanger surfaces, which significantly reduces heat flow.

2.2.3 Effect of water-leaching and HTC of biogenic feedstocks on release behavior of inorganic constituents under gasification conditions

To reduce the emission of impurities during gasification, either the fuel can be pretreated or the syngas can be posttreated. However, several biomass upgrading approaches, e.g. torrefaction [64–66], microwave pretreatment [67–69], and leaching [70–72] are considered as potential process steps for thermochemical conversion of biomass utilization.

Pretreating the biomass through water-leaching and drying can significantly reduce emissions for straw gasification, particularly for water-soluble alkalis [41,73–75]. Leaching by rain can reduce purification efforts for grassy biomasses. However, water-leaching has a minimal effect on woody biomasses, since alkalis are primarily organically bound [49].

Extraction experiments with empty fruit bunch (EFB) have shown that both chlorine and potassium concentrations can be significantly reduced by up to 80-90 % after four consecutive extractions with water [73,76]. Additionally, research indicates that water-leaching can increase the ash melting point by several hundred degrees Celsius [72]. However, insoluble inorganic components cannot be removed through water-leaching, as they are bound to active sites of lignin, cellulose, or hemicellulose. In order to remove these components, acidic environments like HCl are necessary [77].

Thermodynamic equilibrium calculations showed that a lower Si/(Ca+Mg) molar ratio reduce slag formation. In water-leached samples, K_2O was significantly lower, leading to a shift in inorganic constituents present in the ash, increasing the proportions of SiO_2 and CaO/MgO [75].

Cl can promote the release of potassium in the form of gaseous KCl [78]. Potassium is thus released more as a result of Cl content in fuels than potassium content. As confirmed by molecular beam mass spectrometry (MBMS), water-leaching successfully reduced the amount of alkali chlorides released from the fuel during conversion due to their significant reduction in the fuel [73]. Consequently, their condensation downstream the gasifier

shifted from temperatures above their melting points to temperatures below, thus contamination should be less significant. Using batch-type release experiments, it was found that potassium release behavior depends on the Si/K fuel molar ratio. Higher Si content results in less K being released, which is beneficial for preventing fouling. When Si/K ratios are very high (e.g. sewage sludge), potassium is embedded well in the slag, resulting in extremely low K releases. [73,79]

Hydrothermal carbonization (HTC) has also gained increasing interest as a pretreatment strategy for (wet) biodegradable waste. In this process, the substrate is treated at moderate temperatures (160-300 °C) and self-generated pressure. Hydrochar produced by HTC is abundant in carbon and has properties similar to lignite [80,81]. In addition to the chemical composition of the feedstock, the reaction parameters play a significant role in the outcome. Various reactions such as polymerization, decarboxylation, hydrolysis, and aromatization occur during HTC of lignocellulosic samples [82–85]. Enhanced aromaticity and hydrophobicity of the waste improve the dewatering abilities of the hydrochar [80]. Carbonization ensures sterility of waste and it has the potential to degrade emerging pollutants and endocrine disruptors [86]. As a result of the exothermic nature of HTC, a high calorific value is obtained, influenced by carbon densification and dehydration. Hydrochar has improved fuel qualities due to its decreased nitrogen and chlorine content [87]. The behavior of chlorine, nitrogen, and phosphorus during HTC has been well studied [88,89].

The reduction of nutrient compounds in aqueous waste and wastewater is a current priority. Various resource recovery options are considered for water waste streams generated during the HTC and water-leaching pretreatment processes. Although there are some challenges such as capital costs, evaporation offers a well-proven option for incorporating various resource recovery options. Moreover, several biominerals have been reported as promising fertilizers, including struvite, a mineral rich in nitrogen, phosphorus, and magnesium. [90]

2.3 Hot gas cleaning in biomass gasification and calcination

Although the gasification process for biomass is technically advanced and has been implemented on a large scale several times, one of the main existing challenges is the developing of a resource-saving and cost-effective hot gas conditioning (HGC) system to

produce a highly pure synthesis gas [91–93]. Impurities contained in syngas include particulates, tars, and inorganics, posing environmental risks. HGC can be used to reduce organic (e.g. tars) and inorganic contaminants (e.g. sulfur, chlorine, alkali metals) from low-cost fuels during gasification and calcination processes. H_2S, KCl, and HCl are the main contaminants produced during biomass gasification [52]. Moreover, there is a huge difference in terms of contaminant concentration ranging from a few ppm_v to over 1000 ppm_v depending on the biomass.

Currently, there are only a few methods for tar cracking. The most advanced techniques for tar cracking include autothermal reforming and partial oxidation [49]. As tar removal/conversion and particle removal are conducted separately in the present biomass gasification plants, the plants can be more compact when processes are carried out in the same reactor [94]. Catalytic filters can carry out both solid-state filtration and tar conversion in one step. In order to impregnate the filter element, a catalytic coating is applied or the catalytic component is incorporated into the filter structure, i.e. the mixture of ceramic grains and binders.

So far, catalytic activity of a MgO supported catalyst (6 wt-% Ni) was achieved for 100 h at 800 °C with a filtration rate of 90 m h^{-1} (2.5 cm s^{-1}) in the presence of 100 ppm_v H_2S, with complete conversion of naphthalene [95]. In other experiments, porous alumina filter discs were tested on their sulfur poisoning resistance using benzene and naphthalene as model compounds. Ni/MgO-activated filter discs with increased surface area achieved 99.89 % naphthalene conversion when operating at 2.5 cm/s and 100 ppm_v H_2S [96].

Moreover, there is a wider range of techniques for particle and ash separation. In principle, the separation of particles and ash can be achieved by washing (wet scrubbing) and filtration (electrostatic filtration, barrier filtration, and cyclone filtration).

The most effective and reliable gas cleaning technique to date is wet scrubbing, also known as wet gas cleaning. During scrubbing, one or more components of a gas stream are selectively absorbed into an absorbent. The term "scrubbing" is used interchangeably with "absorption". Most commonly, water is used as an absorbent liquor in wet scrubbing. However, other relatively nonvolatile liquids can be used as absorbents. This process has some disadvantages, such as waste water disposal and gas cooling, which reduces the overall efficiency of the system. [97]

Electrostatic filtration is another gas cleaning technique. An electrostatic filter has two main sections. In the ionizing section, fine wires are charged to a voltage up to 13 kV and alternated with earthed rods. The ionizing field creates a corona discharge and the air-borne particles are charged positively as they pass through the ionizing field. Secondly, there is the collector section, which is made up of parallel, vertical metal plates with a potential difference of 6-7 kV between them. Ionized dust particles are attracted to these plates. However, this process tends to form deposits and is only suitable for biomasses with a high ash melting temperature. [98]

Cyclone filtration is one of the most durable and robust methods for removing up to 98 % of particles larger than 5 µm in diameter, even at high temperatures [49]. For particles smaller than 1 µm, the barrier filter is used. Barrier filters come in various designs, including fabric filters, fixed-bed or packed-bed filters, and filter candles. Common fabric filters have limitations on operating temperatures since they are made of natural fibers, glass fibers, or polymers. Conventional fabric filters are limited to operating temperatures lower than 260 °C while ceramic fiber filter bags were operated up to 760 °C [99]. Common materials for fixed-bed or packed-bed filters are sawdust, ceramic balls, or sand. The limited use of filters for biomass gasification is due to the potential accumulation of ash and tar, especially with low temperature molten ash.

Filter candles made of metals or ceramics can be sintered in various forms. Their porosity and mechanical properties depend on the source material. By using catalytically active components, filter candles can be used for both tar cracking and particle separation. Since this is a cake filtration process, cyclic repulsing is required to regenerate the filter candles. During repulsing, the gas flow is reversed to remove particle layers from the surface of the filter candle. Ceramic filter candle have a high potential for particle removal and are widely used. [100]

In the GICO-Process different sulfur compounds are present in gases in different operating units, with SO_2 predominating in calciner gases and H_2S being a by-product of gasification. However, small quantities of each product can be found in either unit. Consequently, it is important to distinguish between HGC methods that remove SO_2 from calciner gases and those that remove H_2S from the gasifier gases. Since H_2S is one of the most problematic sulfur contaminants under gasification conditions, its removal is necessary (see Chapter 2.2.2). However, currently used techniques are producing by-products

that need to be further treated. Moreover, they are energy intense due to the thermal management (cooling and heating steps) of the feed stream.

Therefore, investigations on chemical HGC were conducted and show that metal oxides are suitable for sulfur reduction [101–103]. Several Mn-, Ca-, Cu-, Fe-, Ce-, and Zn-based sorbents with high sulfur capacity have been developed in the temperature range up to 600 °C [49]. It is possible to achieve H_2S concentrations of 1-5 ppm_v for Cu-based sorbents to 10 ppm_v for zinc ferrites in gasifier-derived gases [103,104]. Although reaction 2.5 shows that the sorption reaction is sensitive to water, many syngases used for H_2S sorption investigations were only balanced with N_2 or He [105–111].

$$MeO_{(s)} + H_2S_{(g)} \leftrightarrow \ MeS_{(s)} + H_2O_{(g)} \tag{2.5}$$

In order to fulfill the requirement of nickel catalyst for 1 ppm_v H_2S in the high temperature range of 800-900 °C, investigations were carried out with BaO. Thermodynamic calculations indicate that stabilized BaO sorbents should retain 1 ppm_v H_2S, therefore the stabilization of the sorbent by CaO was investigated. [12]

CaO-BaO shows low solubility at temperatures above 1200 °C. Therefore, in previous studies a sorbent was prepared from a mixture of BaO and CaO. The sorbent reduced the H_2S concentrations to values below 0.5 ppm_v in the temperature range of 800-900 °C. The XRD analysis confirms the stabilization effect by the appearance of a BaS phase in the sorbent, which should normally be unstable under these conditions. At temperatures below 760 °C, the remaining H_2S concentration increases strongly due to the carbonation of the sorbent. [11]

Another potential second-generation sorbent for high-temperature gas desulfurization that has been studied is cerium oxide. Moreover, reversible adsorption of H_2S on cerium oxide surfaces has been demonstrated over many cycles at temperatures as high as 800 °C. Despite the fact that CeO_2 will react with H_2S, the reaction thermodynamics do not allow H_2S target levels of about 20 ppm_v to be achieved. CeO_2 is reduced at high temperatures to a nonstoichiometric oxide, CeO_n ($n < 2$), which is superior to CeO_2 in removing H_2S. As a function of temperature, pressure, feed gas composition, and flow rate, the reduction and sulfidation reactions were studied in fixed-bed reactors. [112,113]

Ce_2O_3 forms an oxysulfide (Ce_2O_2S) with H_2S, but also Ce_2S_3 (see reactions 2.6-2.9). The H_2S vapor pressure over Ce_2S_3 is greater than the vapor pressure of H_2S over Ce_2O_2S.

$$2CeO_{2(s)} + H_{2(g)} \rightarrow \ Ce_2O_{3(s)} + \ H_2O_{(g)} \quad (2.6)$$

$$2CeO_{2(s)} + H_2S_{(g)} + H_{2(g)} \rightarrow \ Ce_2O_2S_{(s)} + 2 \ H_2O_{(g)} \quad (2.7)$$

$$Ce_2O_{3(s)} + H_2S_{(g)} \rightarrow Ce_2O_2S_{(s)} + H_2O_{(g)} \quad (2.8)$$

$$Ce_2O_{3(s)} + 3H_2S_{(g)} \rightarrow Ce_2S_{3(s)} + 3 \ H_2O_{(g)} \quad (2.9)$$

It has been shown that it is marginally more effective to produce CeO_n as a separate step before reduction rather than simultaneously combined reduction and sulfidation. Despite this, both approaches were able to reduce H_2S below the levels of 20 ppm_v. [112]

It is important that desulfurisation sorbents have a high capacity, good chemical stability, fast kinetic reactions, and are both affordable and abundant. Table 2.1 summarizes the estimated tolerance limits for those inorganic contaminants that are expected to severely affect solid oxide fuel cells (SOFC) performance.

Table 2.1: Tolerance limits of inorganic contaminants for SOFC [114,115].

Contaminant	Concentration [ppm]
H_2S	1-3
HCl	10-200
Alkali	10-200

However, posttreating the syngas can not only be achieved by gas purification but also by impurity retention. Additives, such as lime, dolomite, or kaolin to reduce the release of sulfur and alkali species can be added to the fuel. [116,117]

In conventional direct combustion processes, the most common technology to reduce sulfur at high temperature revolves around pulverizing $CaCO_3$ or dolomite, which is then fed into the combustion chamber. This means that SO_2 is removed right after combustion, before any gaseous material is produced. [103]

In general, it can be concluded that at higher temperatures (approximately 800 °C) $CaSO_4$ will be produced (reaction 2.10), while at lower temperatures, in the 450–800 °C region, the solid products are CaS and $CaSO_3$ (reaction 2.11) as well as $CaSO_4$. [103]

$$CaO_{(s)} + SO_{2(g)} + 0.5O_{2(g)} \rightarrow \ CaSO_{4(s)} \tag{2.10}$$

$$CaCO_{3(s)} + SO_{2(g)} \rightarrow \ CaSO_{3(s)} + CO_{2(g)} \tag{2.11}$$

$CaSO_4$ has a molar volume three times greater than CaO, therefore, the molar volume of $CaSO_4$ produced during sulfidation will exceed the molar volume of CaO consumed, resulting in an increase in the amount of pore blockage that gradually eliminates SO_2 access to the active surface of CaO. [103]

Alkali sorption experiments on aluminosilicates (bauxite, bentonite, kaolinite, etc.) have been undertaken in various temperature ranges over the past few decades [118,119]. However, reaction 2.12 indicates the necessity of water [120,121].

$$Al_2O_3 \cdot xSiO_{2(s)} + 2AlkCl_{(g)} + H_2O_{(g)} \ \leftrightarrow 2AlkAlO_2 \cdot xSiO_{2(s)} + 2HCl_{(g)} \tag{2.12}$$

The thermodynamic equilibrium data in Figure 2.4 shows a clear stepwise trend during sorption on kaolin. The vertical lines represent one or two of the stable K-Al-Si compounds $KAlSiO_4$ (kalsilite), $KAlSi_2O_6$ (leucite), and $KAlSi_3O_8$ (K-feldspar), whereas the horizontal plateaus represent the transition from one three-phase region to another over a two-phase transition zone.

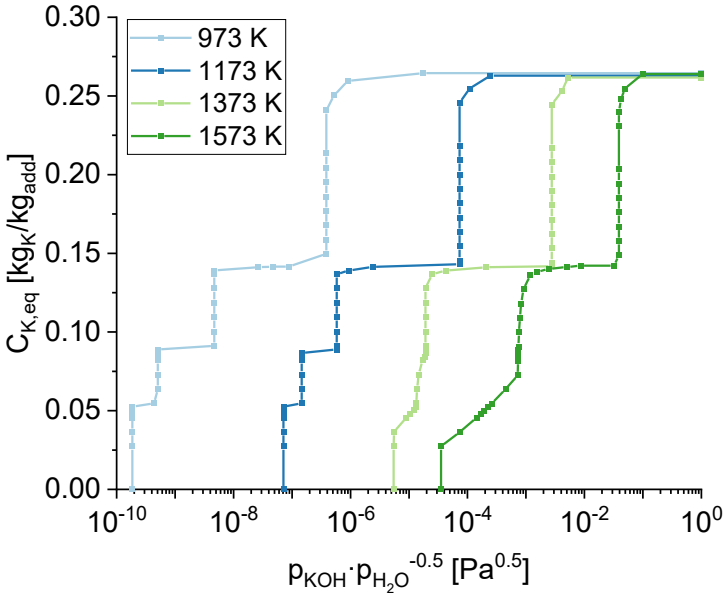

Figure 2.4: Equilibrium potassium-capture as a function of the partial pressures of KOH and H_2O, adapted from [122].

Although it is a modest air pollutant, HCl gas is troublesome because of its high solubility and corrosive nature [123,124]. That is the reason why its removal is an important issue. Studies on Ca-based sorbents indicate a high conversion rate for HCl between 400-650 °C [125–127]. Reactions 2.13 and 2.14 show the mechanisms for HCl sorption on CaO.

$$CaO_{(s)} + 2HCl_{(g)} \leftrightarrow CaCl_{2(s)} + H_2O_{(g)} \quad (2.13)$$

$$CaCO_{3(s)} + 2HCl_{(g)} \leftrightarrow CaCl_{2(s)} + H_2O_{(g)} + CO_{2(g)} \quad (2.14)$$

Thermodynamic investigations have shown that only a concentration of 600 ppm_v can be achieved during HCl sorption on Ca-based sorbents above 800 °C [128]. However, in a dry atmosphere, HCl has been reduced below 1 ppm_v [129,130] by stabilizing calcium in an aluminosilicate phase (hydrogrossular). Further studies are required to determine the HCl concentration achieved by the hydrogrossular in a humid reducing atmosphere [49].

Sufficient HCl removal with Na_2CO_3, K_2CO_3, and dried distillers grains with solubles (DDGS) ash has also been demonstrated for temperatures up to 550 °C at Forschungszentrum Jülich (see Figure 2.5) [131]. To determine kinetically effects, a gas stream consisting of 66 % He, 4 % H_2, and 30 % H_2O was varied between 2-4 l/min. The length of the sorbent fill varied from 25 mm to 100 mm.

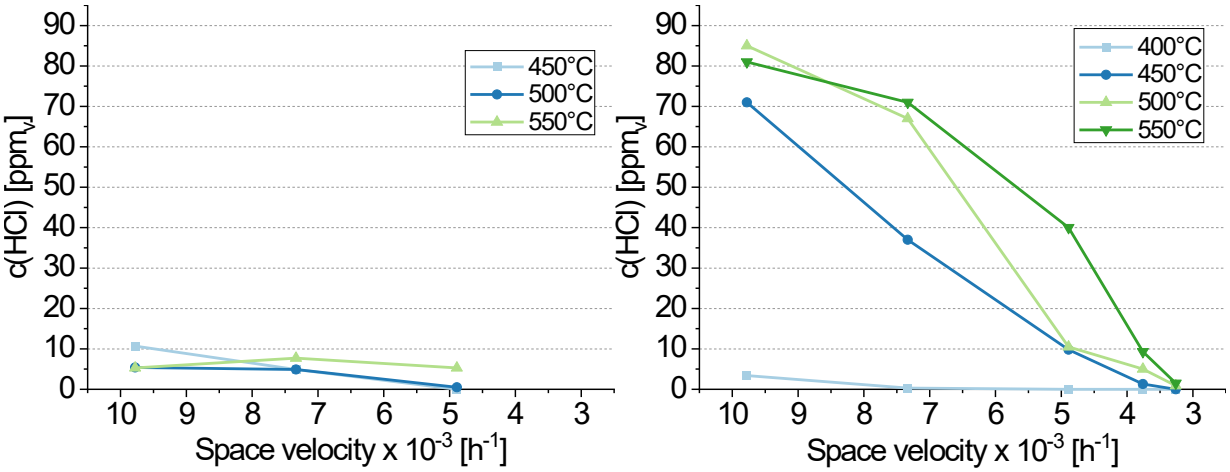

Figure 2.5: Kinetics of HCl sorption on Na_2CO_3 (l.) and K_2CO_3 (r.) at 450 °C, 500 °C, and 550 °C, adapted from [131].

The HCl sorption on Na_2CO_3 and K_2CO_3 at temperatures between 400 °C and 550 °C shows that this reaction is kinetically limited. In order to prevent the limitation through kinetics, the space velocity has to be reduced to 4900 h^{-1} for the Na_2CO_3 sorbent and to

3750 h^{-1} for the K_2CO_3 sorbent. However, HCl concentrations of 1 ppm_v are achievable below these space velocities.

3 Research methodology and experimental setups

This chapter includes the description of the pretreatment methods of the investigated biomasses, their chemical analyses, and the production procedure of different sorbents. Moreover, it contains a description of the FactSage model used to select suitable sorbents for the sorption experiments. In addition, all experimental setups used for the release experiments, the sorption experiments, and the filter candle exposure experiments are described. As described in Chapter 1.2, the focus was placed on the relatively little investigated medium temperature range in which the GICO gasifier (650 °C) operates.

3.1 Biomass samples, pretreatment, and chemical characterization

Four different types of biomass wastes provided by the Carbon Science and Technology Institute (INCAR-CSIC), Spain, within the framework of the GICO project were used for the release experiments (see Figure 3.1). Both the release behavior of the untreated biomass and the release behavior of three differently pretreated biomasses were investigated:

1. Solids from an HTC process
2. Water-leached samples
3. Samples mixed with CaO

The latter pretreatment method is used to simulate the process taking place in the gasifier. Special attention was paid to biomasses that are not really promising for gasification requirements, but have a large occurrence in Europe including Grape Bagasse, Organic Fraction of Municipal Solid Waste (OFMSW), Green Waste, and Out-of-use woods from construction debris and discarded furniture.

The hydrochars were obtained by subjecting the diverse feedstocks at 195 °C and 13.2 bar at 195 °C in an HTC pilot reactor of 1 m^3 for 3 hours. The biomass/water ratio was 1:4. To achieve greater profitability and a lower environmental impact based on the reduction of water consumption and the elimination of two wastes simultaneously, a co-hydrothermal carbonization of Out-of-use woods was approached by using whey instead of water as a reaction medium. The samples were dried to mass constancy at 105 °C and vacuum sealed for shipment.

Figure 3.1: Overview of biomasses used in the release experiments.

To increase the specific surface and thus improve the mass transfer between the fuel and the water during leaching, each sample was milled and fractionated to a diameter of 0.2 mm. All biomass samples (untreated and hydrochar) were washed twice. Each washing cycle lasted one hour. In each case, 500 ml of deionized water were added to 50 g

fuel sample in PET bottles. The bottles were then placed on a roller so that the contents were mixed. After each cycle, the sample was vacuum filtered using a water aspirator. After the washing cycle, the biomass was dried to constant mass at 105 °C.

Each sample was chemically characterized afterwards. An elemental analysis was performed for C, H, N, S, and O. For the major ash forming elements (e.g. K, Ca, Na, …) optical emission spectroscopy combined with inductively coupled plasma (ICP-OES) was used. The filtrate for both washing cycles was collected and also used for the quantification of Ca, K, Mg, Na, P, Si, and Cl using ICP-OES. The analysis was carried out by the Central Institute of Engineering, Electronics and Analytics (ZEA-3) at Forschungszentrum Jülich. The results are presented in Figure 5.1, Table 5.1, and Table 5.2 of Chapter 5.1.

3.2 Thermodynamic modeling of the GICO-Process with FactSage

Since knowledge of inorganic trace substance concentrations in syngases from (pretreated) biomasses is fundamental for the removal of trace substances, a model for describing both the release and the removal of trace substances in syngases was created. The aim is to determine the limits of sorptive alkali and sour gas removal for syngases and calciner gases produced during the GICO-Process. Due to the large variety of syngas components, adsorptive HGC in the context of biomass gasification and calcination is a complex chemical system. In FactSage, a thermodynamic calculation tool, thermodynamic equilibria in chemical systems can be calculated depending on chemical composition, temperature, and pressure by minimization of the Gibbs energy of a system. FactSage is a product of the companies Thermfact (Canada) and GTT-Technologies (Germany) [132] and is based on ChemApp and ChemSage [133]. The in-house developed oxide database GTKT [134] and the commercial database SGPS were used for the calculations. In the case of duplicate species, GTKT was given a higher priority.

As shown in Figure 3.2, the GICO model consists of several equilibrium reactors and phase separators represented by squares. The equilibrium reactors are connected to each other and to the environment via material flows represented by arrows.

The model begins with the introduction of the two input streams water and biomass into the gasifier. Water is added until all the elemental C (graphite) from the biomass has been oxidized to carbon monoxide and carbon dioxide at 650 °C under atmospheric pressure. With the help of a phase separator, the gas phase is then separated from the solid phase,

so that only the gas phase is considered in the CaO sorption calculation. In this way, the considerably faster reaction between the gas and CaO should take precedence over the solid-solid reactions between the ash components of the biomass and the sorbent. The amount of CaO used in the modeling was determined using the transition-function in FactSage. This function can be used to determine the amount of CaO above which no change in the gas phase occurs. This approach simulates sufficient residence time and amount of CaO for the complete conversion of all potential reactants in the fluidized bed reactor.

The solid phase that remains after the water reaction is the carbon (graphite)-free, mineral ash. Chapter 4.1 discusses the ash melting behavior of the different biomasses. For these calculations, the formation of the gas phase in FactSage was suppressed to ensure mass constancy of the condensed phase.

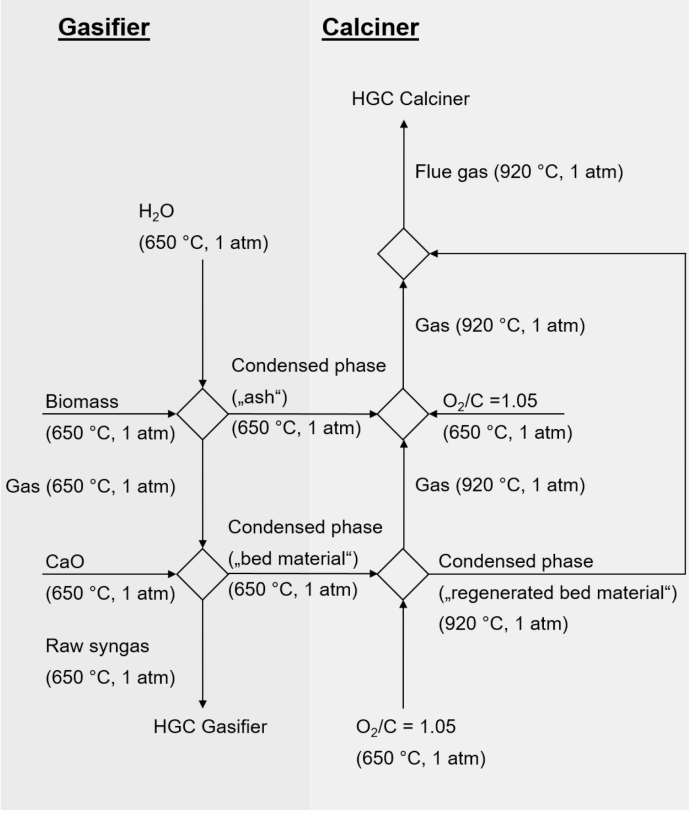

Figure 3.2: Schematic representation of the gas release and sorption calculations via FactSage.

After the gas-CaO reaction, the gas phase and the condensed phases are separated from each other again. Chapter 4.1 gives a summary of the achievable gas stream purities and of the composition of the reacted bed material consisting mainly out of $CaCO_3$ leaving the

gasifier. Further calculations for hot gas cleaning are carried out in Chapter 4.2. The solid phase, on the other hand, which represents the bed material, is adiabatically brought to 920 °C by adding O_2 and C in a ratio of 1.05. This is necessary since all C has been converted in the gasification calculation. This assumption was made since values for the mass of coke in the slip cannot be found. Statements about the gas amount after the calciner can therefore no longer be related to the mass of biomass. Together with the bed material, $1/10^5$ of the mass of the bed material in gas phase is also transferred into the calcination calculation. This is to ensure the required water content for the subsequent alkali sorption. The gas slip also considers the possibility of transferring contaminants from the gasifier into the calciner. The addition of C (graphite) represents the transfer of the carbon-rich coke into the calcination unit. Chapter 4.3 deals with the influence of the slip and the O_2/C ratio on the inorganics in the gas phase.

The gas phase from the calcination of the bed material is mixed with the ash and again brought adiabatically to 920 °C by adding O_2 and C in a ratio of 1.05 to enable vaporization of ash components. The resulting gas phase is then mixed with the calcined bed material to simulate reactions of the bed material with volatile inorganic trace species.

Figure 3.3 shows the calculation scheme for the subsequent hot gas cleaning. The concept consists of an alkali and a sour gas cleaning unit. The gas is brought into contact with various sorption materials.

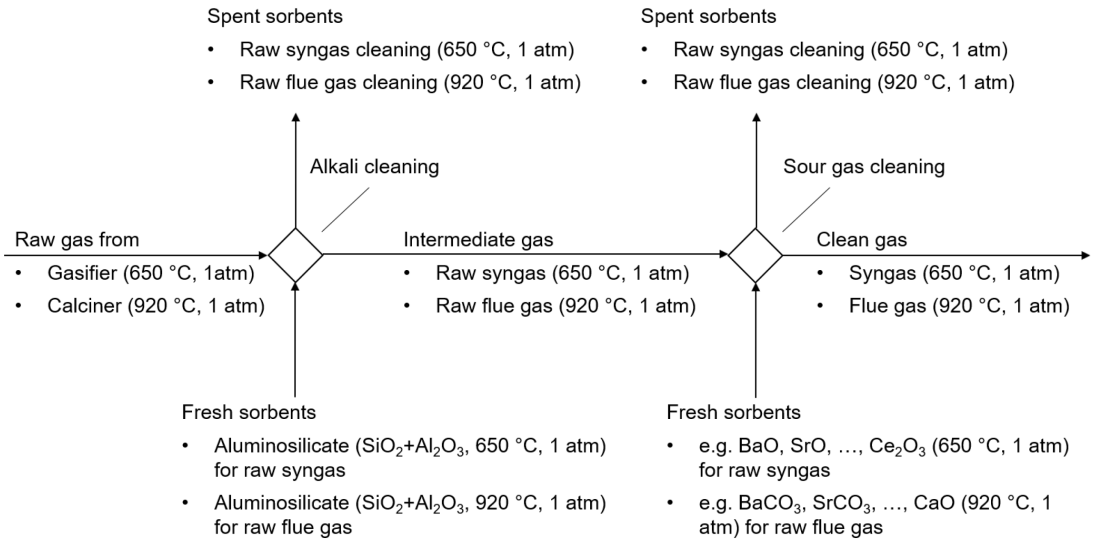

Figure 3.3: Schematic representation of the HGC calculations. Both HGC units, for the gasifier and for the calciner, consist of an alkali cleaning unit and a sour gas cleaning unit.

The sorbents were added in a significant excess, so that the concentrations are the minimum achievable with the respective sorbents and temperature. Moreover, no further gas-solid reactions can occur. For alkali sorption, the two aluminosilicate components SiO_2 and Al_2O_3 were used in excess. Since HCl is released during alkali cleaning with aluminosilicates (reaction 2.12), the sour gas cleaning unit must be located afterwards.

Condensation calculations are carried out for the gas flows leaving the gasifier and the calciner. The condensation behavior is compared with the condensation behavior after the various hot gas cleaning steps. The condensed mass is related to the input biomass. Graphite (C) is not included in those calculations because its precipitation would lead to a significant reduction in the gas volume, which would increase the concentration of the other species.

In Deliverable 2.1 “Selection of feedstocks and their characterization” of the GICO-Project [39], the results of elemental analysis for all the selected feedstocks are reported. Since this document does not cover the analysis of the hydrochars, the biomass composition was analyzed, too. The composition of the biomasses used in the model can be found in Table 3.1. These values were obtained from the normalization of the ICP-OES analysis in Table 5.1.

Table 3.1: Biomass compositions in the simulation [wt-%].

Biomass	C	H	N	S	Cl	O	Al	Ca	Fe	K	Mg	Na	P	Si
Green Waste	39.1	5.33	1.54	0.20	0.23	36.22	1.07	2.29	0.94	1.14	0.28	0.10	0.00	11.58
Green Waste Hydrochar	47.6	5.28	0.99	0.11	0.11	35.08	0.63	1.93	0.65	0.51	0.15	0.06	0.00	6.89
OFMSW	42.0	5.76	2.82	0.24	0.82	36.85	0.36	4.67	0.36	1.01	0.55	0.77	0.73	3.05
OFMSW Hydrochar	48.6	6.09	2.51	0.18	0.49	31.76	0.27	5.30	0.23	0.76	0.26	0.48	1.05	1.98
Out-of-use woods	46.7	6.19	1.96	0.09	0.06	44.41	0.04	0.20	0.05	0.07	0.03	0.06	0.00	0.13
Out-of-use woods Hydrochar (whey)	48.0	5.97	1.42	0.10	0.32	42.09	0.04	0.56	0.19	0.38	0.07	0.28	0.00	0.55
Out-of-use woods Hydrochar (water)	51.5	5.77	2.40	0.10	0.11	37.86	0.08	0.51	0.16	0.08	0.10	0.29	0.00	1.03
Grape Bagasse	48.8	5.94	2.38	0.18	0.003	37.66	0.03	0.34	0.17	3.94	0.12	0.01	0.31	0.09
Grape Bagasse Hydrochar	57.6	6.09	2.32	0.18	0.01	30.62	0.07	0.38	0.12	2.41	0.07	0.02	0.00	0.12

3.3 Release experiments using MBMS

Inorganic gaseous species released during gasification were measured using molecular beam mass spectrometry (MBMS). The experimental setup allowed the analysis of hot gases from various biomass derived feedstocks under gasification-like atmospheres. This technique employed common mass spectrometry to analyze the mass-to-charge ratios (m/z) in an electromagnetic field. An explanation of the functioning of the MBMS used is omitted here, as this has already been provided in numerous places [135,136].

Experiments were conducted under gasification-like conditions at 650 °C, using a four-zone furnace with an alumina-tube connected to the MBMS nozzle as the gas inlet. The sample was gasified in the first two zones at 650 °C while the third zone was set to 1000 °C to prevent condensation and crack all formed hydrocarbons, enabling the study of inorganic species only. A visualization of the setup is given with Figure 3.4.

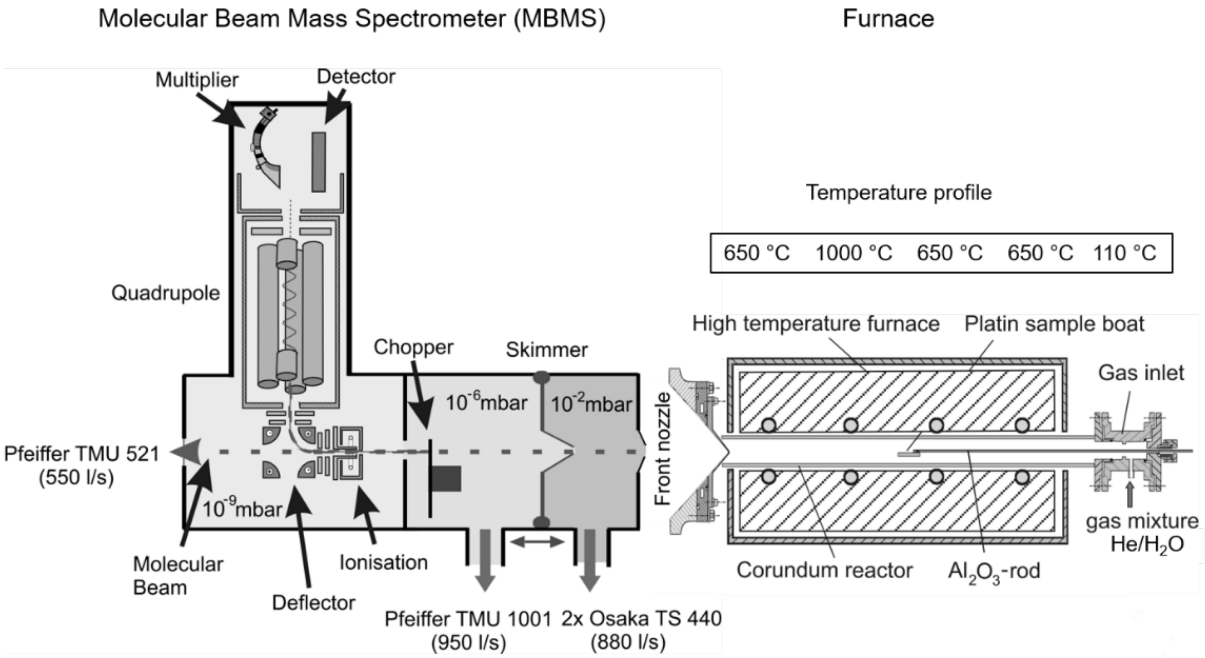

Figure 3.4: Experimental setup for release experiments.

A continuous spectrum of masses 1 to 200 was recorded during an empty tube measurement. Gas components with an expected high concentration (and correspondingly high intensity) were excluded from the measurement in order to increase the sensitivities of the trace substances. Figure 3.5 shows the spectrum after removing the masses 18 (H_2O), 37 ($(H_2O)_2$-H), and 44 (CO_2).

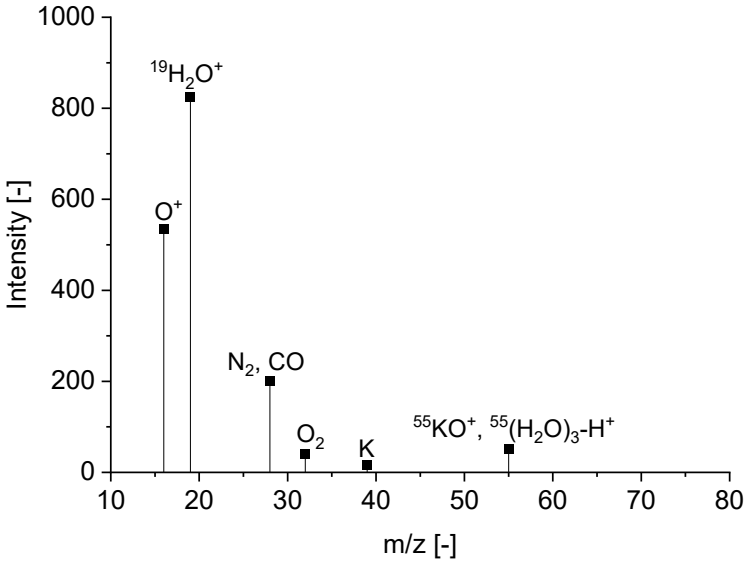

Figure 3.5: Intensities during empty tube measurement.

Intensity-time profiles of $^{19}H_2O^+/^{19}OH^+$, $^{34}H_2S^+$, $^{35}Cl^+$, $^{36}HCl^+$, $^{38}HCl^+$, $^{39}K^+$, $^{55}KO^+/^{55}(H_2O)_3\text{-}H^+$, $^{58}NaCl^+$, $^{60}COS^+$, $^{64}SO_2^+$, $^{74}KCl^+$, and $^{113}K_2Cl^+$ were recorded and normalized to the $^{19}H_2O^+/^{19}OH^+$ base level signal for quantification. Each sample was measured five times, and the averages were used for error calculations and semi-quantitative analysis. A gas consisting of 20 % H_2O and 80 % He was used throughout the measurement campaign. The total gas flow was set to 4 l/min for each experiment. 50 mg of fuel were gasified in Al_2O_3-sample boats in a single run and kept in the furnace for 5 minutes.

For the mixture release experiments, CaO was mixed 1:1 (by mass) with each biomass sample. In contrast to the pure biomass release experiments, 100 mg of sample material was used in order to keep the amount of biomass constant. The molar ratio of C in the biomass to CaO is between 0.38 (Grape Bagasse Hydrochar) and 0.67 (Green Waste). Accordingly, CaO is available sub-stoichiometrically for the reaction of CO_2 to $CaCO_3$.

The ash resulting from the MBMS experiments was collected and analyzed using the XRD method (X-Ray Diffraction). The MBMS adjustments for the release experiments can be found in Table A.1.

3.4 Experimental setups for the sorption of syngas inorganics

Except for the gas analysis, the experimental setups for the KCl sorption and the sour gas sorption were almost identical: A synthetically mixed syngas loaded with impurities was led through a sorbent bed in a tube furnace. This type of experimental setup has been used successfully in several previous studies [137,138].

All sorption experiments were conducted as fixed bed investigations at atmospheric pressure. As soon as the sorption material was saturated and the H_2S and HCl concentration increased, the sorption experiments were stopped. The KCl sorption tests, on the other hand, were stopped after 20 h since no increase in the corresponding signal could be detected.

3.4.1 Experimental setup for KCl sorption

The KCl sorption experimental setup consisted of a tube furnace with five independent heating zones. A high-density Al_2O_3-tube was used as the reaction tube. This material does not bind any alkalis at temperatures below 1000 °C. To determine the KCl concentration in the syngases achieved by sorption, the test setup shown in Figure 3.6 was used.

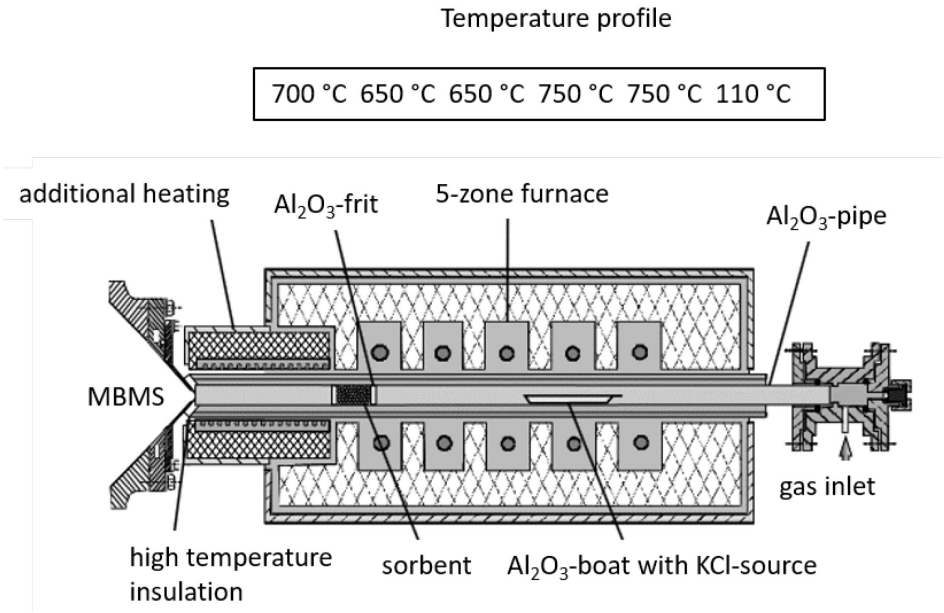

Figure 3.6: Experimental setup for sorption tests, adapted from [49].

Since previous thermodynamic calculations showed that the substitution of a simulated flue gas by helium has no influence on the KCl sorption [49,139], the syngas was synthetically mixed from 10 % H_2 and 83 % He. The gas stream was further loaded with 7 % H_2O by flowing through a vaporizer. The gas mix (4 l/min) flowed through a flange into the cold end of the Al_2O_3 tube.

The Al_2O_3 tube had an inner diameter of 25 mm and a length of 870 mm. It was installed horizontally in a 5-zone furnace with an additional heating at the outlet. The additional heating was set to 1000 °C and used to prevent the KCl from condensing at the inlet of

the MBMS. The syngas was loaded with approximately 25 ppm_v KCl shortly after flowing into the Al_2O_3 pipe by overflowing a 750 °C hot Al_2O_3 boat filled with KCl (alkaline source). The contact surface of the KCl with the syngas stream is approximately 900 mm^2.

The KCl loaded syngas then flowed through the bed of an aluminosilicate sorbent. To completely cover the pipe cross-section with sorption material, the sorbent was pressed between two Al_2O_3-frits. The frits had a material thickness of 10 mm and consisted of a coarse-pored high-temperature foam. To reduce the flow resistance the sorbent was fractionated to a grain size between 1.6 and 4 mm. Approximately 30 g of sorbent were used per bed corresponding to a bed length of 50 mm.

The experimental setup such as syngas composition, syngas volume flow, general settings of the MBMS (ionization voltage, multiplier voltage, optics) was kept constant.

3.4.2 KCl sorbents and their preparation

The chemical composition and the specific surface areas of the sorbents were determined by ZEA 3 of Forschungszentrum Jülich and are given in Table 3.2 and Table 3.3. Before the BET measurement, the samples were outgassed by heating in a vacuum at 300 °C for 1 h. The materials used for alkali sorption are aluminosilicates differing in Al_2O_3 and SiO_2 content. Except for the bauxite, the SiO_2/Al_2O_3 ratio is bigger than 1.

All sorbents listed in Table 3.2, except Boke Bauxite and Cat litter, were prepared from powder. The powder was mixed with water and formed into pellets. The pellets were then exposed in Al_2O_3 crucibles for 5 h at 650 °C in an air atmosphere. The sorbents were fractionated afterwards to a particle size of 1.6 to 4 mm. Cat litter and Boke Bauxite samples were still available from previous experiments and were only fractionated accordingly.

Table 3.2: Chemical composition of the KCl sorbents [wt-%].

Sorbent	Al_2O_3	SiO_2	Fe_2O_3	K_2O	Na_2O	CaO	MgO	BaO	Total
Boke-Bauxite	75	1.3	17.4	0	-	0	-	0	93.8
Clinoptilolite	12.8	76.2	0.3	3.5	1	2.3	0.6	0.1	96.8
Kaolin	47.2	58.6	0.8	2.2	0.1	0.1	0.3	0	109.4
Bentonite	17.9	64	1.1	0.5	3.1	0.4	2.8	0.1	89.9
Cat litter	0.2	51.1	0	0	-	20.3	2.2	-	73.9
Montmorillonite	19.5	61	0.9	1.4	0.3	0.6	3.7	0	87.4
Foam	94.1	5.5	-	0.5	0.5	-	0.1	-	100.7

Table 3.3: Specific surface areas [m^2/g] of the KCl sorbents.

Sorbent	Specific Surface
Boke-Bauxite	240.387
Clinoptilolite	26.366
Kaolin	15.761
Bentonite	15.538
Cat litter	95.083
Montmorillonite	60.417
Foam	1.358

Figure 3.7 shows the six different aluminosilicates used in the sorption experiments. The reddish color of the Bauxite is due to iron oxides which make up a big part of the ore (see Table 3.2).

Figure 3.7: Visual appearance of alkali sorbents before sorption experiment (grain size: 1.6–4 mm).

3.4.3 Quantification and calibration of KCl concentrations using MBMS

Calibration measurements were carried out to correlate the signal intensity measured at the MBMS with the respective KCl concentrations. The experimental setup corresponded to the one for KCl sorption, with the exception of the absence of sorbent. Furthermore, the temperature of the KCl source was increased step by step over several empty tube measurements.

The KCl concentration in the syngas of an empty tube measurement was determined via the weight loss of the KCl source. For this purpose, the loaded sample boat was weighed before and after the measurement at room temperature. The duration of an empty tube measurement depended on the selected temperature. Due to the extremely low KCl concentrations (< 0.3 ppm_v), an empty tube measurement lasted up to 28 h. For the correlating measurement signal, mass spectra were recorded on the (MBMS).

The masses 74 and 76 can be directly assigned to $K^{35}Cl^+$ and $K^{37}Cl^+$, respectively. Furthermore, the masses 35, 37, and 39 show the presence of the KCl fragments $^{35}Cl^+$, $^{37}Cl^+$, and $^{39}K^+$. Since chlorine reacts to HCl in the presence of water, signals can also be measured on masses 36 and 38. On the masses 56 and 58, which correspond to KOH and $K^{18}OH$ respectively, no significant signal increases can be observed. The quantification of the potassium chloride is carried out via mass 39, since it has the highest intensity.

Since the following investigations should clarify whether the targeted KCl concentration can be achieved by means of sorptive hot gas cleaning, the calibration measurements concentrated on the range around 1 ppm_v. The empty tube measurements to establish the intensity-concentration correlation were carried out at the temperatures listed in Table 3.4. The correlations resulting from these measurement points are shown in Figure 3.8 and Figure 3.9. The intensities belonging to the temperature range between 565 °C and 590 °C are in the range of the background noise and were therefore not used in the correlation.

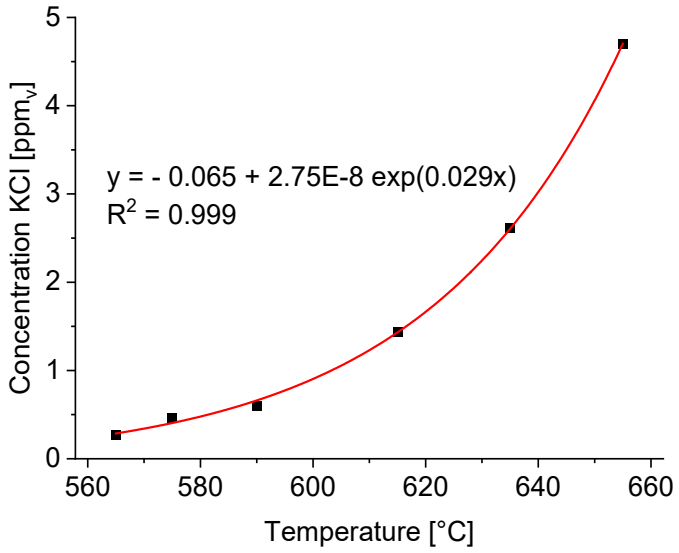

Figure 3.8: Correlation between KCl concentration in the syngas and temperature.

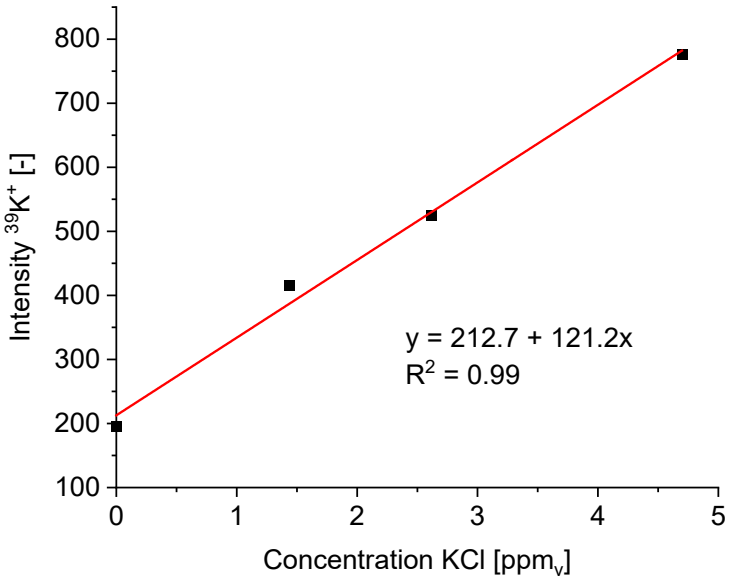

Figure 3.9: Correlation between signal intensity on mass 39 and KCl concentration in the syngas.

Table 3.4: Correlation between KCl concentration and intensity of $^{39}KCl^{+}$.

Temperature [°C]	Concentration KCl [ppm_v]	Intensity $^{39}KCl^{+}$ [-]
650	0 (no KCl source)	195
565	0.27	-
575	0.46	-
590	0.60	-
615	1.44	415.77
635	2.62	524.89
655	4.70	776.18

3.4.4 Experimental setup for H_2S and HCl sorption

A new test rig consisting of a glass reactor, various gas pipes and a water vaporizer was set up. Figure 3.10 shows the main components of the test rig and the individual components of the glass reactor, which was specifically designed for this test rig.

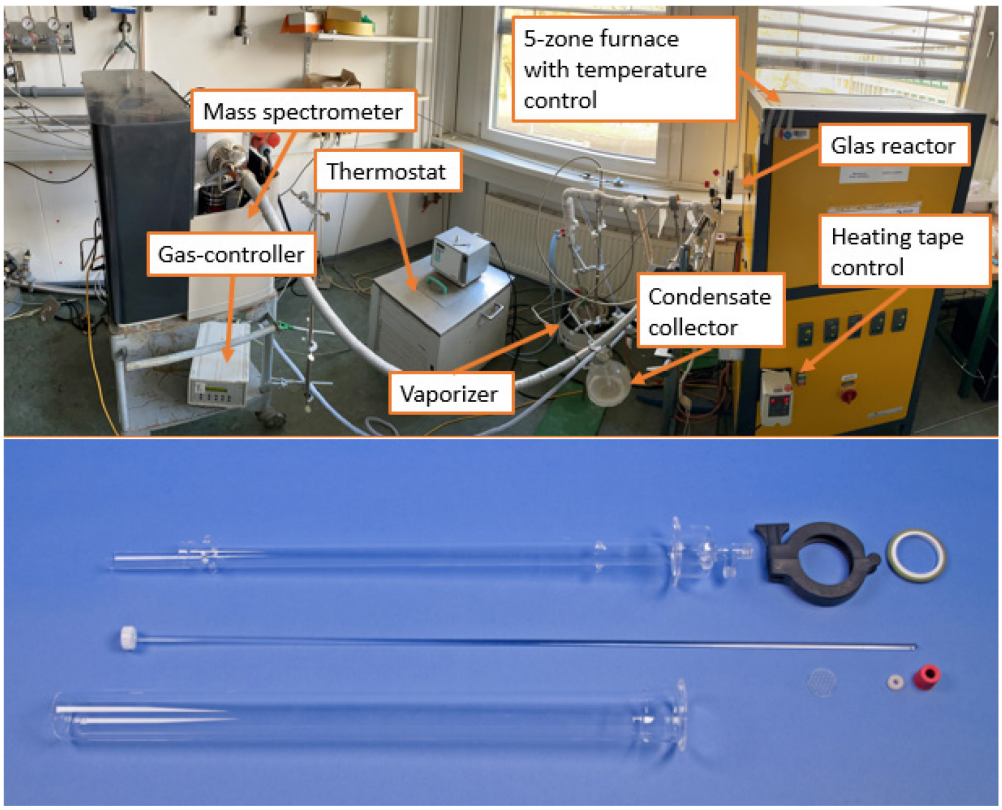

Figure 3.10: H_2S sorption test rig and glas reactor.

A programmable furnace (AGNI Wärme- und Werkstofftechnik GmbH, Model: GHT-130-40-400-5H) was used to obtain a temperature-controlled operation for the sorption experiments. The furnace temperature was controlled via a PID controller acting on the temperature from the thermocouple integrated in the furnace (closed-loop control).

Qualitative hot gas analysis was performed using mass spectrometry (MAX300, Extrel). The gas composition in the H_2S-sorption experiments was set to 73 % H_2, 13 % Ar, 7 % H_2O, 1 % CO_2, 6 % CO, and 60 ppm_v H_2S. This composition was based on the gas modeling presented in Chapter 4.1.2. Since the H_2S sorption can be influenced by several syngas components, the H_2S was mixed in with CO (0.1 %). The inert components (N_2) and the hydrocarbons (mainly CH_4) were substituted by Ar. Because of the expected low H_2S concentration of the gas after H_2S purification, the H_2S signal was determined with an electron multiplier. For the remaining signals, a faraday detector was used.

The H_2S sorption measurements always proceeded in the same way. First, the glass reactor filled with sorption material was flooded with argon. In the second step, the reactor was disconnected from the gas supply by closing the valves immediately upstream and downstream of the reactor. The argon gas flow was then used to purge the pipelines (the gas flow was not yet loaded with water). The CO/H_2S supply was then started. Since the H_2S molecule adsorbed well on surfaces, a steady-state signal was obtained by waiting until the H_2S signal plateaued. Next, the CO_2 stream and the H_2 stream were switched on. The valve to the water supply was opened and the heating of the water started. The gas flow is thus directed onto the water surface from above. After the first steam bubbles appear, the gas (H_2, CO_2, Ar) is directed through the water and loaded. Subsequently, the gas mixture is passed through the reactor. At the end of each experiment, the water supply is stopped and the reactor is flooded with argon.

Similar to the KCl sorption experiments, the HCl contamination was generated by evaporating a solid (here: NH_4Cl) in an Al_2O_3 boat at a fixed temperature during the experiment. The filled boat was attached to the glass rod of the reactor with a metal wire. To fix the sorption material in the glass tube, a foam was used as in the KCl sorption experiments (see Figure 3.11).

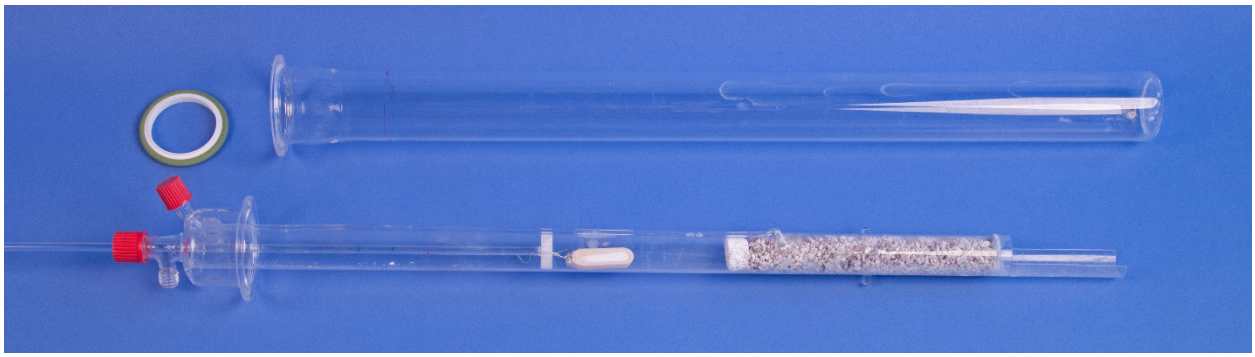

Figure 3.11: Glass reactor filled with SrO with additional HCl source.

The experimental setup for HCl sorption differed only slightly from the experimental setup for H_2S sorption: Helium was used here for the substitution of CH_4 and N_2. This change was made because Ar has fragments at masses 36 and 38 in addition to the main mass at 40. The main signal of HCl is at mass 36.

Since the temperature profile of the furnace is very steep (a few centimeters in the direction of the furnace interior corresponds to several 10 degrees Celsius), the NH_4Cl was evaporated via a heating belt. The NH_4Cl source was placed in the reactor as far away as possible from the furnace entrance. The heating tape was set to its maximum temperature two minutes before the gas was passed through the reactor.

3.4.5 H_2S and HCl sorbents and their preparation

Table 3.5 lists all the chemicals used for HCl and H_2S sorption. The degree of purity was over 98 % for all chemicals.

Table 3.5: List of chemicals used for H_2S and HCl sorbents preparation.

Chemical	Assay	Supplier	CAS Registry Number
$BaCO_3$	≥ 99%	Thermo Scientific, Schwerte	513-77-9
$CaCO_3$	≥ 99.5 %	Thermo Scientific, Schwerte	471-34-1
CeO_2	≥ 99.5 %	Thermo Scientific, Schwerte	1306-38-3
La_2O_3	≥ 99.9 %	Thermo Scientific, Schwerte	1312-81-8
$SrCO_3$	≥ 98 %	Fischer Scientific, Geel (Belgium)	1633-05-2
Y_2O_3	≥ 99 %	Merck, Darmstadt	1314-36-9
Zn_2TiO_4	≥ 99.9 %	Thermo Scientific, Schwerte	12036-43-0

The sorption properties of a commercially available lime (Sorbacal) from Rheinkalk were also investigated. The chemical composition is given in Table 3.6. The values for the oxides were calculated from the elements measured with ICP-OES. In previous studies, the CaO content was 98.1 wt-%. The lower percentage can be explained by the fact that $Ca(OH)_2$ and $CaCO_3$ have formed during storage.

Table 3.6: Chemical composition of Sorbacal [wt-%].

Sorbent	Al_2O_3	SiO_2	Fe_2O_3	CaO	MgO
Sorbacal	0.2	1	0.2	62.1	0.6

In order to ensure a concentration of 1 ppm_v H_2S in the syngas, conventional sorption materials like ZnO could not be used, as these only show good sorption efficiency at temperatures below 600 °C. Therefore, the Sr- and Ba-based sorption materials developed by Stemmler at Forschungszentrum Jülich were included in the experiments. Stemmler's calculation showed that stabilized Ba-based sorbents keep the 1 ppm_v concentration even in a temperature range between 800 °C and 900 °C [131].

Figure 3.12 shows a slight solubility regarding BaO and CaO at temperatures above 1200 °C. Moreover, all CaO-SrO mixtures above 900 °C are forming a CaO-SrO solution phase. Since increased marginal solubilities exist, mixtures of 90 mol-% CaO and 10 mol-% SrO (or BaO), respectively 10 mol-% CaO and 90 mol-% SrO are used for H_2S sorption.

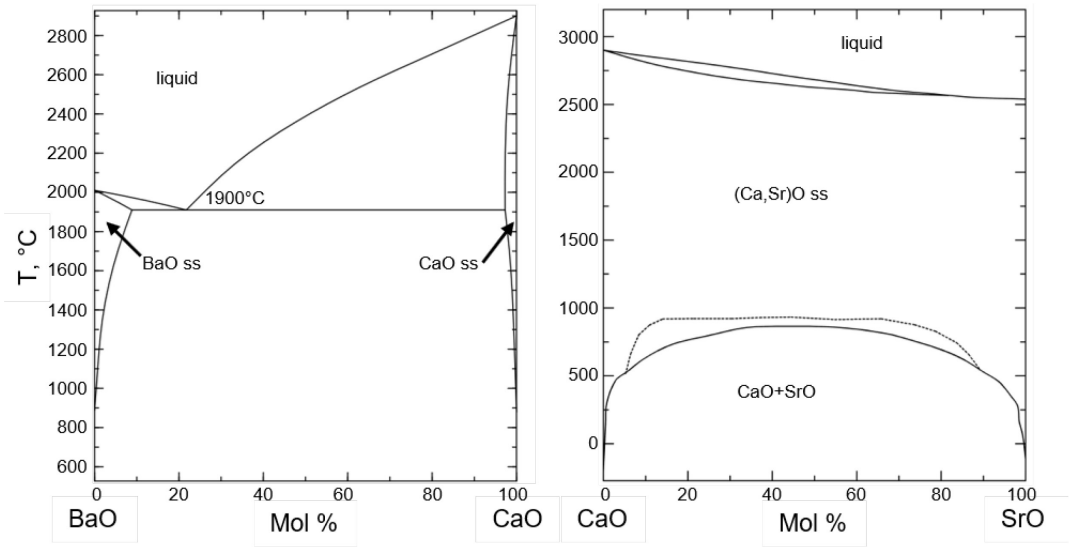

Figure 3.12: Binary Phase-diagram of BaO and CaO (l.) and SrO and CaO (r.) [49,140,131].

For the preparation of the H_2S and HCl sorbents, raw powder ($SrCO_3$, $ZnTi_2O_4$, CeO_2, …) was mixed with water and formed to pellets. For the preparation of the Sr- and Ba-based sorption material, carbonates were used. The TGs of the alkaline earth sorbents (Figure 3.13) were recorded under an air atmosphere. They show that the decomposition reaction of $CaCO_3$ to CaO is completed at about 800 °C to 850 °C, while $SrCO_3$ is completely decomposed at about 1150 °C and $BaCO_3$ at 1200 °C. However, the sorbents used in the sorption experiment were prepared at 1600 °C in platinum crucibles.

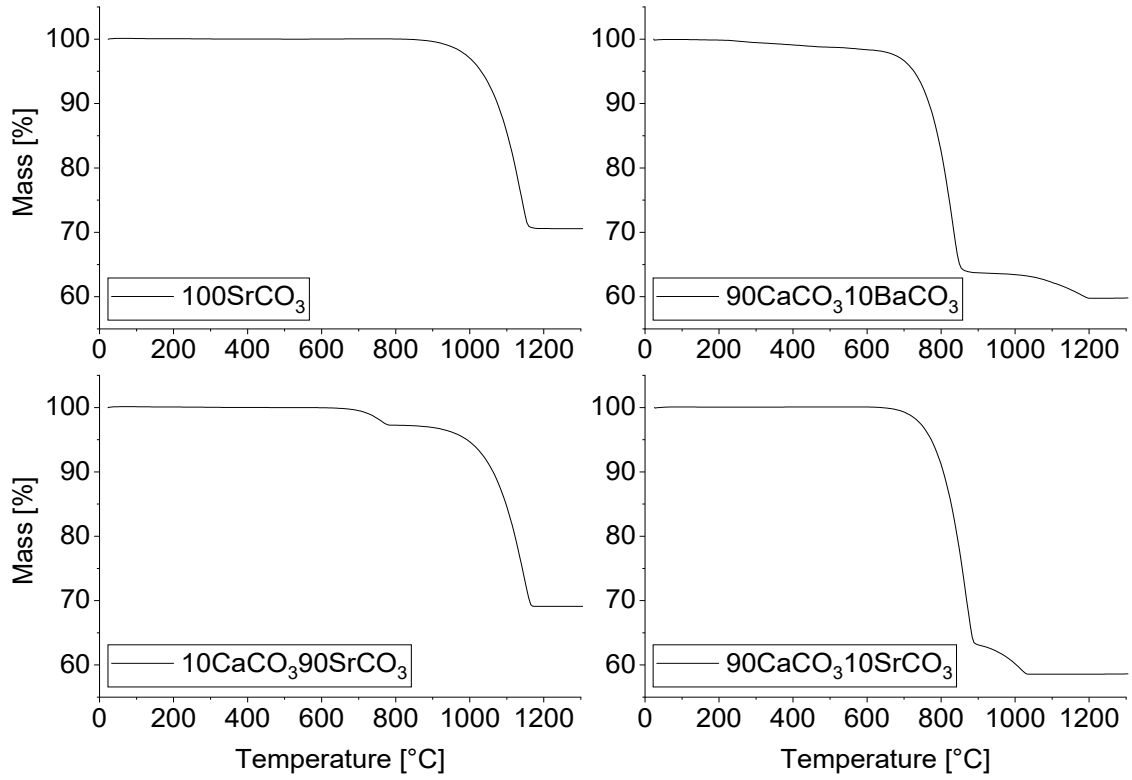

Figure 3.13: Mass loss of $100SrCO_3$, $90SrCO_310CaCO_3$, $10SrCO_390CaCO_3$, and $10BaCO_390CaCO_3$.

A 4-tube furnace was used for the production of reduced ceria sorption material. Raw powder of CeO_2 was mixed with water and was heated in a 10 % H_2-Ar atmosphere at 1500 °C for 72 h. Ce_2O_3 is stable in air if it has been produced at temperatures above 1400 °C [141]. The reduced cerium samples did not show a homogeneous color, but were in a color spectrum between light yellow and light brown (see Figure 3.14). The mineral phase analysis (XRD) of the cerium oxide sorbents used in the experiments are given in Table 3.7. The specific surface area of the most highly reduced cerium oxide sample was determined to be 0.21 m^2/g.

Figure 3.14: Cerium oxide samples after exposure in a 10 %-H_2-Ar atmosphere at 1500 °C for 72 h. Only cerium oxide samples corresponding to picture 1 were used.

Table 3.7: Mineral phase composition of the cerium sorbents [wt-%].

Picture Number	CeO_2	Ce_2O_3
1	16	84
2	19	81
3	30	70
4	100	0
5	100	0
6	100	0

The temperatures and exposure times of the other sorbents can be found in Table 3.8. To ensure a certain mechanical stability of the sorption material, different temperatures and dwell times in the furnace were used depending on the sorption material.

Table 3.8: Manufacturing temperatures and duration.

Sorbent	Temperature [°C]	Duration [h]
La_2O_3	1400	5
Zn_2TiO_4	650	5
CeO_2	1050	10
Y_2O_3	1050	10

In analogy to the KCl sorbents, the specific surface areas of the sorbents were determined by ZEA 3 of Forschungszentrum Jülich (see Table 3.9).

Table 3.9: Specific surface areas of the H_2S sorbents [m^2/g].

Sorbent	Specific surface
Sorbacal	4.778
La_2O_3	0.642
Zn_2TiO_4	0.586
Y_2O_3	1.761
90Ca10Ba	0.878
90Ca10Sr	0.242
10Ca90Sr	0.466
100Sr	0.209

Figure 3.15 provides an overview of all sorbents prepared for the H_2S sorption experiments.

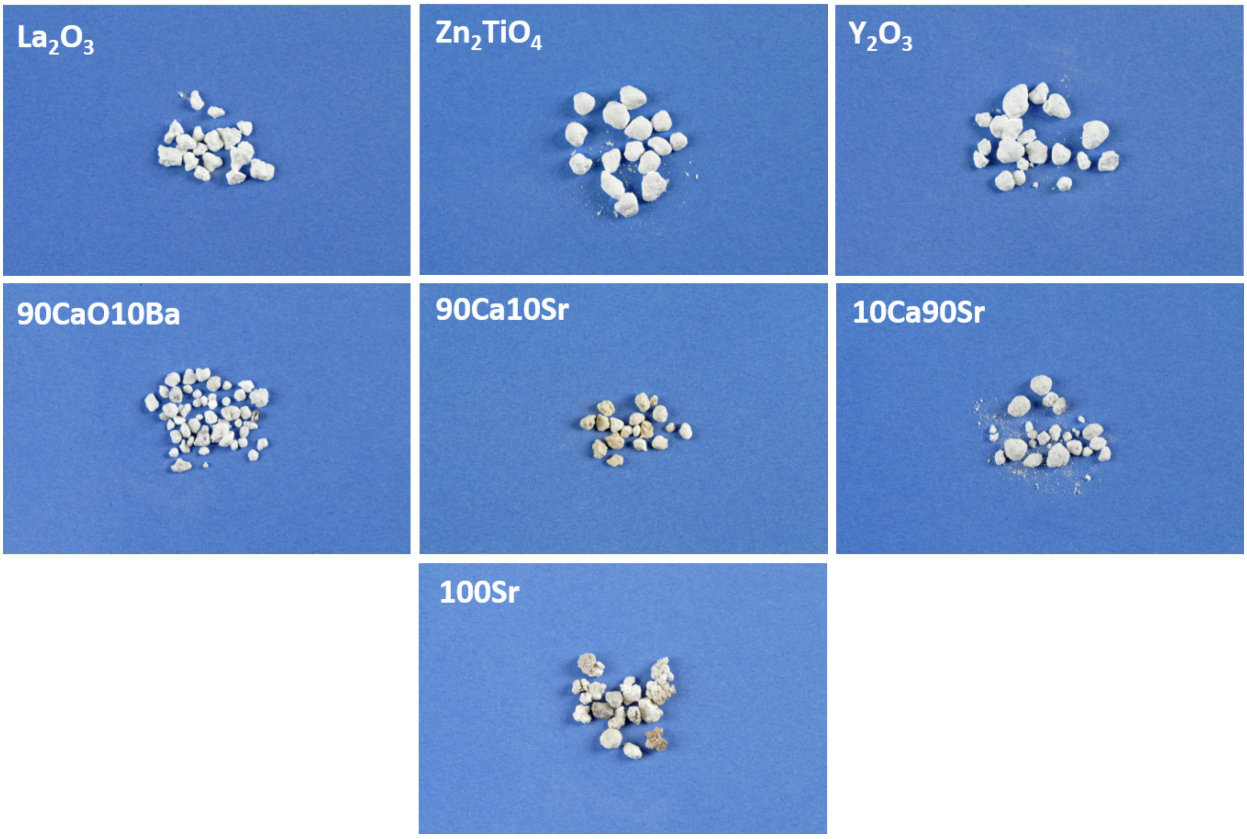

Figure 3.15: Visual appearance of the H_2S sorbents before sorption experiment (grain size: 1.6–4 mm).

3.4.6 Quantification and calibration of H_2S concentrations using MS

As described earlier, the H_2S signal was recorded by mass spectrometry. Before starting the H_2S investigations, the signal intensities were correlated with the corresponding H_2S concentrations. In analogy to the KCl calibration (Chapter 3.4.3), empty pipe measurements were carried out.

Since a syngas purity of less than 1 ppm_v H_2S was aimed for, H_2S concentrations of 60 ppm_v, 30 ppm_v, 10 ppm_v, 5 ppm_v, 2.5 ppm_v, 1 ppm_v, and 0 ppm_v were chosen as calibration points. Since H_2S was mixed with CO, a decrease in the H_2S input current was accompanied by a decrease in the CO input current. The syngas fraction missing due to the reduction of the H_2S concentration was substituted by Ar. The syngas compositions used for calibration are given in Table 3.10. Since the CO content will be reduced to 0.1 %,

the calibration of the H_2S required a high total flow rate. Accordingly, a total flow rate of 2 l/min was used for the calibration.

Table 3.10: Syngas compositions used for H_2S calibration with a volume flow rate of 2 l/min [vol-%].

H_2S concentration [ppm_v]	CO	Ar	CO_2	H_2	H_2O
60	6	13	1	73	7
30	3	16	1	73	7
10	1	18	1	73	7
5	0.5	18.5	1	73	7
2.5	0.25	18.75	1	73	7
1	0.1	18.9	1	73	7
0	0	19	1	73	7

The empty tube measurements with the syngases from Table 3.10 result in the correlation between H_2S concentration and signal intensity at mass 34 shown in Figure 3.16.

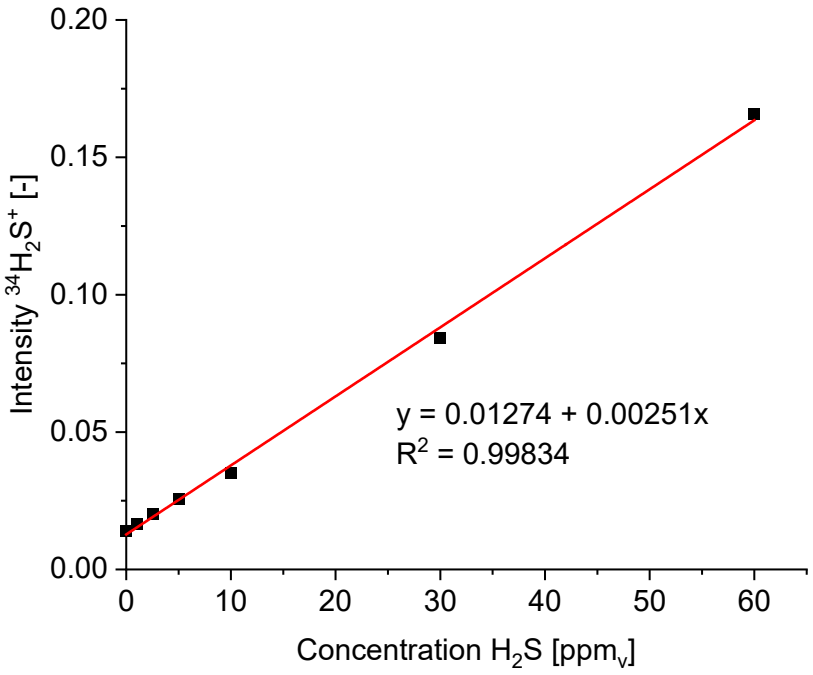

Figure 3.16: Correlation between the signal intensity at mass 34 and the H_2S concentration.

3.4.7 Quantification and calibration of HCl concentrations using MS

According to the KCl and H_2S calibration, a correlation between signal intensities and HCl concentrations was conducted prior to the HCl sorption experiments. An empty pipe calibration was carried out similar to the KCl calibration. Due to the precise positioning of the NH_4Cl source inside the reactor, evaporation of NH_4Cl by the heating tape was difficult. Therefore, a two-point calibration was used. For calibration, a signal of 0.012 was measured without a source (0 ppm_v), and a signal of 0.057 was measured at 148.94 ppm_v at mass 36.

3.5 Experimental setup for the investigation of sorbents-filter candle compatibility and sample preparation after exposure

In order to be able to make statements about the sorbent-filter candles compatibility, two different types of samples were exposed: (1) Pellets consisting of equal parts (wt-%) of sorption material and filter candle material as well as (2) filter candle pieces embedded in sorption material.

The sorption material was ground to a fine powder before being mixed with the filter candle material. The samples were placed in Al_2O_3 boats. Figure 3.17 shows an example of boats prepared with pellets and filter candle pieces.

Figure 3.17: Filter candle pieces embedded in sorption material (l.) and filter candle-sorbents pellets (r.) before exposure.

Two different types of filter candles were used in the investigations made of Ca-Mg silicate fiber and Al-oxide silicate fiber. A photo of the two filter candles can be found in the appendix (see Figure A.1). Table 3.11 shows the composition of the filter candles before exposure.

Table 3.11: Composition of the two filter candles investigated in the sorbents-filter candle compatibility experiments [wt-%].

Component	Ca-Mg silicate fiber	Al-oxide silicate fiber
Al_2O_3	4.18	51.20
SiO_2	59.90	46.85
Fe_2O_3	2.24	0.20
Na_2O	0.70	0.13
CaO	27.84	0.07
MgO	1.28	0.01

Figure 3.18 shows the corresponding XRD analysis. Basically, three phases could be detected: $CaSiO_3$, SiO_2, and Diopside ($CaMgSi_2O_6$) for the Ca-Mg silicate fiber and Al_2O_3, SiO_2, and Mullite ($Al_{2.34}Si_{0.66}O_{4.83}$) for Al-oxide silicate fiber.

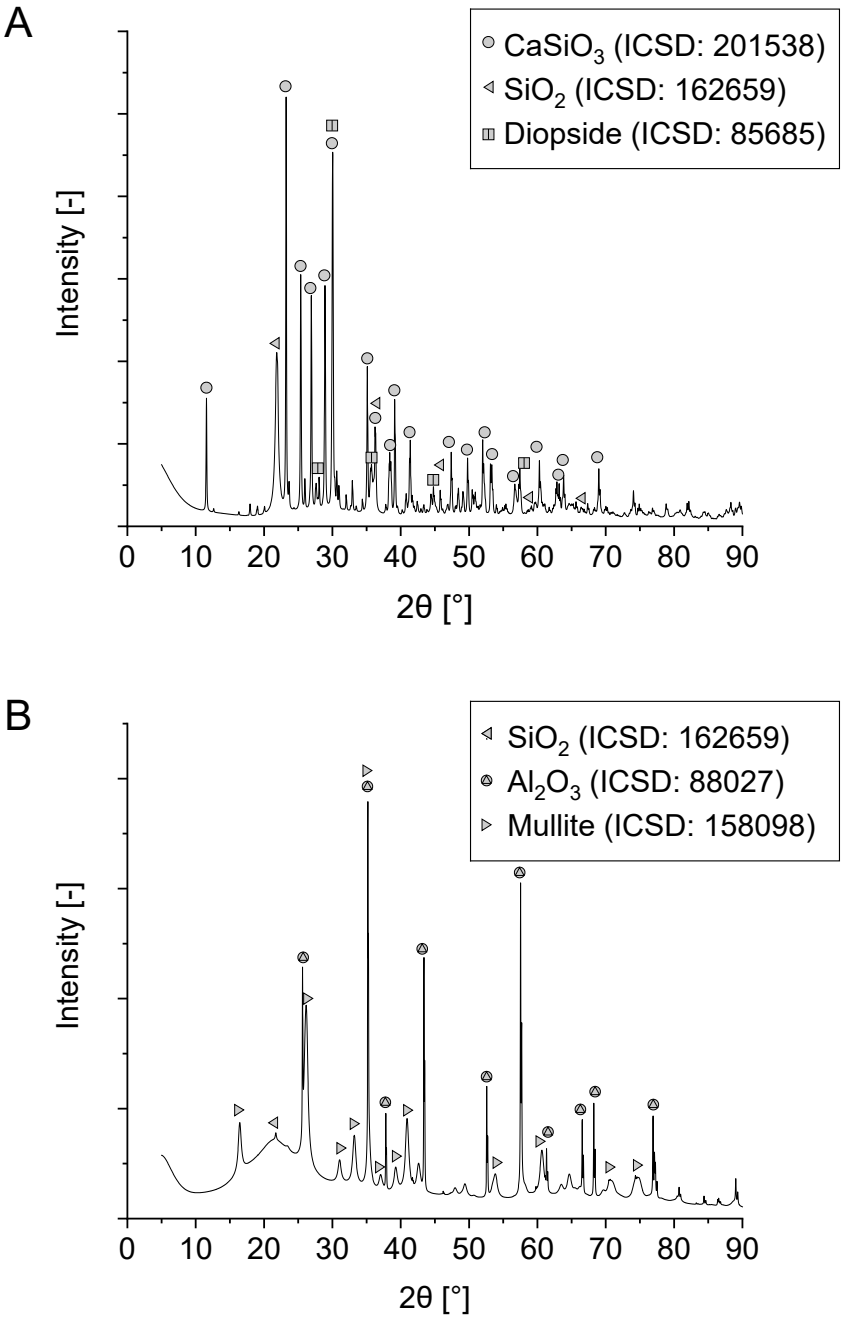

Figure 3.18: XRD analysis of the filter candles used for the exposure experiments: Ca-Mg silicate fiber (A) and Al-oxide silicate fiber (B).

All exposure experiments were carried out in a 4-tube furnace from Prüfer. This furnace essentially consists out of four Al_2O_3 tubes which are operated at 650 °C (gasification temperature).

The gas control technology used in the experimental setup consists of an 8-channel flow computer and mass flow controllers. A heater from Thermo scientific was used to heat the water, while the temperature in the reflux condenser was controlled by a circulating thermostat from Julabo to adjust the humidity of the atmosphere. Table 3.12 shows the volume flow rate of the gases used in the storage facilities. These are derived from the modeling results in Chapter 4.

Table 3.12: Primary gas composition during exposure. A one-point calibration was performed for the gases.

Gas	Volume flow rate [ml/min]
H_2	292
Ar	52
H_2O	28
CO (0.1 % H_2S)	24
CO_2	4
Total:	400

To create a clear-cutting edge for the microscopic, SEM, and EDX analysis, the filter candles had to be prepared. For this purpose, the samples were initially embedded cold into epoxy resin (SpeciFix Resin from Struers). A fairly low viscosity embedding medium for the embedding of the porous specimens was used. The samples are poured under vacuum so that the embedding agent penetrates into the pores of the samples. After the resin hardened, they were prepared in a cross section. For this purpose, the cross-sections of the surfaces are first exposed and then levelled with SiC sandpaper.

Figure 3.19 shows an example of a filter candle embedded in the epoxy resin.

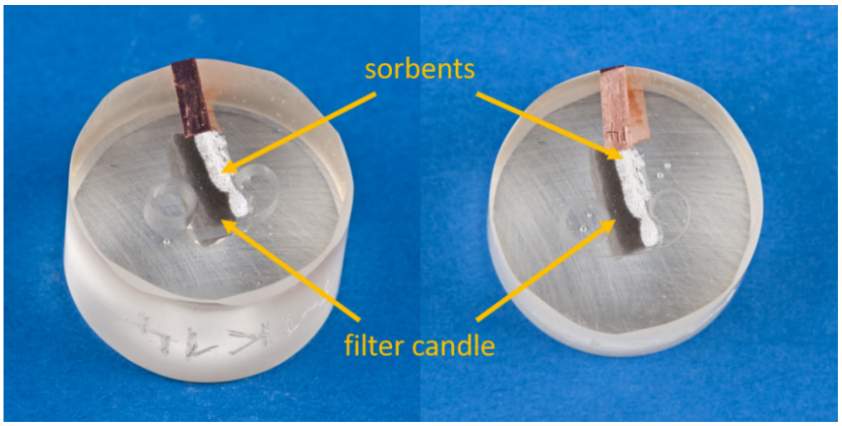

Figure 3.19: Side view (l.) and top view (r.) of the filter candle after exposure embedded in epoxy resin.

The tablets were ground up in a mortar after the exposure experiments. For analysis using XRD, a grain size of 100 nm to a few µm was necessary.

All XRD, microscopic, SEM, and EDX analyses were carried out by the analytical department of IEK-2 at Forschungszentrum Jülich.

4 Simulation results of biomass gasification, calcination, and HGC

This chapter summarizes all calculations carried out with FactSage. As described in the previous chapters, the calculations include the steam gasification calculations, the syngas-CaO calculations, the calcination calculations, and the hot gas cleaning calculations. A corresponding focus was placed on the risks and potentials of the different biomasses during gasification.

4.1 Simulation results of biomass gasification (SEG)

In order to better understand the influence of primary sorption by means of CaO in the gasification unit, the calculated concentrations before and after the CaO reaction are listed in this chapter. Since CaO does not only have an influence on the CO_2 concentration in the syngas, but also reacts with other gas components (e.g. H_2S, HCl, etc.) the trace substance behavior must also be considered.

4.1.1 Gasification without CaO

By referring to the input conditions of the gasifier described in Chapter 3.2 and the biomass composition presented in Table 3.1, the simulation results on the syngas compositions shown in Figure 4.1 and Figure 4.2. Due to the high differences in concentration, the main components (H_2, CO, H_2O, CO_2, CH_4, N_2) of the syngas are listed separately from the trace substances. Regarding the main components produced during the steam gasification at 650 °C, Figure 4.1 shows a fairly homogeneous composition of the syngas, irrespective of the biomass. On average, the syngas before the reaction with CaO consists of approximately 45.9 % H_2, 20.0 % CO, 14.7 % H_2O, 13.3 % CO_2, 5.0 % CH_4, and 0.7 % N_2.

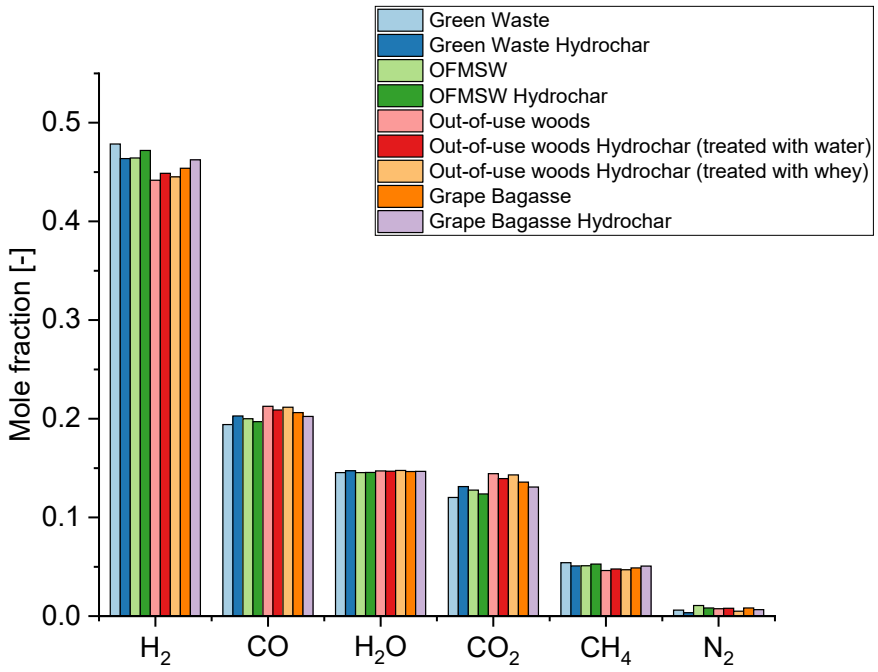

Figure 4.1: Concentrations of the main components in syngas during gasification without CaO (650 °C, 1 atm).

The presentation of trace substances in Figure 4.2 is limited to those alkali, sulfur, and chlorine species that have a concentration above 0.10 ppm_v. Due to the immense differences in concentration of the individual trace species, the dependence on the biomass is directly recognizable: Those syngases with high concentrations of a trace species usually exceed those with low concentrations many times over. Thus, the HCl concentration in the syngas from Green Waste (734 ppm_v) and from its hydrochar (301 ppm_v) clearly exceeds that of Grape Bagasse or Grape Bagasse Hydrochar with less than 1 ppm_v according to the Cl content in the biomass. The high Si content in some biomasses favors the forming of solid compounds with K, Na, and Ca (e.g. $CaSiO_3$, $KAlSi_3O_8$, $NaAlSi_3O_8$), leaving Cl for the reaction to HCl. Thus, the low HCl concentrations of Out-of-use woods, Out-of-use woods Hydrochar (treated with whey), Grape Bagasse, and Grape Bagasse Hydrochar result partly from the low Si concentrations of the biomasses.

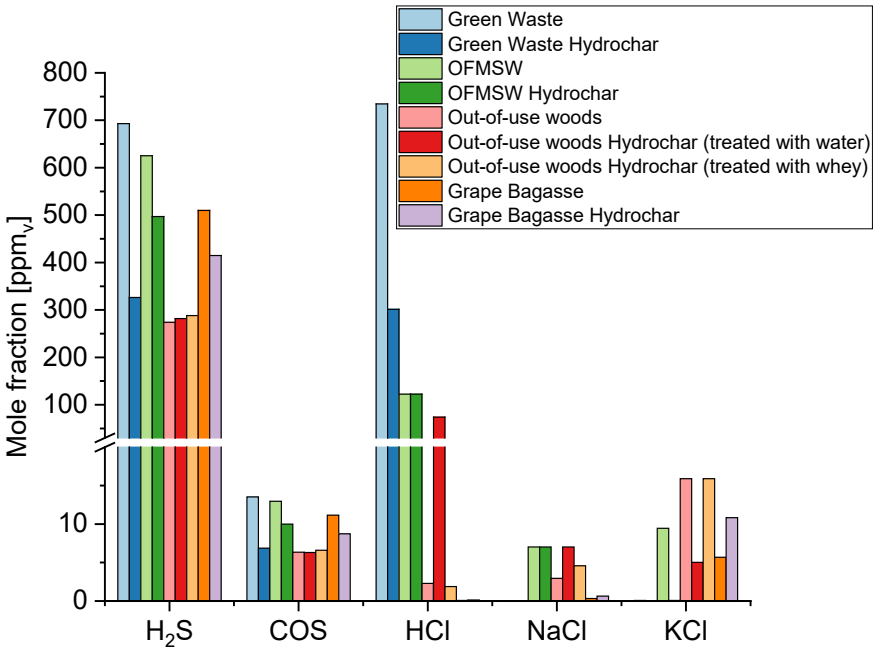

Figure 4.2: Concentration of alkali, chlorine, and sulfur species in the simulated syngas without CaO (650 °C, 1 atm).

Due to the reducing atmosphere in the gasifier, oxidation of the sulfur bound in the biomass is almost completely prevented. As a result, the majority of the sulfur appears in the form of hydrogen sulfide (H_2S), as can be clearly seen in Figure 4.2. The H_2S concentration released is ranging from 281 ppm_v in the syngas from Out-of-use woods Hydrochar (treated with water) to over 692 ppm_v in the syngas from Green Waste. Due to the equilibrium reaction with CO_2 (reaction 4.1), a small amount of sulfur is also bound in carbonyl sulfide (COS).

$$CO_{2(g)} + \ H_2S_{(g)} \leftrightarrow COS_{(g)} + H_2O_{(g)} \tag{4.1}$$

Accordingly, COS concentrations range from 6.3 ppm_v in syngas from Out-of-use woods Hydrochar (treated with water) to 13.5 ppm_v in syngas from Green Waste.

In general, the potassium load in biomasses is higher than the sodium load. This often leads to higher KCl than NaCl concentrations in the syngas.

However, not all biomass components are present in gaseous form at 650 °C under gasification conditions. Table 4.1 puts the mass of the resulting ash in relation with the input mass of the biomass.

Table 4.1: Ash fraction after gasification.

Biomass	Ash fraction [$g_{ash}/g_{biomass}$]
Green Waste	0.3228
Green Waste Hydrochar	0.2043
OFMSW	0.1971
OFMSW Hydrochar	0.172
Out-of-use woods	0.0095
Out-of-use woods Hydrochar (treated with water)	0.0347
Out-of-use woods Hydrochar (treated with whey)	0.04
Grape Bagasse	0.0857
Grape Bagasse Hydrochar	0.0575

As described in Chapter 3.2, the mineral phases were modeled for (steam) gasification conditions. In the first step, the solid stream file resulting from the steam reaction at 650 °C was saved. All phases were then predicted in dependence of the temperature, starting from 400 °C and ending at 1300 °C. The stable phases were grouped into chlorides, sulfides, carbonates, oxides, and silicates. Figure 4.3 presents the calculated phase compositions of the (modeled) project ashes listed in Table 4.1.

The amount of molten slag increases with increasing temperature. Compared to the raw biomasses, the slag formation of the hydrochar ashes barely shifts in temperature. However, the slag amount is clearly decreasing for the investigated hydrochars.

The resulting ashes of Green Waste and Green Waste Hydrochar only consist out of silica and silicates (Figure 4.3, diagrams A+B) at 650 °C. This is consistent with the biomass composition: Green Waste and Green Waste Hydrochar have by far the highest Si content (11.58 wt-% and 6.89 wt-%, respectively). In addition to silicates, OFMSW (C), and OFMSW Hydrochar (D) ashes also contain oxidic phases (mainly $KPMgO_4$ and FeO). Nevertheless, the silicate fraction predominates at 650 °C. Even though almost 40 % of the Na content of the biomass has been leached out after HTC, the OFMSW Hydrochar still has an extremely high Na content (0.48 %) which is reflected in the ash. At 801 °C, the sodium chloride formed in the ash begins to melt and is present in the liquid form. In

the case of untreated OFMSW, this would be prior to the formation of the slag phase. Due to the extremely high Ca, P, and Mg contents in the initial biomass, corresponding compounds (e.g. OFMSW: $CaK_4P_2O_8$, $KPMgO_4$, $KSiAlO_4$, OFMSW Hydrochar: $KPMgO_4$, $CaKPO_4$) are formed which prevent the formation of KCl.

Grape Bagasse (E) and Grape Bagasse Hydrochar (F) have a low ash content compared to other biomasses. This is mainly due to the extremely low Si content in the biomass. Since these biomasses have extremely low Ca and Cl concentrations, the ashes of Grape Bagasse and its hydrochar form carbonates. Due to the high potassium content, mainly K_2CO_3 and $K_2Ca(CO_3)_2$ predominate, but Na_2CO_3 is also present in the ash at lower temperatures. The formation of slag is favored by the high potassium content.

For the pretreated Out-of-use woods samples (G, H, I), a different trend can be seen than for the other hydrochars. Due to the HTC-pretreatment with whey (I), the K, Na, Si, Fe, and Ca content increased compared to the raw biomass. This leads to a very developed KCl phase at 650 °C. Due to the high K and Si, the biomass pretreated with whey results in early slag formation at approximately 650 °C.

Table 4.2 shows the proportion of the slag phase in relation to the mass of the condensed phase at gasifier temperature (650 °C) and calciner temperature (920 °C). At 650 °C, Grape Bagasse and Grape Bagasse Hydrochar exhibit extremely high slag formation with a proportion of over 90 wt-%. For Out-of-use markus2woods Hydrochar treated with whey (I), a low formation of < 1 wt-% of slag is recognizable. The remaining biomasses do not yet form slag at 650 °C. At 920 °C, however, all examined biomasses in the model show a slag phase. A high proportion of slag is problematic due to the risk of bed agglomeration. Therefore, slag formation is normally undesirable in furnaces and attempts are made to keep the temperature in the combustion chamber below the ash softening temperature by taking suitable measures (e.g. flue gas recirculation).

The lowest slag content, namely 9 wt-%, is found in Out-of-use woods. Out-of-use wood also has a low ash content in relation to the biomass (see Table 4.1), which makes it the most suitable examined biomass for gasification in terms of slag minimization.

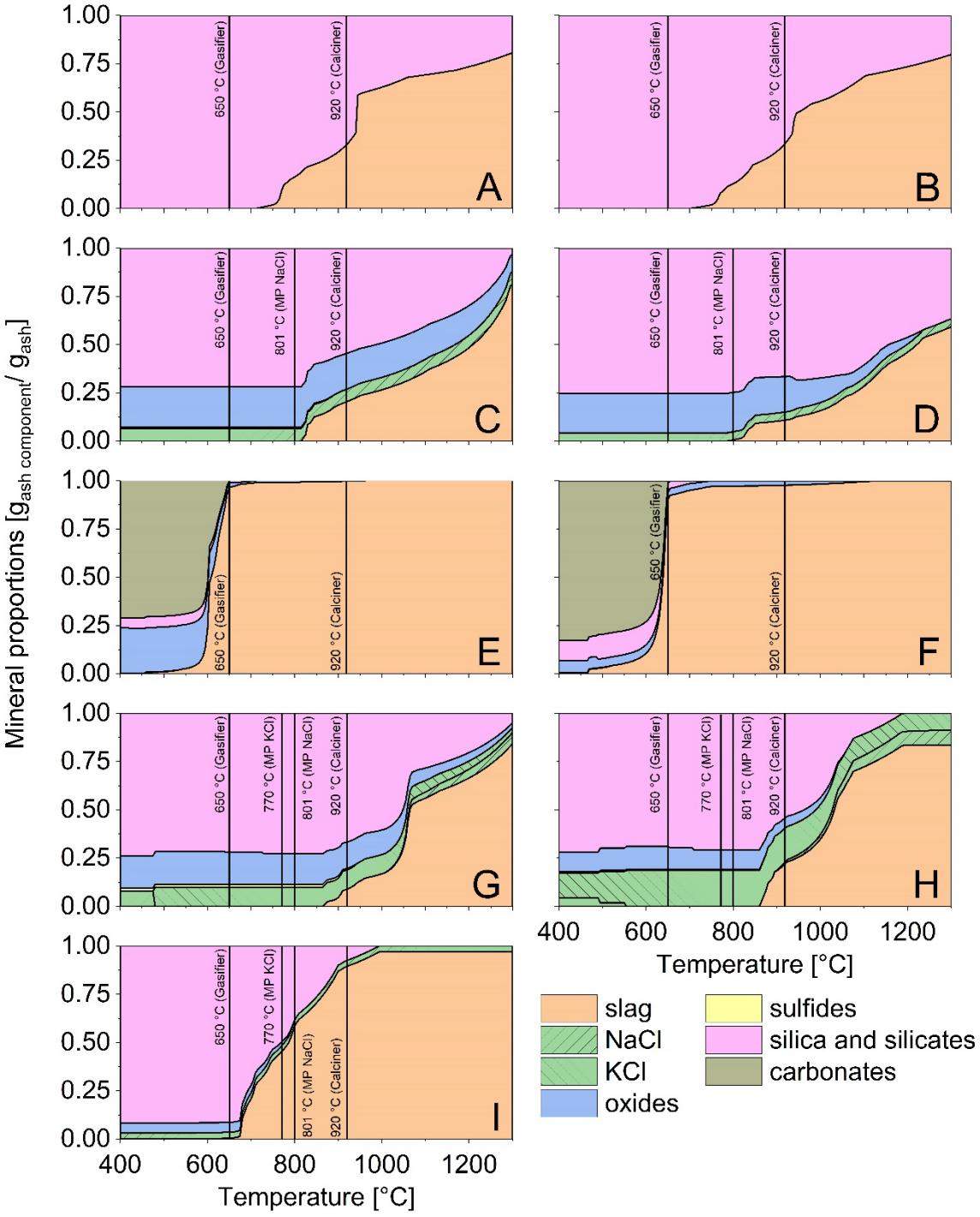

Figure 4.3: Calculated mineral proportions in the ash of (A) Green Waste, (B) Green Waste Hydrochar, (C) OFMSW, (D) OFMSW Hydrochar, (E) Grape Bagasse, (F) Grape Bagasse Hydrochar, (G) Out-of-use woods, (H) Out-of-use woods Hydrochar treated with water, and (I) Out-of-use woods Hydrochar treated with whey under gasification conditions.

Table 4.2: Slag fraction in gasifier at gasification temperature (650 °C) and calciner temperature (920 °C).

Biomass	Slag fraction [$g_{slag}/g_{condensed\ phase}$]	
	650 °C	920 °C
Green Waste (A)	0.00	0.33
Green Waste Hydrochar (B)	0.00	0.34
OFMSW (C)	0.00	0.20
OFMSW Hydrochar (D)	0.00	0.11
Grape Bagasse (E)	0.96	0.996
Grape Bagasse Hydrochar (F)	0.90	0.98
Out-of-use woods (G)	0.00	0.09
Out-of-use woods Hydrochar treated with water (H)	0.00	0.22
Out-of-use woods Hydrochar treated with whey (I)	0.0054	0.89

Figure 4.4 shows the condensation behavior of chlorides of the syngases resulting from the different biomasses. For some of the biomasses (OFMSW, OFMSW Hydrochar, and all of the Out-of-use woods samples), the chlorides (mainly consisting of sodium chloride and potassium chloride) condense directly at temperatures below 650 °C.

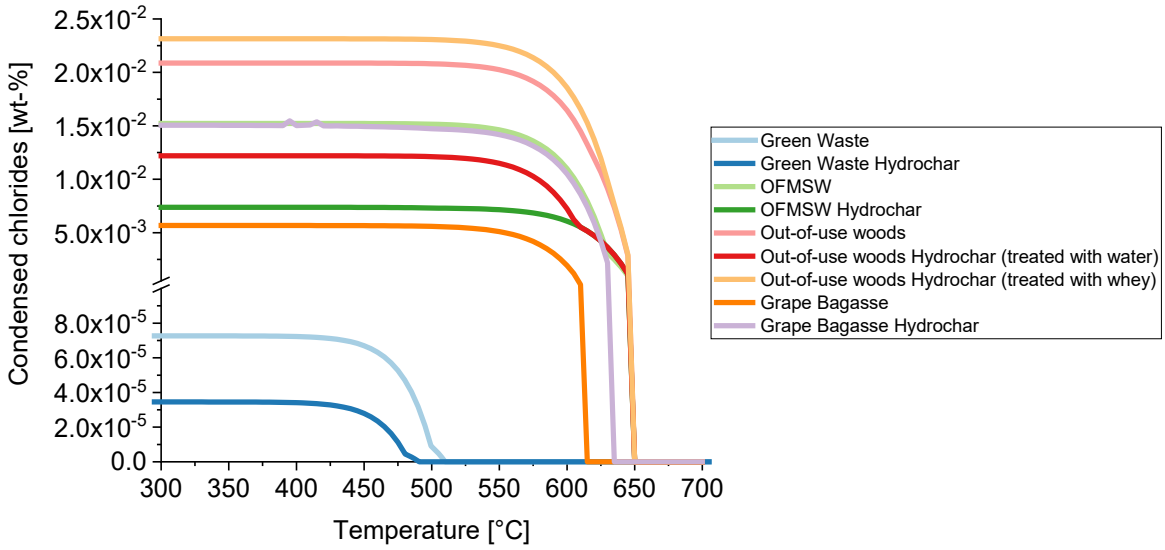

Figure 4.4: Condensation of chlorides after steam gasification at 650 °C and 1 atm. The condensed chlorides consist mostly out of potassium and sodium chloride. The concentrations refer to the input biomass.

This indicates that the gas phase was saturated with the corresponding chlorides, since they also occur in condensed form in the ash. In contrast, the condensation of the chlorides for Green Waste and Green Waste Hydrochar starts at temperatures below 525 °C. The chlorides of the Grape Bagasse and the Grape Bagasse syngas starts to condense at 610 °C and 630 °C, respectively. This statement is consistent with the low NaCl and KCl concentrations shown in Figure 4.2.

For the syngases of Grape Bagasse and Grape Bagasse Hydrochar, the carbonates condense directly at 650 °C. Figure 4.5 shows that for Grape Bagasse Hydrochar most of the carbonate (mainly Na_2CO_3) condenses out during cooling at approximately 500 °C.

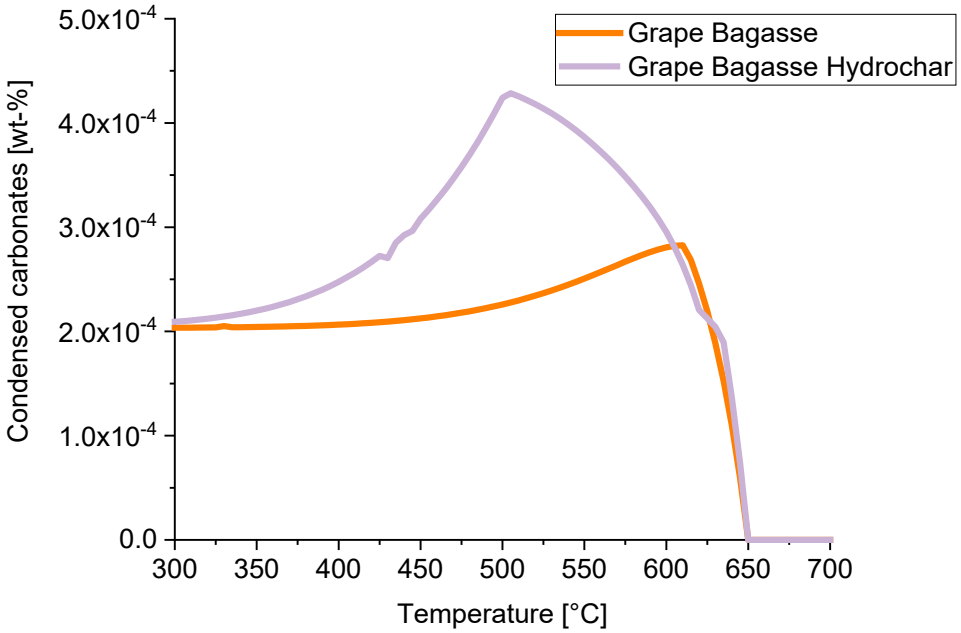

Figure 4.5: Condensation of carbonates after steam gasification at 650 °C and 1 atm. The concentrations refer to the input biomass.

Below this temperature, more NaCl condenses out which causes a maximum in the diagram. In both cases, KCl is the salt component that condenses out first, namely at 630 °C for the syngas of Grape Bagasse Hydrochar and at 610 °C for Grape Bagasse, which explains the decrease in carbonate condensation.

4.1.2 Influence of CaO on the syngas composition and condensation behavior of salts

Since CaO is used as the primary sorption material for CO_2 in the GICO fluidized bed gasification (SEG), the concentrations not only of the main components but also of the sour gas components are changing according to reactions 2.1, 2.5, 2.10, and 2.13.

Figure 4.6 shows that, similar to the syngas concentrations before the CaO reaction, the concentrations of the main components in the gas phase of the different biomasses hardly differ. The CaO reacts with CO_2 in the gas phase to form $CaCO_3$ and thus, lowers the CO_2 concentration in the syngas to approximately 1 %. This is the lowest CO_2 concentration that can be achieved with CaO since CaO is added in excess in the simulation, meaning that the equilibrium in reaction 2.1 cannot be shifted further to the right side. The low CO_2 concentrations shift the equilibrium according to reaction 2.2 to higher H_2 concentrations (approximately 73 %). The elemental nitrogen in the biomass forms mainly inert N_2 (1 %). Moreover, the syngases contains approximately 12 % CH_4, 6 % CO, and 7 % H_2O.

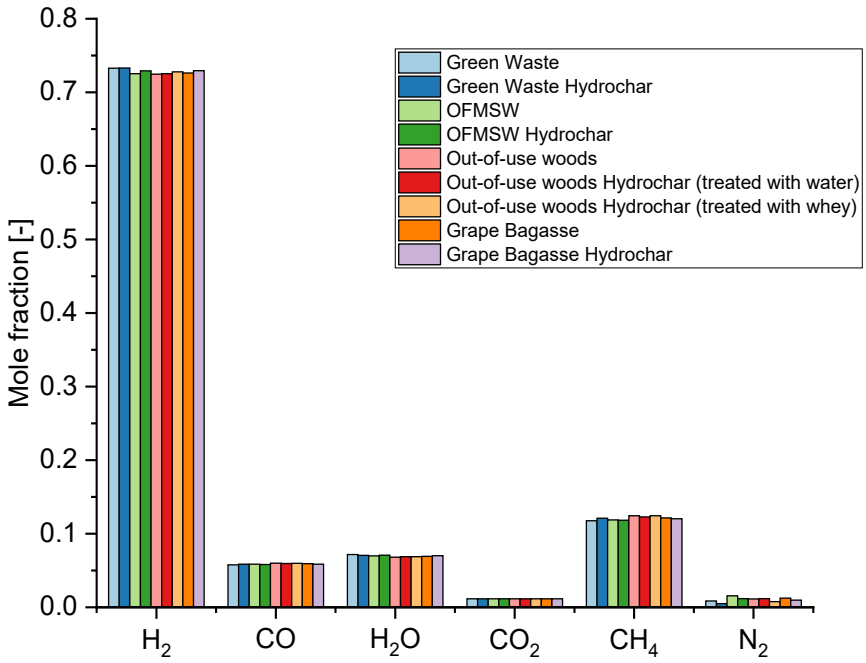

Figure 4.6: Syngas compositions of the main components during gasification with CaO (650 °C, 1 atm).

As described earlier in Chapter 2.3, the CaO has also an influence on the HCl concentration. Since the CaO was added in excess in the simulation, the concentrations shown in Figure 4.7 are the minimum achievable concentrations.

Concentrations of approximately 20 ppm_v are reached for H_2S. The concentration of carbonyl sulfide (COS) even reaches values below 0.1 ppm_v due to reaction 4.2.

$$CaO_{(s)} + \ COS_{(g)} \leftrightarrow CaS_{(s)} + CO_{2(g)} \tag{4.2}$$

The HCl concentrations can be reduced to approximately 160 ppm_v with CaO. Since the HCl concentrations of all Out-of-use woods and Grape Bagasse samples were already low after the steam gasification, they cannot be further reduced. The concentrations for NaCl and KCl found in Figure 4.7 increased for those biomasses, where the syngas was not saturated, due to the reduction of the gas volume after the CaO reaction.

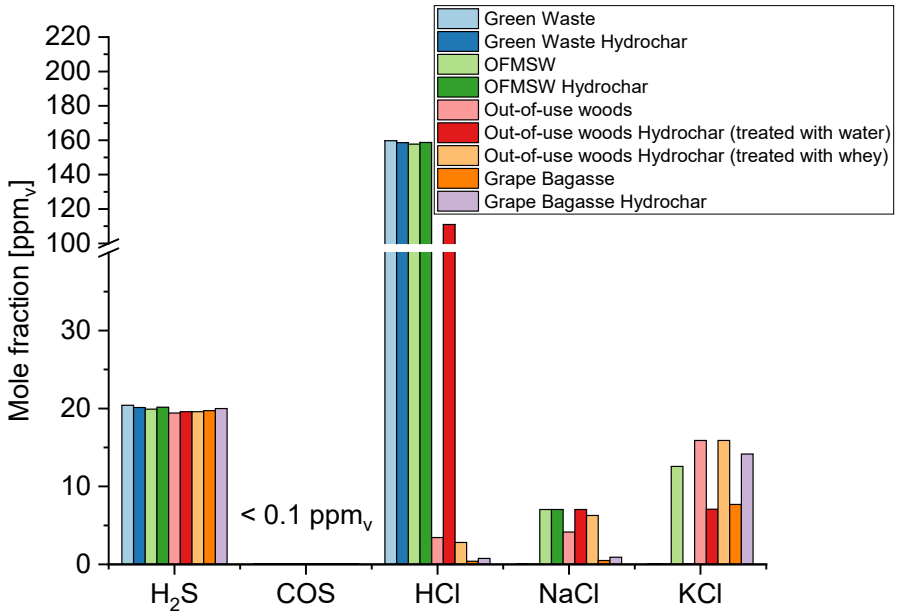

Figure 4.7: Concentration of alkali, chlorine, and sulfur species in the simulated syngas after CaO reaction (650 °C, 1 atm).

Figure 4.8 shows the condensation behavior of the chlorides after the CaO reaction. It can be seen that the condensation temperatures increase due to the increased alkali concentration in the syngas. However, the amount of condensed chlorides tends to decrease only slightly.

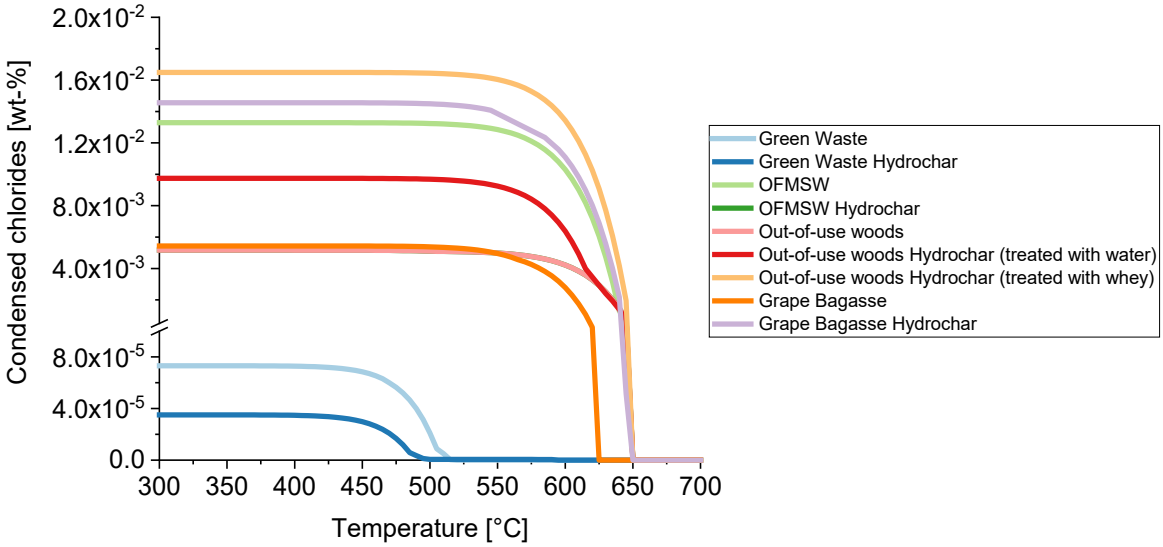

Figure 4.8: Condensation of chlorides (mostly potassium and sodium chloride) after gas-CaO reaction.

Since the concentrations of inorganic trace substances, i.e. H_2S and HCl, achieved with CaO are not yet sufficient or are right at the limit according to Table 2.1, further calculations for hot gas cleaning needed to be carried out on the basis of the calculation results presented in this chapter.

4.2 Simulation results of HGC gasification side

With H_2 concentrations of up to 73 % and CO concentrations of around 6 % the produced syngases have a high potential for use in fuel cells. To find suitable sorbents for the hot gas cleaning of the gasification unit (650 °C, 1 atm), further FactSage calculations were carried out.

The basic concept of hot gas cleaning presented in this work uses alkali cleaning for both sides (gasifier and calciner). Therefore, aluminosilicates are investigated in the calculations. Aluminosilicates have proven to work well in temperature ranges between 700 °C and 1000 °C [49]. Reaction 2.12 shows that HCl is released during alkali sorption. Therefore, the syngas must accordingly be freed from HCl after the alkali cleaning unit. In the following modeling, a combined H_2S-(respectively SO_2, for the calcination side) HCl purification unit is investigated.

4.2.1 Alkali cleaning (gasification side)

As described in the previous chapter, KCl is the most commonly released alkali species during biomass gasification. Due to the high condensation temperatures of KCl directly at 650 °C (gasification temperature) for most of the investigated biomasses (see Figure 4.8), the condensation temperatures of the syngases are determined by the alkali impurities. To reduce the condensation temperature of syngases, the reduction of KCl and NaCl is of particular importance. The simulation results of sorptive alkali hot gas cleaning on aluminosilicates are shown in Figure 4.9.

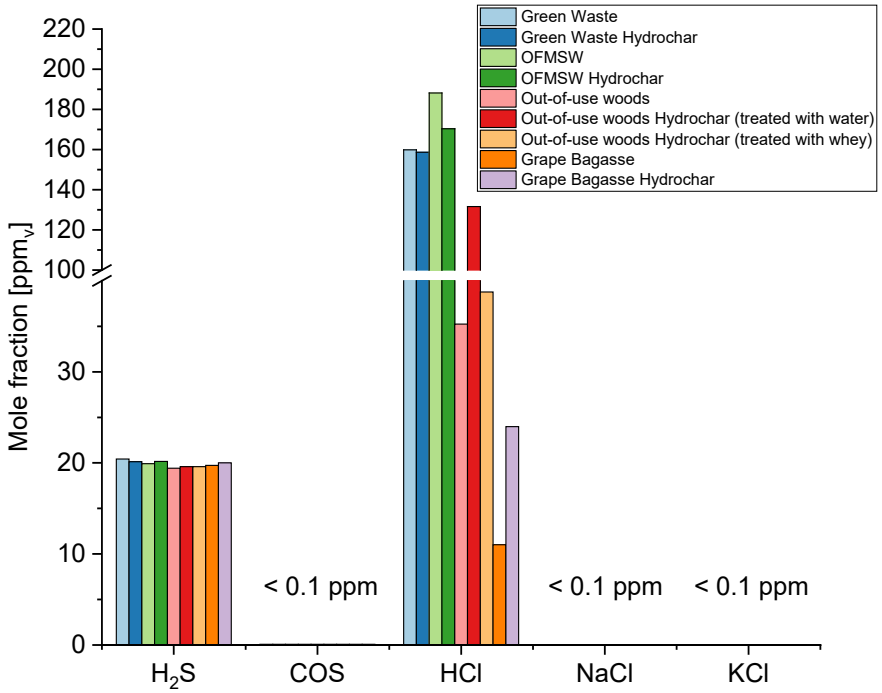

Figure 4.9: Achievable HCl, alkali, and sulfur compound concentrations after alkali cleaning using aluminosilicates in excess (650 °C, 1 atm).

The NaCl concentrations range up to 0.97 ppb_v, while the maximum KCl concentration is 1.5 ppb_v. With concentrations of up to 188 ppm_v, in the purified syngas, the concentration of HCl is the only chlorine species that increases significantly according to reaction 2.12. Since H_2S does not react with aluminosilicates, its concentrations remain unchanged.

The condensation behavior resulting from the remaining alkali concentrations is shown in Figure 4.10. The range of condensation temperatures varies between 380-430 °C.

The use of aluminosilicates not only shifts the condensation temperature by more than 200 °C, but also extremely reduces the amount of condensing chlorides. Since most condensation temperatures are around 430 °C and the amount of water available is several orders of magnitude greater than the alkali salt concentration, it can be assumed that alkali salt reduction has proceeded to the minimum concentration.

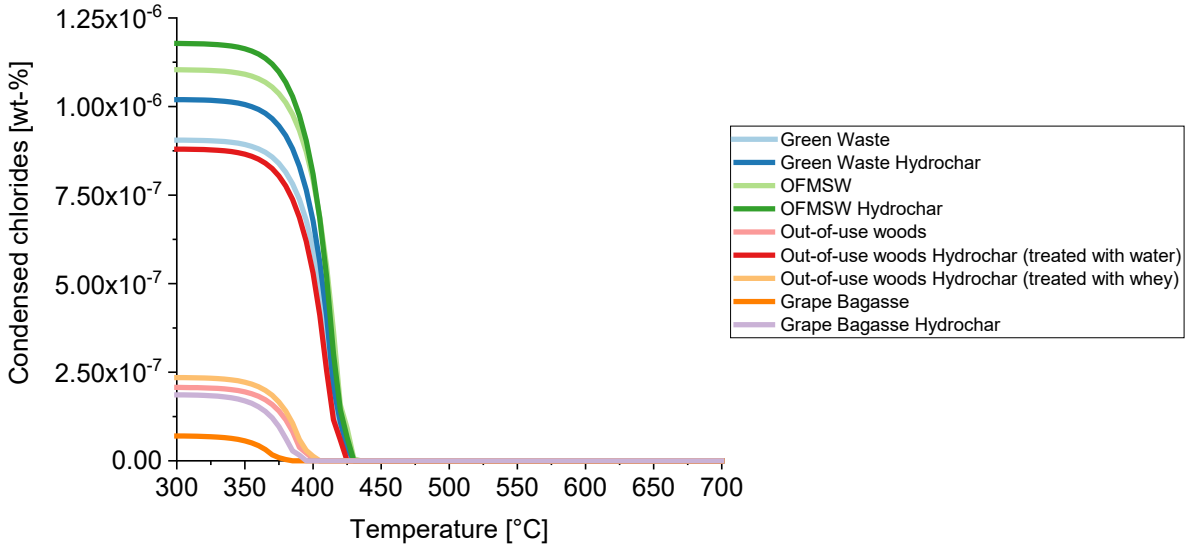

Figure 4.10: Condensation behavior after alkali cleaning. The concentrations refer to the input biomass.

4.2.2 Sour gas cleaning (gasification side)

Based on the results of the alkali cleaning calculations, further calculations for the sour gas cleaning were carried out. Therefore, several metals/metal oxides as well as natural occurring alkali and alkaline earth compounds had been considered. Because the syn-gases have all similar H_2S, NaCl, and KCl concentrations due to the reaction with CaO and the aluminosilicates, the sour gas cleaning was carried out on the basis of the syngas from OFMSW. The modeled syngas from OFMSW has the highest HCl concentration (188 ppm_v).

The results show that SrO, BaO, and Ce_2O_3 are suitable to reduce the concentrations of H_2S from approximately 20 ppm_v to values below 1 ppm_v (SrO: 2.8 ppb, BaO, 0.013 ppb, Ce_2O_3: 1 ppt). These concentrations are all within the range of purities demanded for the use of SOFC in Table 2.1. From a thermodynamic point of view, gas purification can therefore be carried out in the way described. With the help of Zn-based sorption materials (ZnO and Zn_2TiO_4), the H_2S concentration can be reduced to a few ppm_v (ZnO: 5.1 ppm_v, Zn_2TiO_4: 10.4 ppm_v).

Similar statements can also be made about the HCl sorption with the sorption materials mentioned: BaO and SrO sorbents can reduce the concentrations of HCl from around 188 ppm_v to 2.8 ppb and 0.37 ppm_v. Ce_2O_3 reduces the HCl amount to 17.7 ppm_v, while ZnO and Zn_2TiO_4 are not able to reduce the input concentration. Figure 4.11 shows another positive effect of BaO, SrO, and Ce_2O_3 on the syngas. The CO_2 concentrations of

approximately 1 % can be further reduced. This also has the advantage of shifting the equilibrium to higher H_2 concentrations.

It is well known that the reduced form of CeO_2, namely Ce_2O_3, is a good H_2S sorption material [112,142]. Ce_2O_3 forms an oxysulfide (Ce_2O_2S) with H_2S, but also Ce_2S_3 (see reactions 2.7-2.9). The H_2S vapor pressure over Ce_2S_3 is greater than the vapor pressure of H_2S over Ce_2O_2S. However, since the syngas after the CaO reaction has a high H_2 concentration of approximately 73 %, there is the consideration of reducing the cerium oxide in situ according to reaction 2.6.

Figure 4.11 shows that the syngas can be used to reduce CeO_2 (H_2 concentration decreases), but nevertheless H_2S cannot be reduced at 650 °C. This is due to the high water concentration produced during the reduction, which prevents the formation of the sulfides.

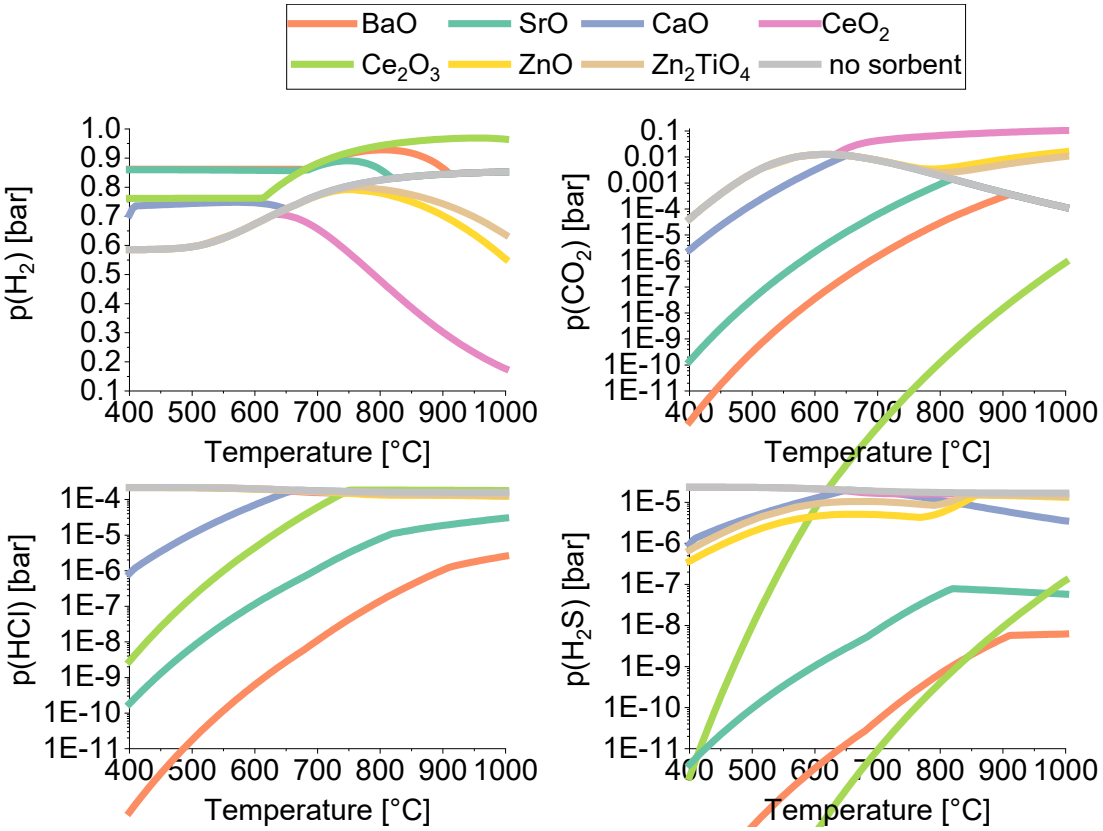

Figure 4.11: Partial pressure of H_2, CO_2, HCl, and H_2S after H_2S/HCl cleaning for different sorbents.

The sorption capacity of BaO- and SrO-based sorption materials with respect to CO_2, H_2S, and HCl can be seen positively over a wide temperature range (400-1000 °C). Ce_2O_3, on the other hand, lowers the HCl concentration significantly only up to about 700 °C.

Since the gas comes into contact with sorption material during hot gas cleaning, a final investigation of the condensation behavior is useful. Figure 4.12, Figure 4.13, and Figure 4.14 show the condensation behavior of the final purified syngas after H_2S-HCl sorption.

Similarly, the condensation starts directly at 650 °C. This means that sorption material was present in excess and therefore all gas-sorbents reactions have taken place. It can be seen that the Ce_2O_3, ZnO, SrO, and BaO have formed chlorides. However, the condensation mass for the Ba- and Sr-sorbents in relation to the biomass is only slightly higher than the condensation mass without purification above 250 °C.

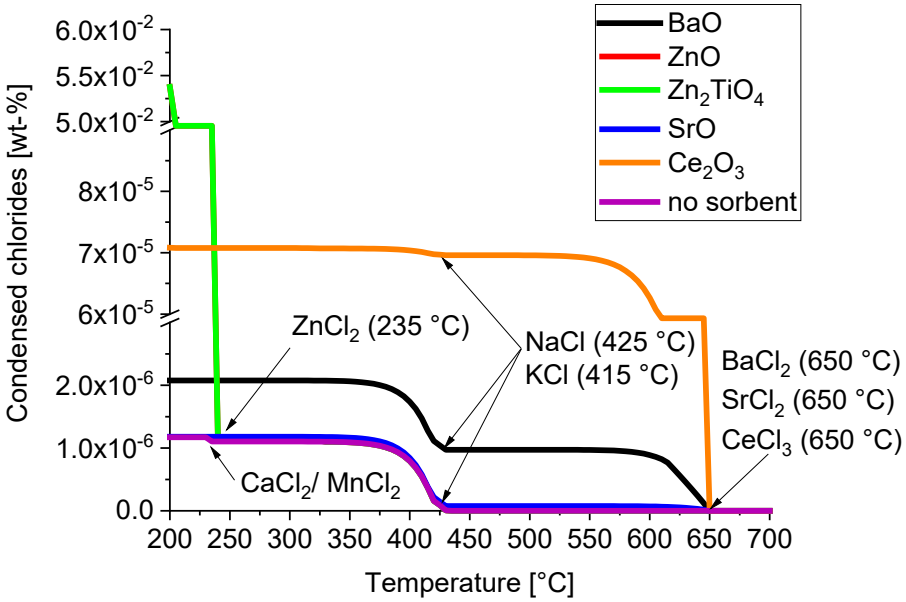

Figure 4.12: Chloride condensation behavior after H_2S/HCl cleaning. The concentrations refer to the input biomass.

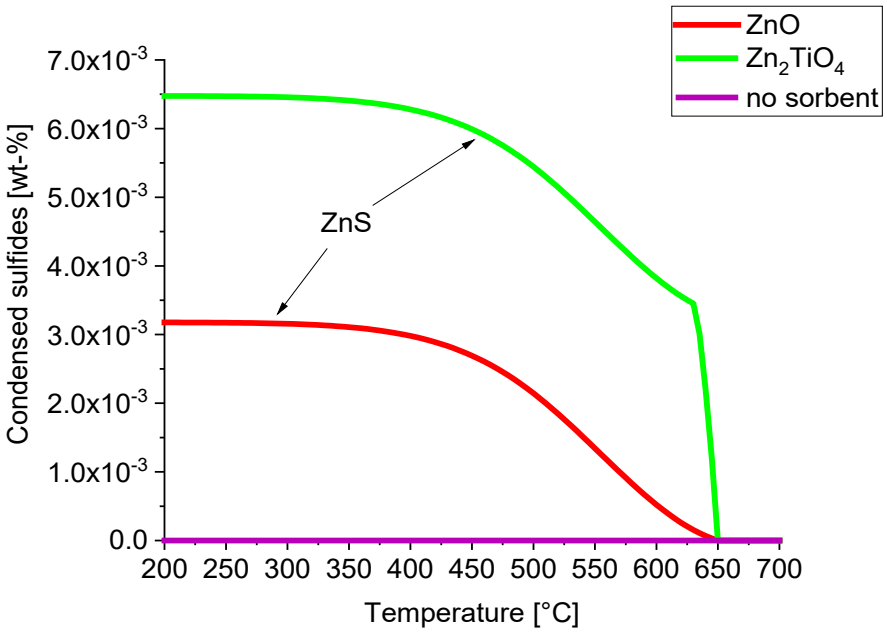

Figure 4.13: Sulfide condensation behavior after H_2S/HCl cleaning. The concentrations refer to the input biomass.

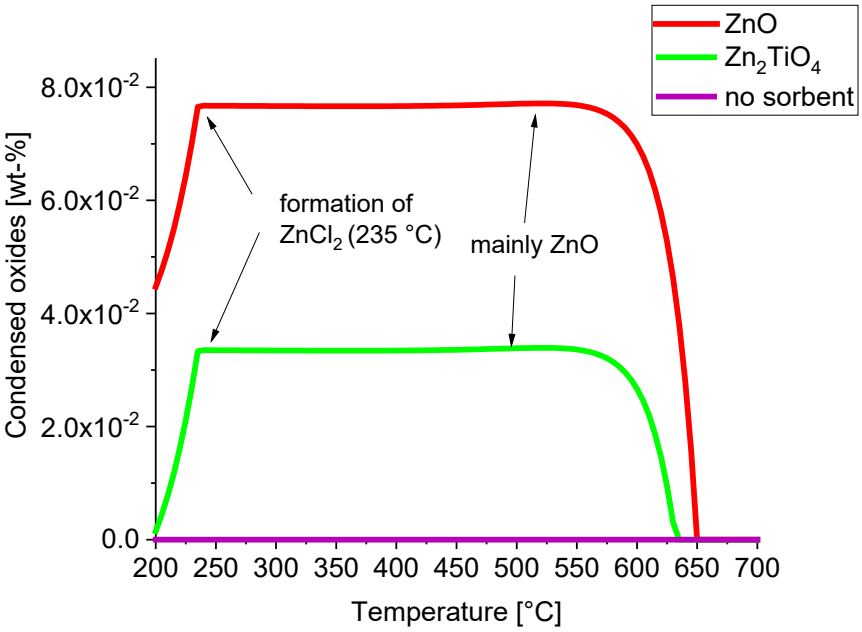

Figure 4.14: Oxide condensation behavior after H_2S/HCl cleaning. The concentrations refer to the input biomass.

Ce_2O_3 also forms a chloride ($CeCl_3$) whose mass after condensation is one order of magnitude higher than that of the other sorbents in the 250-650 °C temperature range. How-

ever, the condensation of zinc compounds such as ZnS, ZnO, and $ZnCl_2$ is very problematic. In relation to the used biomass, these sorbents have a very high proportion in comparison (10^{-3}-10^{-2} wt-%). At low temperatures, more $ZnCl_2$ and less ZnO condenses out.

4.3 Simulation results of calcination

The bed material plays a decisive role in the calciner modeling. Figure 4.15 shows the composition of the bed material under (reducing) gasifier conditions at 650 °C and after calcination conditions at 920 °C. In average over 99.85 wt-% of the CaO is converted to $CaCO_3$ and approximately 0.12 wt-% to CaS in the gasifier. Due to the high Cl and Si content in Green Waste, Green Waste Hydrochar, OFMSW, and OFMSW Hydrochar, $CaCl_2$ is formed. Si is present in excess here and forms silicates with K and Ca, which is why enough Cl is present for the $CaCl_2$ formation.

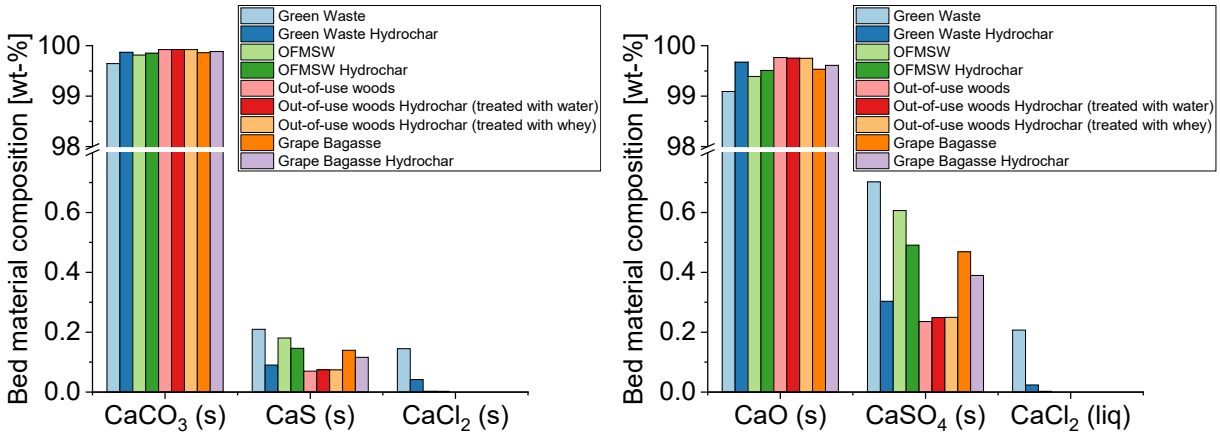

Figure 4.15: Bed material composition after gasification at 650 °C (l.) and after calcination at 920 °C (r.) at 1 atm.

Since $CaCO_3$ is only stable up to approximately 825 °C under atmospheric pressure and decomposes to CaO and CO_2 above this temperature, the bed material in the calciner mainly consists of CaO. In addition, the CaS oxidized to $CaSO_4$. Since the melting temperature of $CaCl_2$ of 772 °C has been exceeded, it is now in liquid form.

CaO that reacts to CaS or $CaCl_2$ will be missing in the next sorption cycle and must be replaced. Table 4.3 gives an overview of the CaO content in the bed material consisting of CaO, $CaCl_2$, and $CaSO_4$. Between 0.91 wt-% (Green Waste) and 0.24 wt-% of the bed material (Out-of-use woods) must be replaced.

Table 4.3: CaO content of the calcined bed material [wt-%].

Biomass	CaO/bed material ratio
Green Waste	99.09
Green Waste Hydrochar	99.67
OFMSW	99.39
OFMSW Hydrochar	99.51
Out-of-use woods	99.76
Out-of-use woods Hydrochar (treated with water)	99.75
Out-of-use woods Hydrochar (treated with whey)	99.75
Grape Bagasse	99.53
Grape Bagasse Hydrochar	99.61

The SO_2 contamination in the calciner strongly depends on the amount of oxygen recycled via the plasma reactor. If there is not enough oxygen for the formation of $CaSO_4$, extremely high SO_2 concentrations can occur in the gas phase. Figure 4.16 shows the SO_2 and O_2 concentrations above the O_2/C ratio using the example of Green Waste.

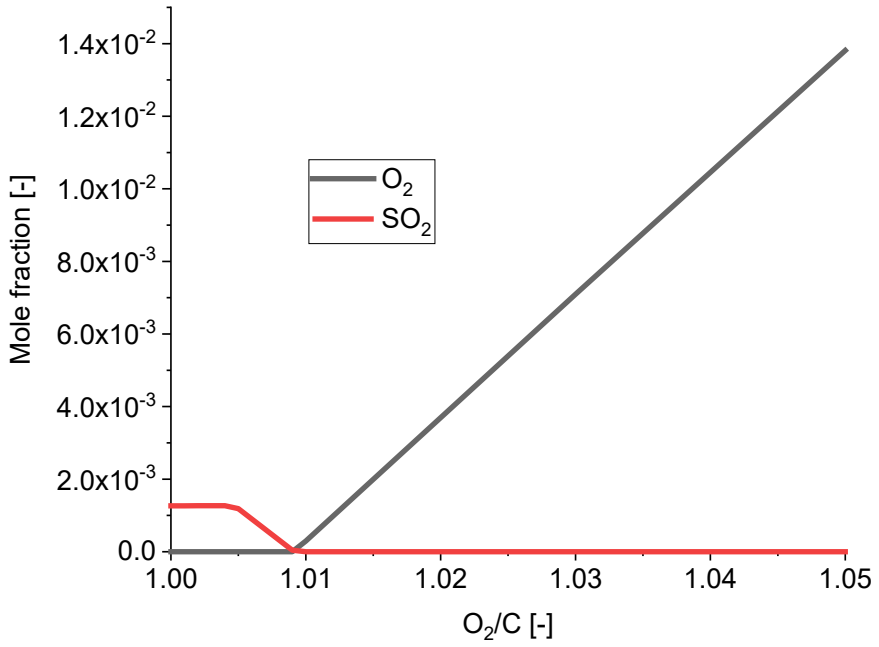

Figure 4.16: Influence of O_2/C on SO_2 at 920 °C, 1 atm (slip ratio = 1/10^5).

Since the H_2S concentration is similar for all gases leaving the gasifier, the bed material of the syngas with the highest CaS content was used for this modeling. Even if C and O_2 were added in the indicated ratio, different (absolute) amounts of C and O_2 were used here, namely the amounts required for an adiabatic increase in temperature from 650 °C to 920 °C (see Chapter 3.2). Since the O_2 mole fraction is linear for $O_2/C > 1.01$, it can be assumed that O_2 does not react with other components of the bed material any longer. Therefore, O_2 dilutes the gas produced during the calcination of the bed material.

Figure 4.17 shows an example (Out-of-use woods Hydrochar treated with whey) of the gas concentration after bed calcination as a function of the slip ratio, i.e. the mass of gas that is transferred to the calciner in relation to the mass of bed material.

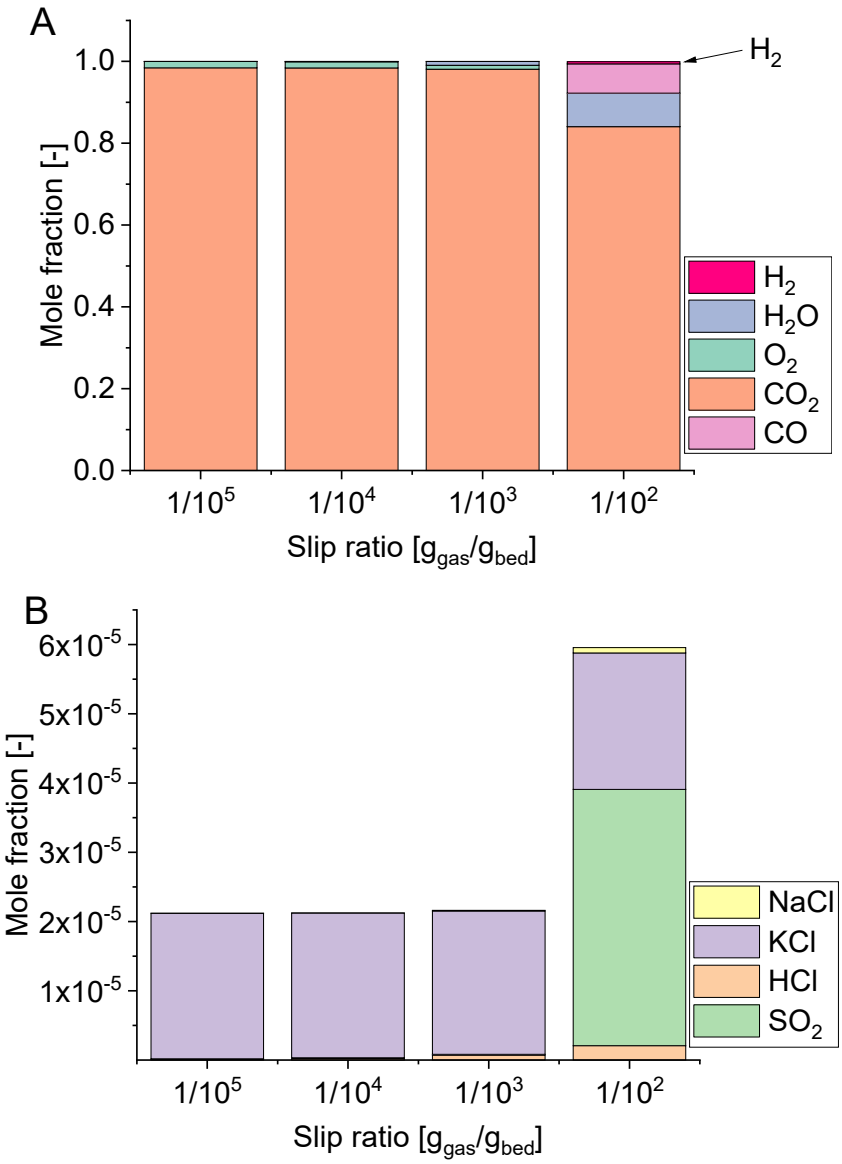

Figure 4.17: Concentration dependence of the main gas components (A) and trace substances (B) on the slip ratio (O_2/C = 1.05).

Only from a slip ratio of $1/10^2$ clear changes in the gas composition can be seen. This statement applies to the main components H_2, CO, H_2O, O_2, and CO_2 as well as to the trace substances NaCl, KCl, HCl, and SO_2. A decent slip is important to ensure enough H_2O for the alkali cleaning unit. However, impurities can also enter the calciner through condensed solids in the bed material stream.

Figure 4.18 shows the condensation behavior of chlorides and sulfates after leaving the calciner. OFMSW Hydrochar and Out-of-use woods Hydrochar (treated with whey) have the highest proportion of condensed chlorides with regard to the biomass used for gasification. This is consistent with Figure 4.20, which shows that the gases from these two

biomasses contain the highest proportion of NaCl and KCl. The proportion of condensed sulfates (mainly Na_2SO_4 and K_2SO_4) is three orders of magnitude lower than that of chlorides. As the primary sorption material CaO has already removed parts of the gaseous H_2S from the gas phase during gasification, this was to be expected.

Figure 4.19 and Figure 4.20 show the gas compositions of the gas streams leaving the calciner. On average, the gas consists of 98.4 % CO_2, 1.4 % O_2, and 0.098 % H_2O. The rest consists of N_2 and trace substances. Since the HCl, NaCl, and KCl concentrations vary extremely strong, they are plotted in logarithmic scales. For OFMSW in Figure 4.18 and Figure 4.19, respectively for Out-of-use woods Hydrochar (treated with whey) in Figure 4.18 B, FactSage could not determine an equilibrium, which is the reason for the missing values.

The maximum HCl contamination is 306 ppm_v (Green Waste), the maximum NaCl contamination is 1870 ppm_v (OFMSW Hydrochar) and the maximum KCl contamination is 1403 ppm_v (Out-of-use woods Hydrochar treated with whey). However, due to the O_2/C ratio of 1.05, the SO_2 concentrations for all biomasses are very low (< 0.2 ppm_v).

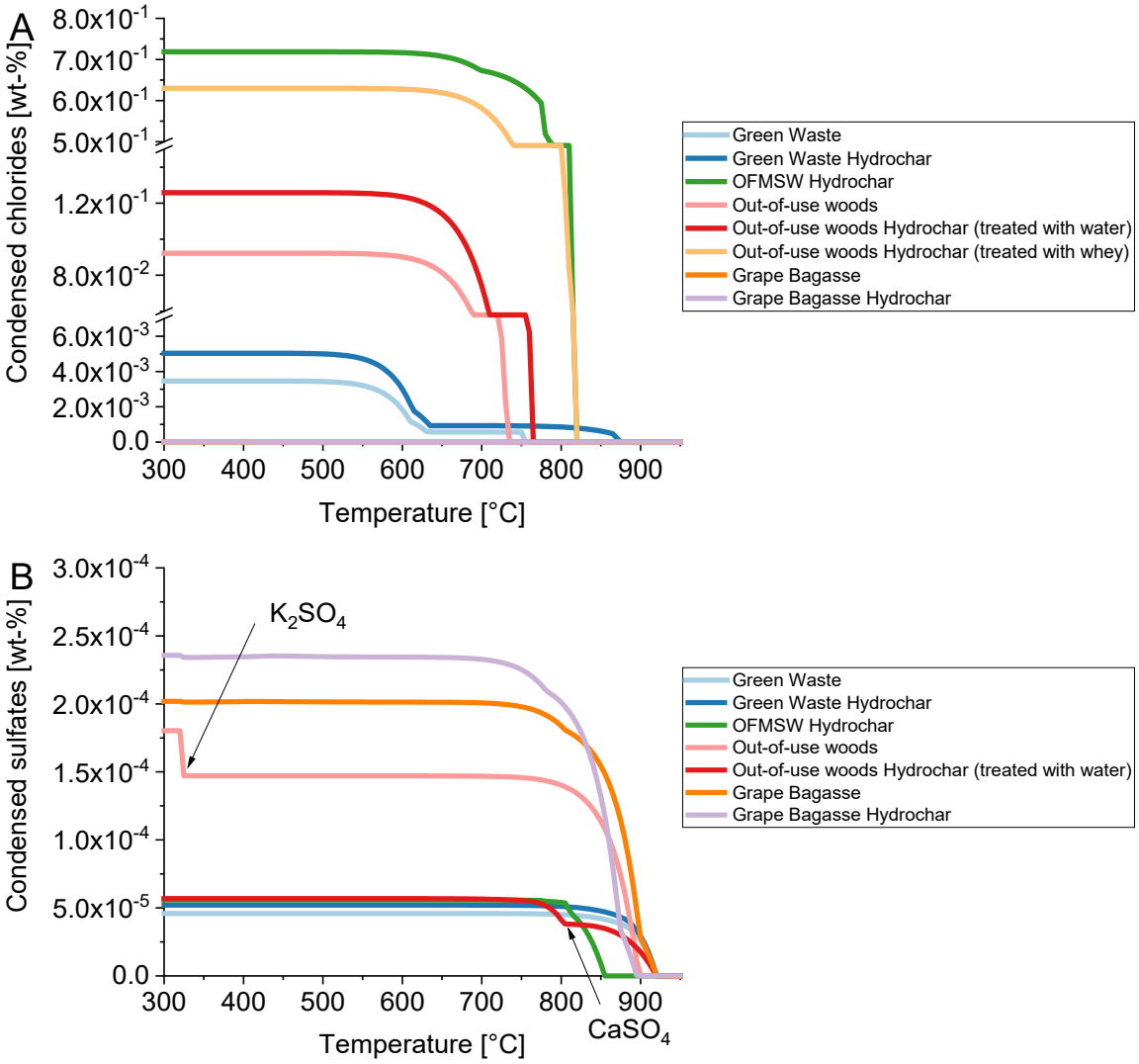

Figure 4.18: Condensation behavior of chlorides (A) and sulfates (B) after leaving the calciner (O_2/C = 1.05, slip ratio = 1/10^5). The concentrations refer to the input biomass.

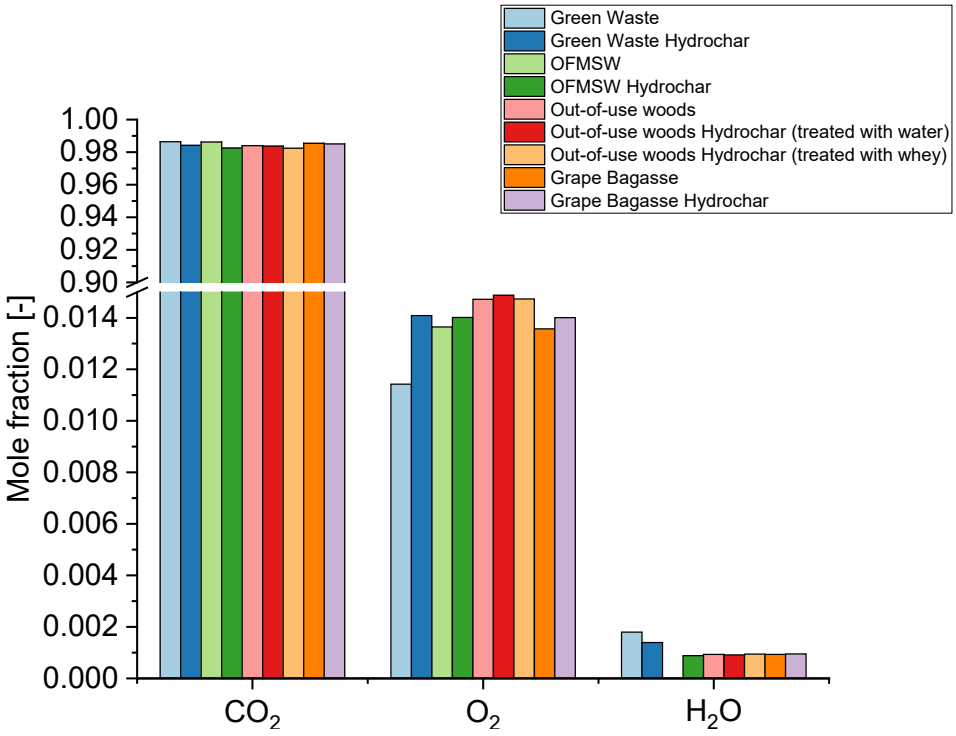

Figure 4.19: Concentration of the main gas components leaving the calcination unit at 920 °C and 1 atm (O_2/C = 1.05, slip ratio = 1/10^5).

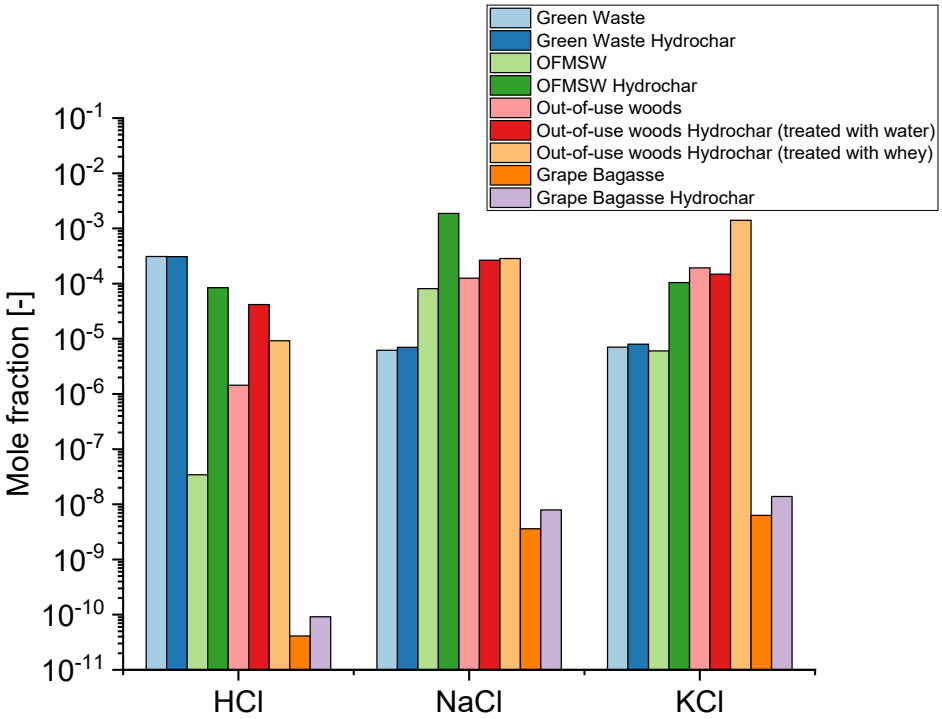

Figure 4.20: Concentration of the trace species of gas leaving the calcination unit at 920 °C and 1 atm (O_2/C = 1.05, slip ratio = 1/10^5).

4.4 Simulation results of HGC calcination side

This chapter deals with the hot gas cleaning of the gas leaving the calciner. First, the influence of alkali cleaning and then the influence of sour gas cleaning on the gas concentrations will be discussed. Aluminosilicates are again used for alkali removal and alkaline earth carbonates for sour gas purification. As in the previous chapters, the condensation behavior after the various cleaning steps is considered here.

4.4.1 Alkali cleaning (calcination side)

The alkali cleaning via aluminosilicates has only a small and indirect influence on the main components CO_2 and O_2 of the syngases. However, since the amount of water in the syngases is limited due to the slip and needed for the alkali cleaning, the water concentration is also shown in Figure 4.21. Compared to Figure 4.19, a decrease in the water concentration according to reaction 2.12 can be seen.

Similar to the alkali cleaning on the gasifier side, a clear increase in the HCl concentrations and a general decrease in the NaCl and KCl concentrations can be seen after the alkali cleaning in Figure 4.22. However, due to the comparatively low H_2O concentrations provided by the slip and the very high HCl concentrations after calcination, the KCl and NaCl concentrations sometimes cannot be lowered by far. The KCl concentrations for Green Waste and Green Waste Hydrochar can be brought from 7 and 8 ppm_v to 1.2 and 1.4 ppm_v, respectively.

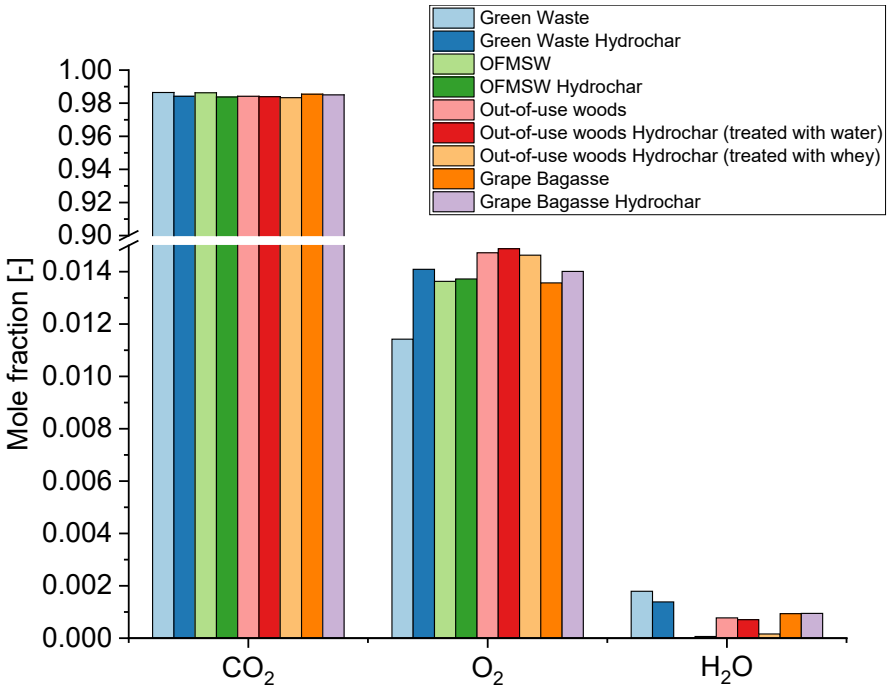

Figure 4.21: Concentration of the main gas species leaving the alkali cleaning unit at 920 °C and 1 atm (O_2/C = 1.05, slip ratio = 1/10^5).

After calcination, the syngas of OFMSW Hydrochar has the highest NaCl content (1870 ppm_v) and, compared to the other syngases, a high HCl content (84 ppm_v). Nevertheless, the NaCl concentration can be lowered to 29.3 ppm_v. The HCl concentration after alkali cleaning increased in this case to 1720 ppm_v. The KCl contamination from the syngas of Out-of-use woods Hydrochar treated with whey can be reduced from 1403 ppm_v to 19.5 ppm_v while the HCl concentration increased to 458 ppm_v.

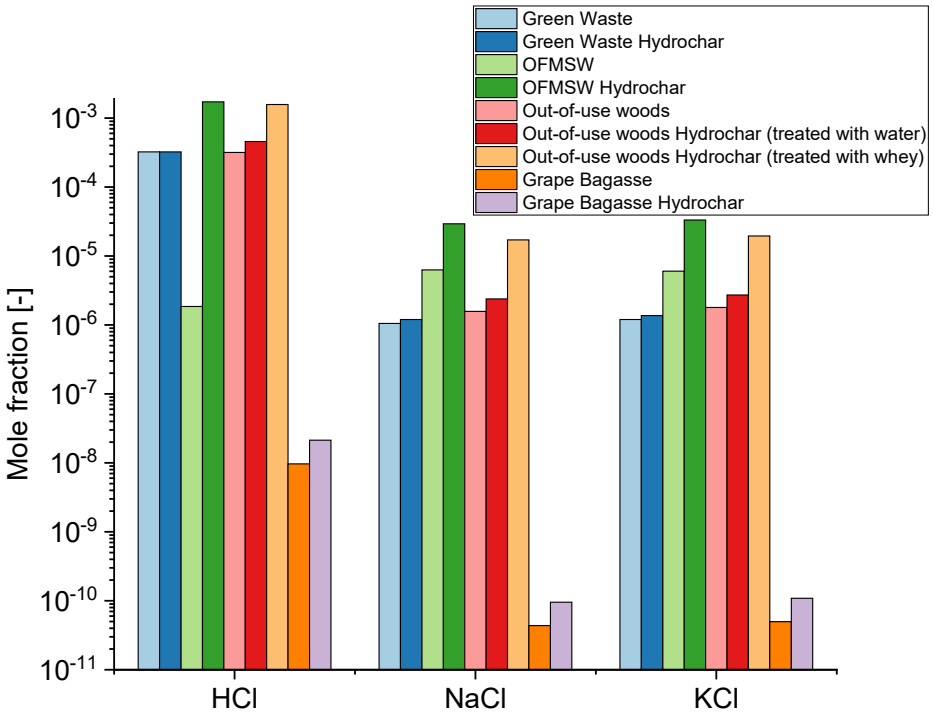

Figure 4.22: Concentration of the inorganic trace compounds of gas leaving the alkali cleaning unit at 920 °C and 1 atm (O_2/C = 1.05, slip ratio = 1/10^5).

Although the NaCl and KCl concentrations of the syngases of Grape Bagasse and Grape Bagasse Hydrochar are already very low, the equilibria can, thanks to the high H_2O to HCl ratio, still be shifted to much lower concentrations. Grape Bagasse and Grape Bagasse Hydrochar reaches NaCl and KCl concentrations of less than 0.1 ppb_v. These concentrations are below the concentrations listed in Table 2.1. It should be noted that these concentrations are below the detection limits of the mass spectrometers used (detection limit: approximately 1 ppb) and are therefore only theoretically achievable values (see Chapter 6.1).

Figure 4.23 shows that the decrease in the NaCl and KCl concentrations after the alkali cleaning on the calcination side shifts the condensation temperatures of the chlorides downwards again.

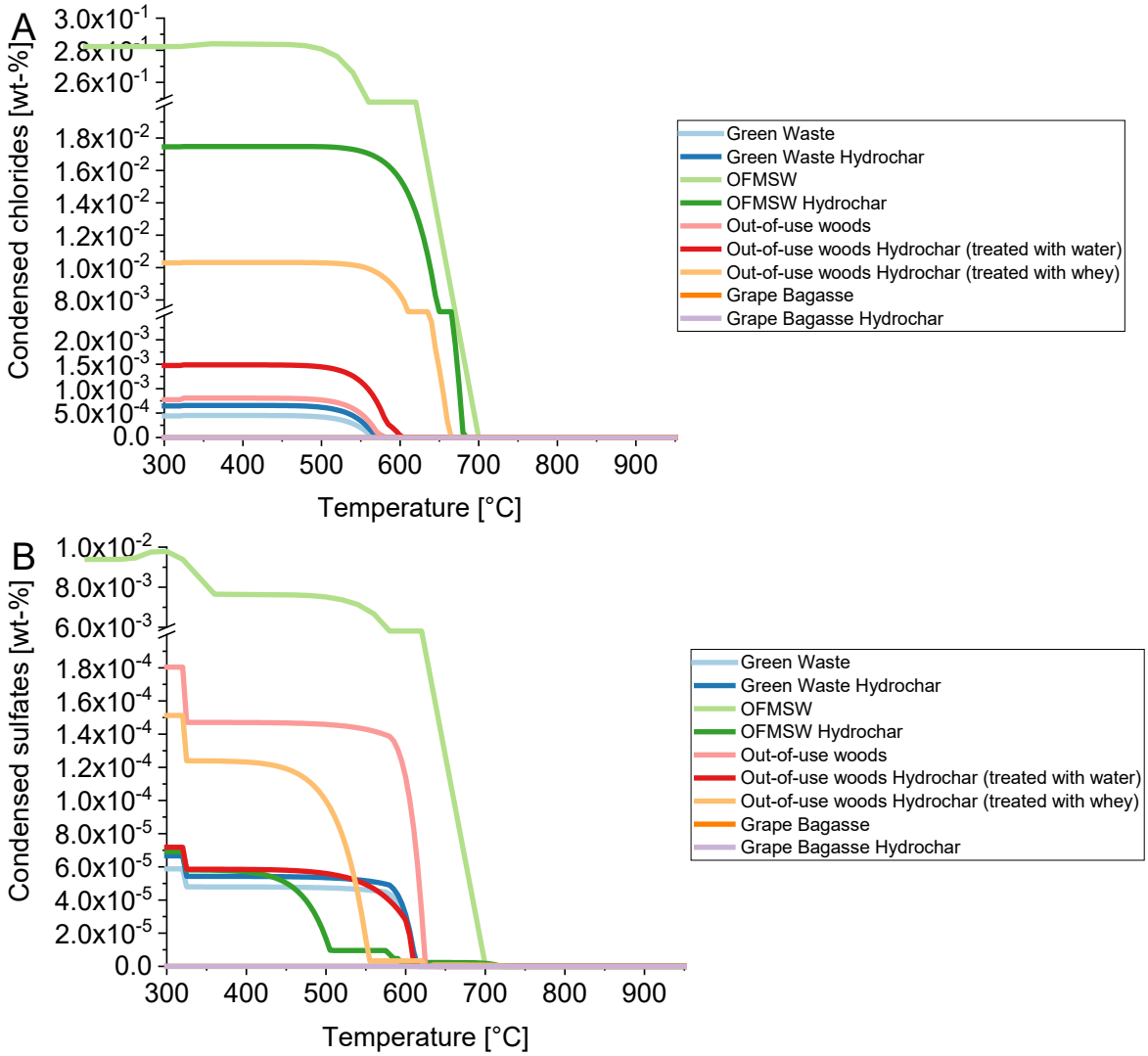

Figure 4.23: Condensation behavior of chlorides (A) and sulfates (B) after alkali sorption on the calcination side (O_2/C = 1.05, slip ratio = 1/10^5). The concentrations refer to the input biomass.

While the chlorides started to condense above 700 °C for all biomasses before the alkali cleaning, the condensation of the chlorides does not start above 700 °C for any of the biomasses after the cleaning.

4.4.2 Sour gas cleaning (calcination side)

As the SO_2 concentrations for all syngases are extremely low, the syngas with the highest HCl concentration (OFMSW Hydrochar: 1720 ppm_v HCl) was chosen for the SO_2-HCl sorption modeling in order to make an estimation for the safe side.

As can be seen in Figure 4.24, the HCl concentration can be lowered for a wide temperature range with $SrCO_3$ and $BaCO_3$.

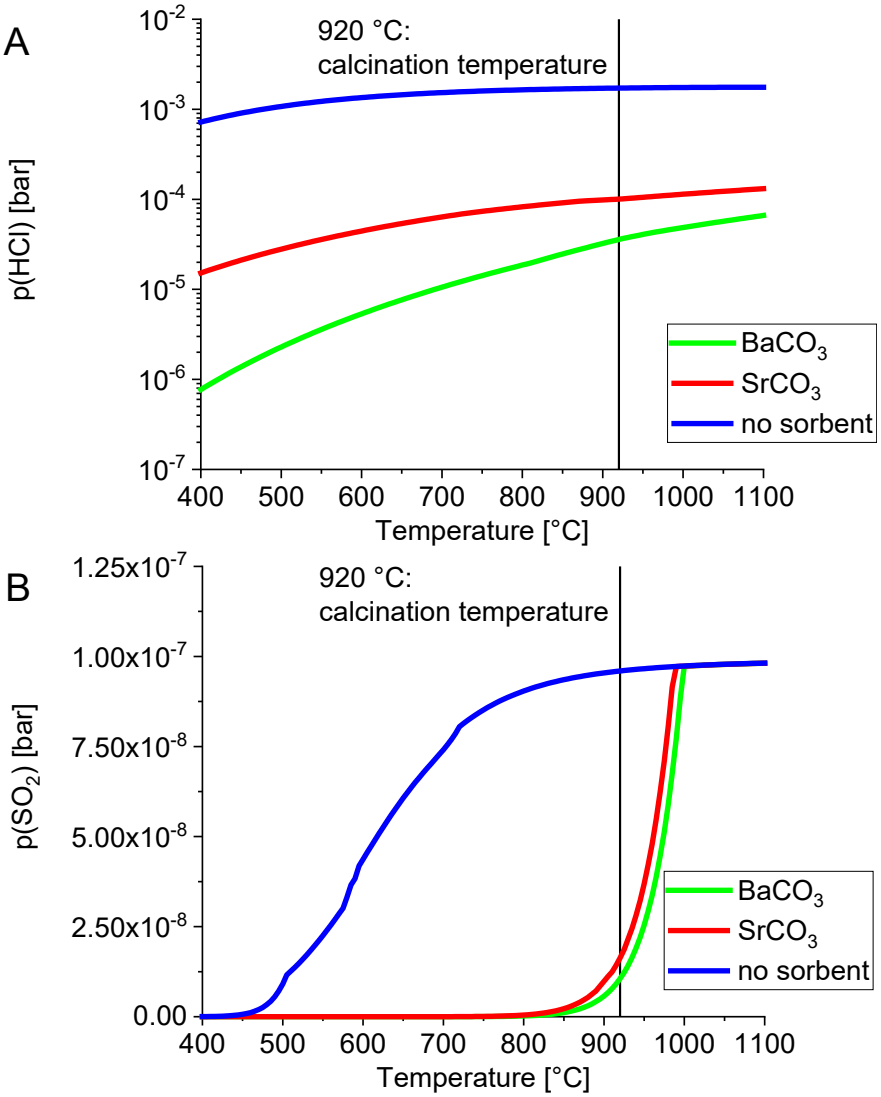

Figure 4.24: Achievable partial pressures of HCl (A) and SO_2 (B) by using $BaCO_3$ and $SrCO_3$ on the calcination side (O_2/C = 1.05, slip ratio = 1/10^5).

At 920 °C (calcination temperature) $SrCO_3$ can lower the concentration from 1720 ppm_v to 100.5 ppm_v, $BaCO_3$ can even lower the concentration to 35.8 ppm_v.

Since CaO is used as the primary sorbent during gasification, CaO might be considered as a secondary sorbent for the HGC on the calcination side. CaO no longer forms carbonates above 825 °C and therefore, can be used in the CO_2-rich atmosphere of the calcination unit. However, the CaO can only reduce the HCl concentration to around 320 ppm_v at 920 °C.

Similar to the gasification side, Figure 4.25 shows the condensation behavior of the syngases after HCl/SO_2 cleaning. Once again, saturation of the gas phase for chlorides and sulfates can be identified at 920 °C. The condensed mass of sulfate is three orders of magnitude smaller than the mass of chlorides.

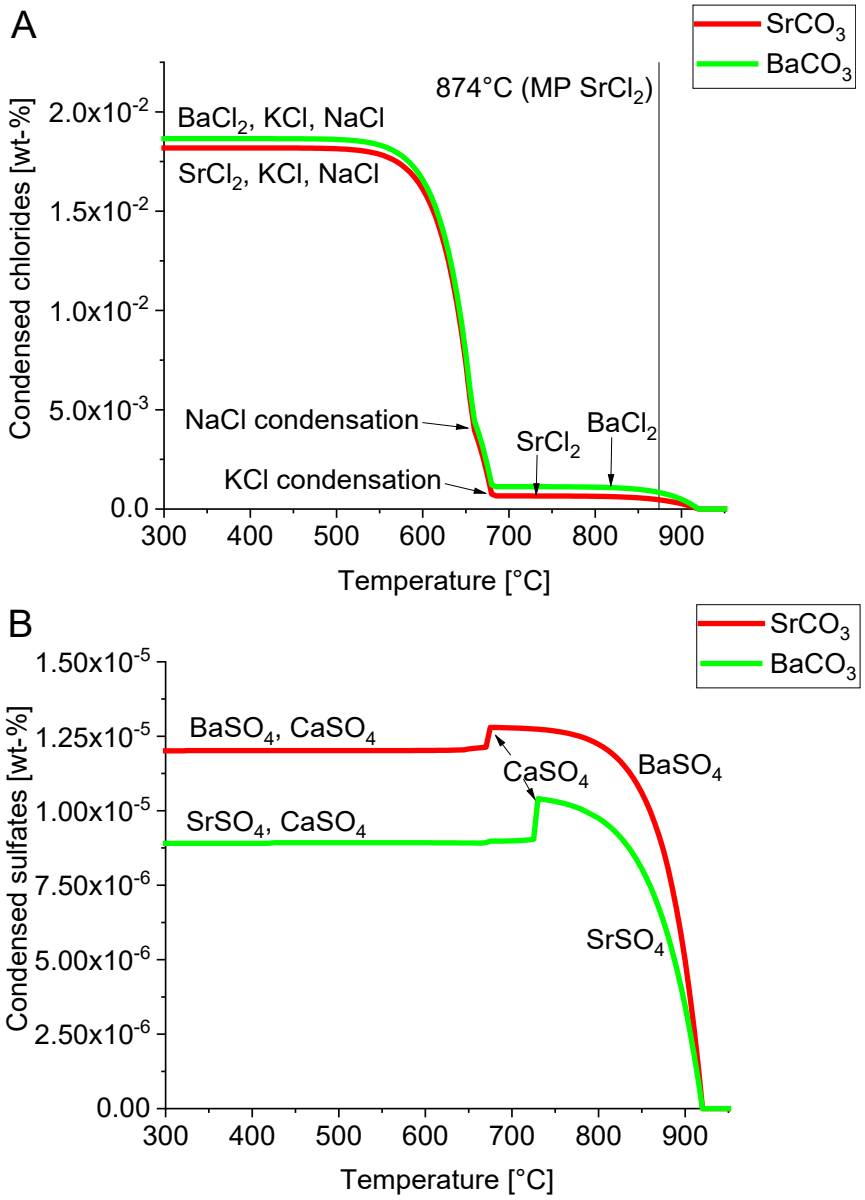

Figure 4.25: Condensation behavior of chlorides (A) and sulfates (B) after HCl/SO_2 cleaning on the calcination side (O_2/C = 1.05, slip ratio = 1/10^5). The concentrations refer to the input biomass.

While the chloride concentration is relatively constant in the temperature range between approximately 700 °C and 920 °C, the sulfate concentration increases by a factor of four in this range. Moreover, between 700 °C and 920 °C only compounds ($BaCl_2$, $SrCl_2$, respectively $BaSO_4$ and $SrSO_4$) associated with the cleaning process condensed. The condensed mass of $BaCl_2$ is slightly higher than that of $SrCl_2$, with $BaSO_4$ and $SrSO_4$ it is reverse.

The condensation temperature of $SrCl_2$ is higher than the melting temperature. Therefore, there is a risk that $SrCl_2$ will melt directly after condensation. The melting point of $BaCl_2$ is at 962 °C so that $BaCl_2$ remains in the solid state.

Figure 4.26 shows the final composition of the purified gas at 920 °C. The sorbents $BaCO_3$ and $SrCO_3$ have no influence on other gas components except HCl and SO_2. The concentrations of the main components in the gases are 98.5 % CO_2, 1.4 % O_2, and 0.09 % H_2O.

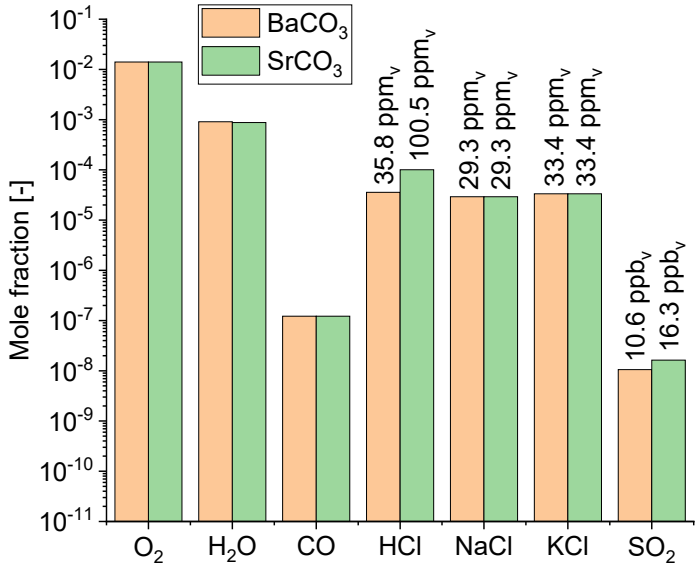

Figure 4.26: Gas composition after HGC (O_2/C = 1.05, slip ratio = 1/10^5).

As described in Chapter 4.2.2, the concentrations of inorganic trace substances to be expected after gasification are within the acceptable range of the SOFC (see Table 2.1). The tolerance limit for inorganic contamination after the calciner is determined by the O_2 membrane-assisted plasma reactor (see Figure 1.1). The development of this reactor is also part of the GICO project. As the impurity limits still have to be determined in the project, no final statements can yet be made about the sufficiency of the HGC concept presented.

4.5 Potentials and risks of the presented HGC concept

Secondary hot gas cleaning (HGC) is a complex process producing different characteristic gas streams after each HGC unit. The calculation results presented can be used not only to determine the expected inorganic trace substance concentrations, but also to identify the main potentials and risks of the GICO process. Statements can be made

about the expected ash quantities and compositions, the ash melting behavior, water requirements for alkali integration as well as temperature stability of certain sorption materials.

Possible potentials include:

- The ash content of the biomasses is extremely variable. By using different biomasses, the ash amount in the gasifier might be regulated (Table 4.1)
- Ce_2O_3, BaO, and SrO shift the equilibrium, through the reduction of CO_2, to extremely high H_2 concentrations (Figure 4.11)
- HCl and H_2S can be lowered with BaO, SrO, and Ce_2O_3 in wide temperature ranges (Figure 4.11)
- The $BaCO_3$, $SrCO_3$ produced in the HGC during H_2S and HCl sorption can be reused as SO_2/HCl sorption material on the calcination side (Figure 4.24)

Possible risks include:

- The ash content of the biomasses is extremely variable. This can lead to an accumulation of non-gasified particles in the reactor (Table 4.1)
- A part of the bed material cannot only be wasted through the formation of CaS or $CaSO_4$, but also through the formation of $CaCl_2$. The formation of $CaCl_2$ is particularly noticeable in biomasses with a high Cl and Si content. $CaCl_2$ can melt under calcination conditions (Table 4.2)
- The ash from different biomasses is present as slag at gasifier temperature (Grape Bagasse+Hydrochar) or there is a risk that slag will be formed with a slight increase in temperature (Out-of-use woods treated with whey) (Figure 4.3)
- The evaporation of Zn during H_2S/HCl cleaning on the gasification side is reflected in the condensation calculations as ZnO, ZnS or $ZnCl_2$ (Figure 4.14)
- Extremely high SO_2 concentrations are possible if not enough O_2 is available for its conversion to $CaSO_4$ (Figure 4.16)
- A certain amount of water in the calciner must be ensured via the slip or by a separate water supply. Otherwise, the integration of the alkalis into the aluminosilicate structure cannot take place (Figure 4.17)

- The slip must not be too large, otherwise the trace substances and product material (H_2) will also be transferred to the calciner (Figure 4.17)

The results presented here are based on thermodynamic equilibrium calculations. Since these do not provide any information about the reaction kinetics and sorption capacities, experimental investigations must be carried out to verify these results.

5 Experimental results

This chapter contains the results of the experiments carried out in this work. As described above, the experimental focus is on the gasifier (release experiments) and on gas treatment after the gasifier (sorption and filter candle exposure experiments), as relatively little research has been carried out into the transition range between the lower temperatures at which standard sorbents are used, and the high temperatures that occur during combustion processes. The results are arranged according to a gasification process. First, the influence of water-leaching and HTC on the inorganic trace substance concentrations of the biomass is discussed, before the main results of the release experiments are presented. After the release experiments, the sorption and exposure results are discussed.

5.1 Release of inorganic constituents from biomass during gasification

The release behavior of inorganics was investigated under gasification-like conditions. In order to understand the influence of different pretreatment methods, a semi-quantitative analysis was performed. The results obtained can be compared semi-quantitatively using bar graphs. However, an absolute statement about the species content cannot be made.

Both pretreated (water-leached biomass, hydrochar, CaO-biomass blends) and the untreated biomasses from Table 5.1 and Table 5.2 were investigated under gasification-like conditions using a MBMS. Thus, the influence of the pretreatment and the influence of CaO on the release behavior can be determined.

The release experiments focused on the species $^{34}H_2S^+$ (m/z = 34), $^{36}HCl^+$ (m/z = 36), $^{58}NaCl^+$ (m/z = 58), $^{64}SO_2^+$ (m/z = 64), and $^{74}KCl^+$ (m/z = 74), as these are of particular importance for hot gas cleaning.

5.1.1 Fuel composition for release experiments

As described in Chapter 2.2.3, the amount of impurities released during gasification can be reduced by pretreatment of the fuel. In the following, the compositions of the fuels for the release experiments under gasification conditions are shown.

Two washing cycles have been performed on the samples. Figure 5.1 shows the chlorine concentration of the filtrate collected during the washing cycles.

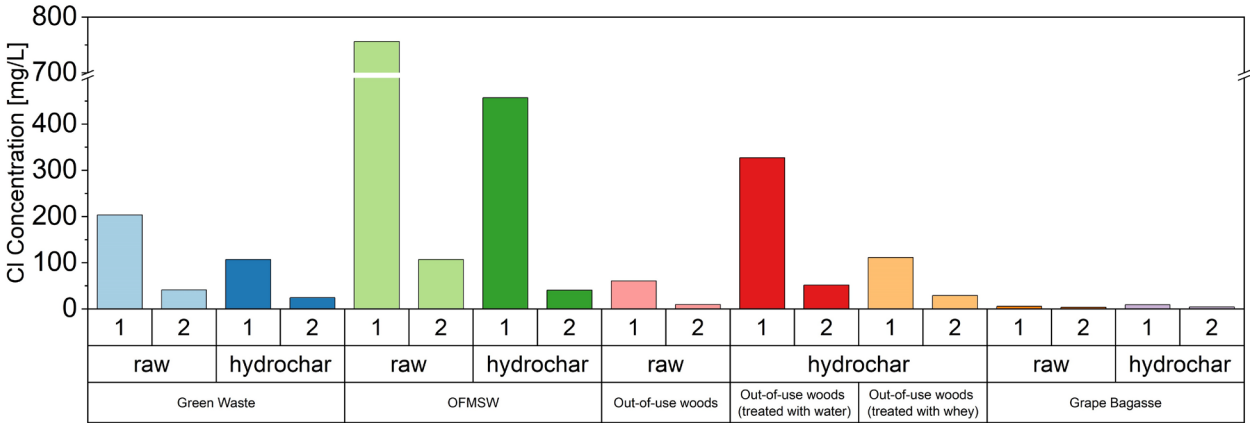

Figure 5.1: Comparison of Cl detected in the washing water after the first and second washing cycle.

Chlorine was detected in the washing water for all biomass samples. The concentration after the first washing cycle was correspondingly higher than after the second washing cycle. Furthermore, Cl was also clearly washed out of the hydrochars (HTC samples), which had previously been exposed to water during preparation.

The results of the ultimate analysis of the untreated feedstocks are listed in Table 5.1 and the results for the water-leached feedstocks are listed in Table 5.2. The effect of water-leaching on the Cl content of the fuels is noticeable. However, no effect is observed on the Si content due to its insolubility. Since potassium is mainly present in the fuel as highly soluble salts such as KCl, water-leaching also reduces the K content.

The biomass content of S, Cl, K, and Na affects the syngas composition. High contents result in higher concentrations of H_2S, respectively SO_2, KCl, NaCl, and HCl. Overall, the analyzed hydrochars (HTC samples) demonstrate a lower content in alkali, alkaline earth, and phosphorus compounds compared to the corresponding raw fuels, likely due to water-leaching during hydrothermal carbonization (HTC). Additionally, the hydrochar also exhibits a 2–22 % higher carbon concentration compared to the raw fuels, highlighting the carbon enrichment that occurs during the hydrothermal carbonization process. On the other hand, the sulfur concentration in the hydrochar has generally remained relatively constant compared to the raw fuels. This suggests that sulfur tends to be retained rather than water-leached during the hydrothermal carbonization process. The only exception is Out-of-use woods. Here, the sulfur concentration after water-leaching was below the detection limit.

Table 5.1: Ultimate analysis of raw fuel samples [wt-%].

Biomass	C	H	N	S	Cl	O	Al	Ca	Fe	K	Mg	Na	P	Si
Green Waste	31.70	4.33	1.25	0.16	0.19	29.40	0.87	1.86	0.76	0.92	0.23	0.08	0.00	9.40
Green Waste Hydrochar	44.20	4.90	0.92	0.10	0.10	32.58	0.59	1.80	0.60	0.48	0.14	0.06	0.00	6.40
OFMSW	38.70	5.31	2.60	0.22	0.76	33.96	0.34	4.30	0.33	0.93	0.51	0.71	0.68	2.81
OFMSW Hydrochar	45.60	5.71	2.35	0.17	0.46	29.78	0.26	4.97	0.22	0.72	0.24	0.45	0.98	1.86
Out-of-use woods	45.50	6.03	1.91	0.09	0.05	43.25	0.04	0.20	0.05	0.07	0.03	0.06	0.00	0.12
Out-of-use woods Hydrochar (water)	49.30	5.52	2.30	0.10	0.11	36.24	0.07	0.49	0.15	0.08	0.10	0.27	0.00	0.99
Out-of-use woods Hydrochar (whey)	46.50	5.78	1.37	0.10	0.31	40.75	0.04	0.54	0.18	0.37	0.07	0.27	0.00	0.53
Grape Bagasse	48.10	5.85	2.34	0.18	0.00	37.10	0.03	0.33	0.17	3.88	0.12	0.01	0.31	0.09
Grape Bagasse Hydrochar	56.50	5.98	2.28	0.18	0.01	30.06	0.07	0.37	0.11	2.37	0.07	0.02	0.00	0.12

Table 5.2: Ultimate analysis of water-leached fuel samples [wt-%].

Leached Biomass	C	H	N	S	Cl	O	Al	Ca	Fe	K	Mg	Na	P	Si
Green Waste	35.60	4.46	1.29	0.17	0.01	33.00	0.91	1.93	0.71	0.57	0.25	0.06	0.00	5.49
Green Waste Hydrochar	47.10	5.28	0.92	0.11	0.00	34.38	0.70	1.49	0.55	0.22	0.09	0.02	0.00	2.70
OFMSW	40.80	5.76	2.82	0.23	0.02	32.67	0.77	3.37	0.30	0.19	0.46	0.16	0.58	2.25
OFMSW Hydrochar	47.30	5.72	1.98	0.18	0.01	27.49	0.27	4.27	0.24	0.10	0.15	0.12	1.31	1.47
Out-of-use woods	47.80	6.19	1.94	0.00	0.01	42.71	0.00	0.20	0.04	0.03	0.02	0.04	0.00	0.07
Out-of-use woods Hydrochar (water)	52.70	5.80	2.04	0.00	0.01	36.31	0.04	0.17	0.11	0.00	0.01	0.00	0.00	0.22
Out-of-use woods Hydrochar (whey)	49.80	6.07	1.24	0.00	0.01	40.04	0.04	0.45	0.18	0.03	0.04	0.03	0.00	0.22
Grape Bagasse	52.60	6.55	2.72	0.21	0.00	34.92	0.02	0.34	0.12	1.22	0.02	0.01	0.00	0.08
Grape Bagasse Hydrochar	61.80	6.51	2.23	0.20	0.00	27.09	0.02	0.44	0.06	0.30	0.00	0.04	0.00	0.14

5.1.2 Release behavior of untreated biomasses under gasification-like conditions

Figure 5.2 shows the intensity-time profile of the $^{19}H_2O^+/^{19}OH^+$ signal whose base level was used to normalize various signal areas. A short peak identifying the volatile trace compounds can be seen immediately at the beginning of each measurement. This peak indicates fast reaction kinetics during devolatilization phase. The signal after this peak is at a higher level than the basic signal before the measurement. This might indicate a kinetic inhibition of the complete H_2O release due to the high H_2O content (20 %) in the gas.

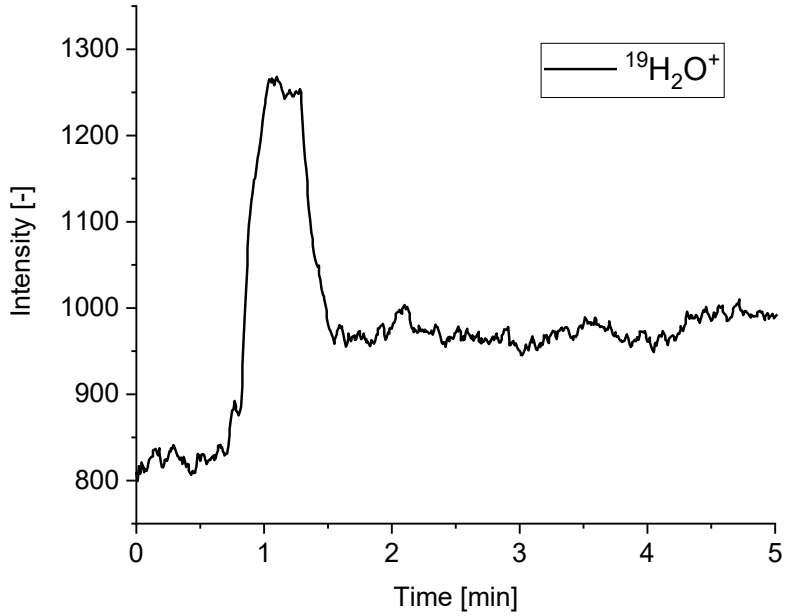

Figure 5.2: Intensity-time profile of $^{19}H_2O^+/^{19}OH^+$ (m/z = 19) of Grape Bagasse at 650 °C in 20 % H_2O and 80 % He ($\dot{V}_{tot}$ = 4 l/min).

Char gasification and ash reactions are characterized by a smaller kinetic rate. Unlike in other investigations [143–145], a second, broader peak cannot be detected or can only be detected to some extent. This is mainly due to the low temperature of 650 °C used in the experiments, where especially many inorganically bound elements released during char gasification have relatively low vapor pressure.

In recent publications [73,136], m/z = 39 was assigned to $^{39}K^+$. To rule out the possibility that fragment 39 belongs to $^{39}NaO^+$ or $^{39}C_3H_3^+$, the intensity-time profiles of potassium-containing species, i.e. $^{39}K^+$ (m/z = 39), $^{55}KO^+/^{55}(H_2O)_3\text{-}H^+$ (m/z = 55), $^{74}KCl^+$ (m/z = 74), and $^{113}K_2Cl^+$ (m/z = 113) from Grape Bagasse, are plotted in Figure 5.3.

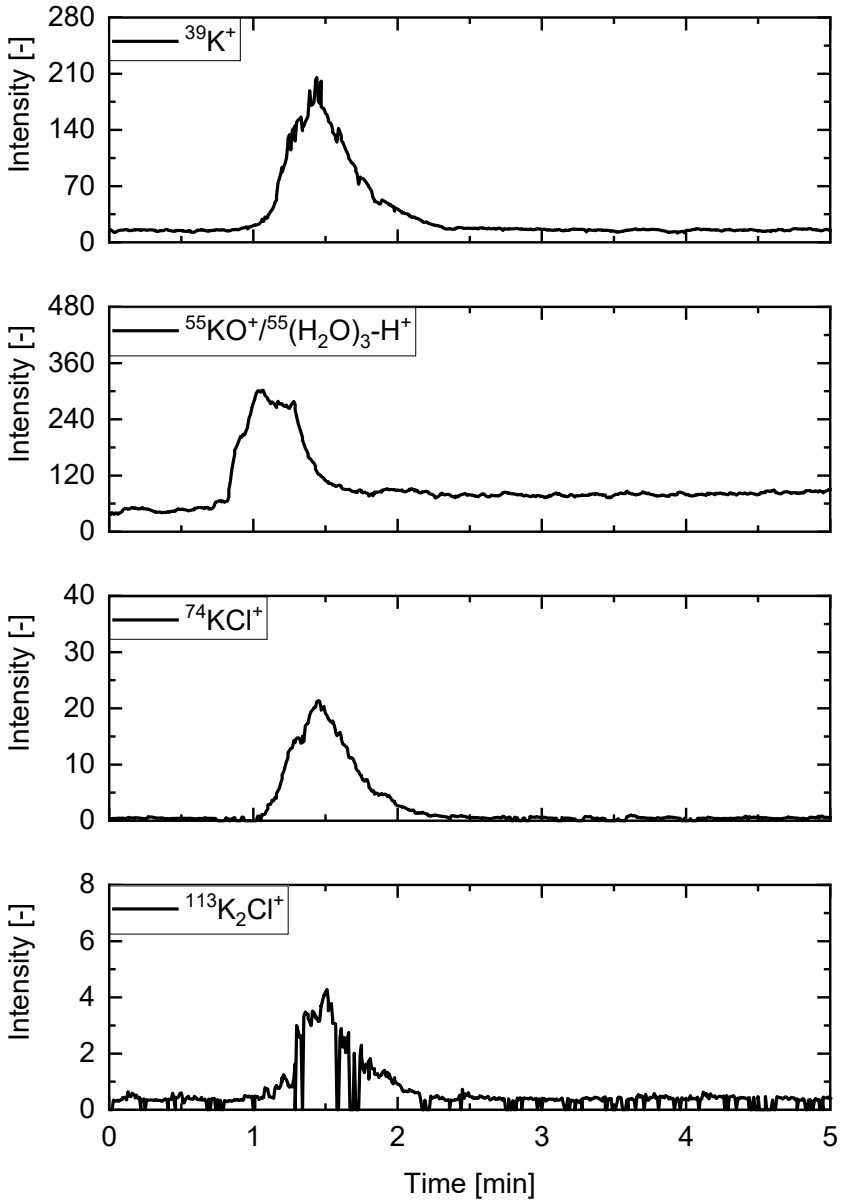

Figure 5.3: Intensity-time profiles of $^{39}K^+$ (m/z = 39), $^{55}KO^+/^{55}(H_2O)_3$-H^+ (m/z = 55), $^{74}KCl^+$ (m/z = 74), and $^{113}KCl^+$ (m/z = 113) of Grape Bagasse at 650 °C in 20 % H_2O and 80 % He ($\dot{V}_{tot}$ = 4 l/min).

As can be clearly seen, the signals of $^{39}K^+$, $^{74}KCl^+$, and $^{113}K_2Cl^+$ are similar in terms of the release duration, release start and the shape of the release peak. However, small amounts of overlap with other species cannot be excluded.

An exception in the figure above is m/z = 55. Preliminary experiments showed that the measurement of $^{56}KOH^+$ (m/z = 56, often fragmented to KO^+ with m/z = 55) can only be done with the inclusion of larger errors due to superposition by a water cluster

($^{55}(H_2O)_3$-H^+) and its isotopes. The release of the component found at m/z = 55 occurs earlier than that of the other potassium-containing components and simultaneously with the water/OH^+ release of signal 19. Therefore, KOH cannot be detected independently.

Figure 5.4 shows an intensity-time profile of $^{58}NaCl^+$. Although the NaCl concentration was only slightly above the detection limit of the ICP-OES (0.01 wt-%), a signal can still be distinguished from the background. Nevertheless, due to the low concentration, there is an increased collapse of the signals.

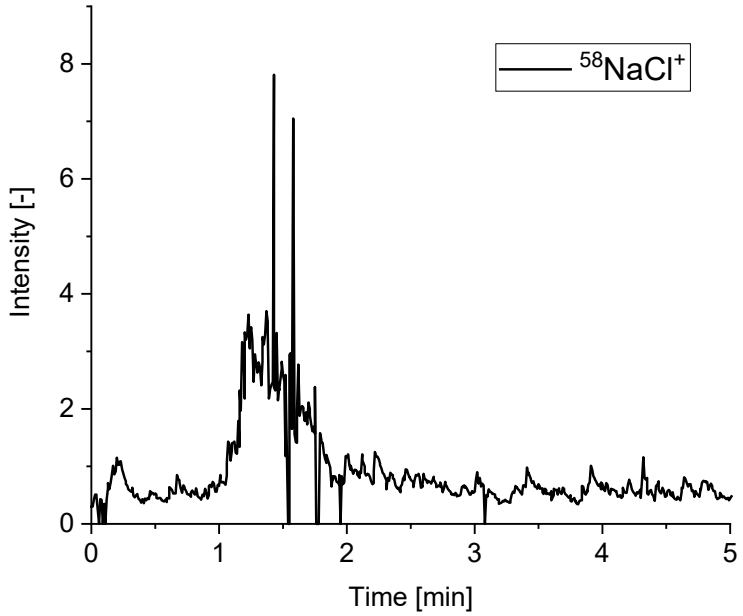

Figure 5.4: Intensity-time profiles of $^{58}NaCl^+$ (m/z = 58) of Grape Bagasse at 650 °C in 20 % H_2O and 80 % He ($\dot{V}_{tot}$ = 4 l/min).

The dip of the signal can partly lead to difficulties in the evaluation, as the integration limits are not clearly identifiable. Grape Bagasse has a $^{39}K^+$ intensity 50 times higher than the example presented for $^{58}NaCl^+$.

Besides KCl and NaCl, another problematic compound in gasification is HCl. Figure 5.5 shows the intensity-time profiles for $^{35}Cl^+$, $^{36}HCl^+$, and $^{38}HCl^+$.

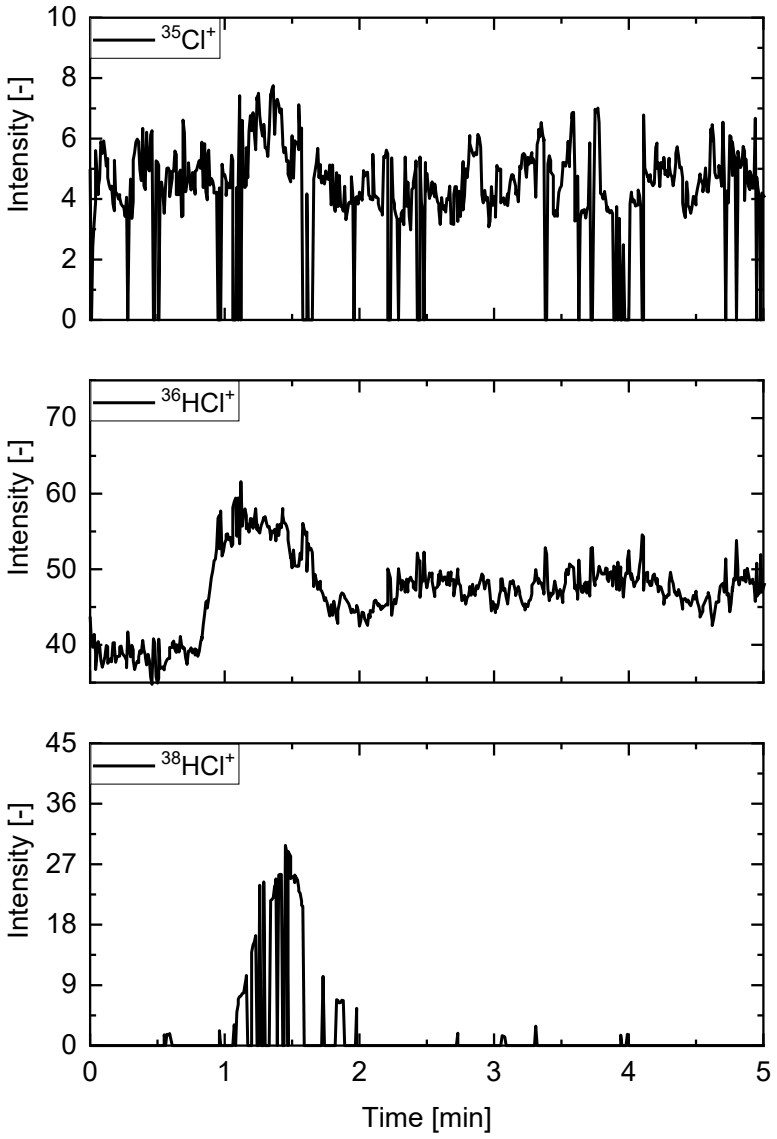

Figure 5.5: Intensity-time profiles of $^{35}Cl^+$ (m/z = 35), $^{36}HCl^+$ (m/z = 36) and $^{38}HCl^+$ (m/z = 38) of Grape Bagasse at 650 °C in 20 % H_2O and 80 % He ($\dot{V}_{tot}$ = 4 l/min).

The levels of the $^{35}Cl^+$ and $^{38}HCl^+$ signals are not sufficient to make an evaluation here. The HCl main signal at m/z = 36 seems to be superimposed by the water cluster at m/z = 37.

Detected sulfur-containing species are $^{34}H_2S^+$, $^{60}COS^+$, and $^{64}SO_2^+$. Typical release profiles are shown in Figure 5.6. Although the experiments were carried out under gasification-like conditions, SO_2 is the sulfur component with the highest concentration. Under gasification conditions, H_2S normally dominates, as there is not enough oxygen for oxidation to SO_2. Reasons for the occurrence of SO_2 are discussed in Chapter 6.1.

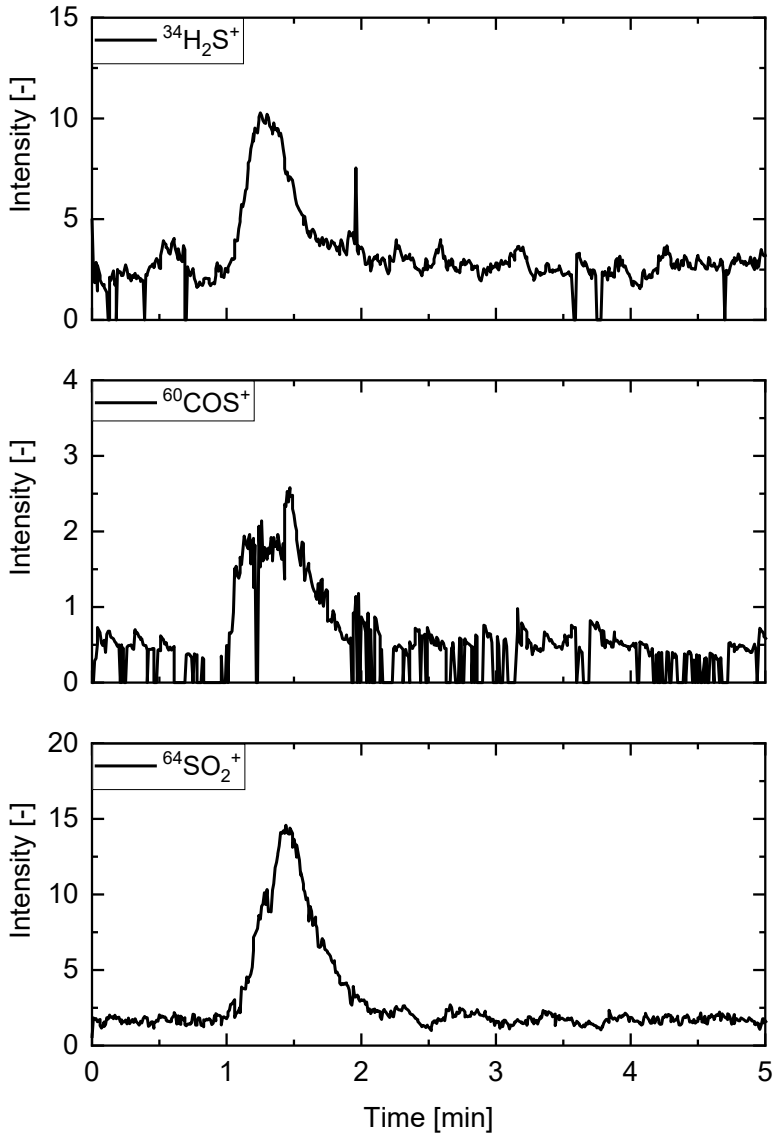

Figure 5.6: Intensity–time profile of $^{34}H_2S^+$, $^{60}COS^+$, $^{64}SO_2^+$ of Grape Bagasse at 650 °C in 20 % H_2O and 80 % He ($\dot{V}_{tot}$ = 4 l/min).

5.1.3 Influence of HTC and water-leaching on the release behavior under gasification-like conditions

The form of the intensity-time profiles of the gas components presented in the previous chapter did not change for the hydrochar (HTC) and water-leached samples. Again, only single peaks and no double peaks/plateaus are recorded for the masses presented. Furthermore, the profiles of the different potassium components are matching in shape and thus verify the release of potassium-containing components.

Figure 5.7, Figure 5.8, and Figure 5.9 show the volatile peak areas of different species released and normalized to the base signal of m/z = 19. Five measurements per sample were performed. Only masses that were significantly above the background noise are evaluated here.

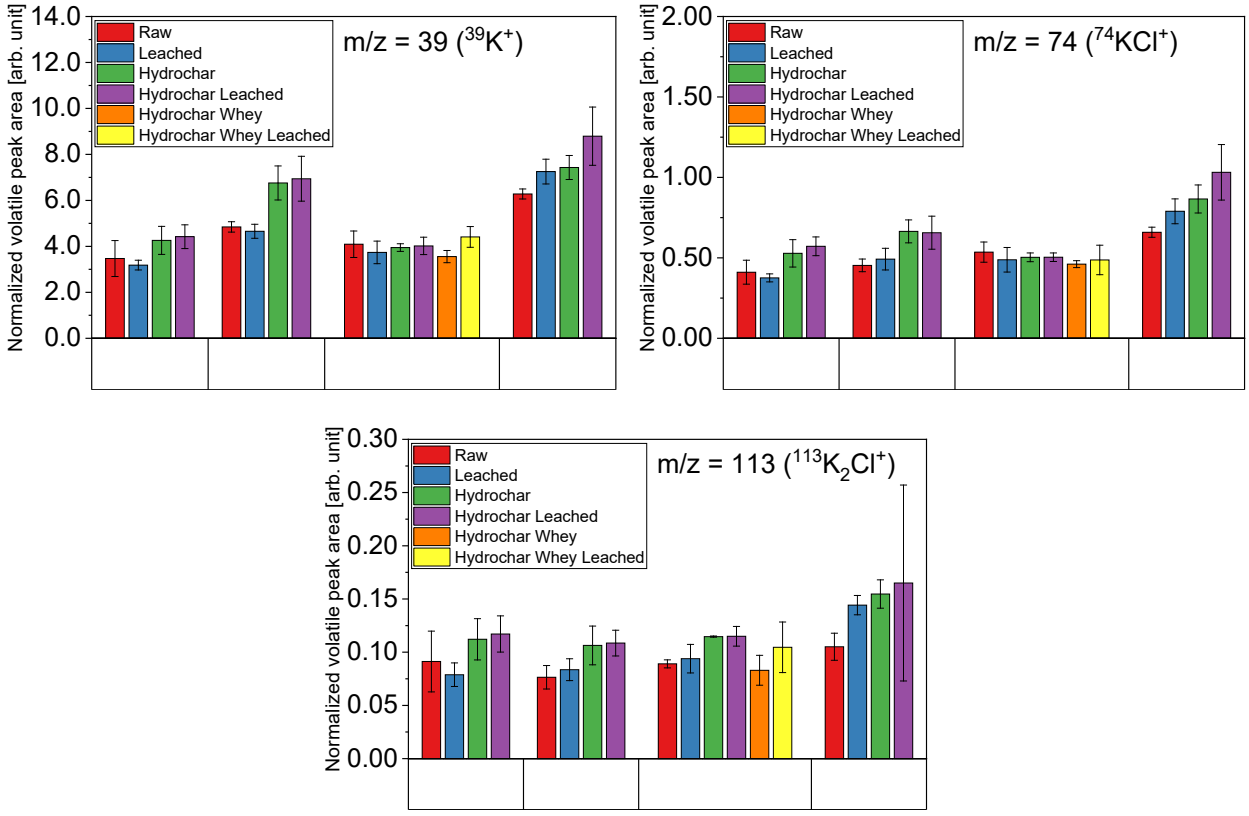

Figure 5.7: Averaged, normalized peak areas of potassium species released during devolatilization phase (n = 5).

In general, the results agree well with the chemical characterization results (see Table 5.1 and Table 5.2), i.e. biomasses with a high potassium or sulfur content (e.g. Grape Bagasse) release more of the associated species (e.g. KCl, H_2S, or SO_2).

The potassium (K^+) peak areas of the biomasses seem to correlate with those of the KCl^+ and K_2Cl^+ peaks. Higher KCl concentrations in the biomasses seem to lead to a proportional increase of the potassium signals. Compared to the untreated biomasses, most of the water-leached biomasses surprisingly show unchanged K^+, KCl^+, and K_2Cl^+ signal intensities despite demonstrably less potassium in the material studied. On the other hand, the hydrochars show a higher release of potassium components even though the potassium concentrations in the hydrochar samples are lower compared to the raw sam-

ples. The potassium components in the hydrochar could be at least partly bound differently than in the non-carbonized biomasses resulting in a higher amount of volatile potassium. This can be attributed to various reactions that take place during HTC (e.g. polymerization, dehydration, hydrolysis, aromatization, etc.) [146,147]. However, a more detailed analysis of the release behavior is beyond the scope of this work.

The sodium concentrations in biomasses shown in Table 5.1 and Table 5.2 are often lower compared to the concentrations of the potassium compounds. For many biomasses, sodium was just above the detection limit of the ICP-OES analysis or was not detectable at all. Accordingly, the peak areas stood out only weakly from the background noise. Figure 5.8 shows the normalized peak areas of $^{58}NaCl^{+}$. These are an order of magnitude smaller than the peak areas of $^{39}K^{+}$.

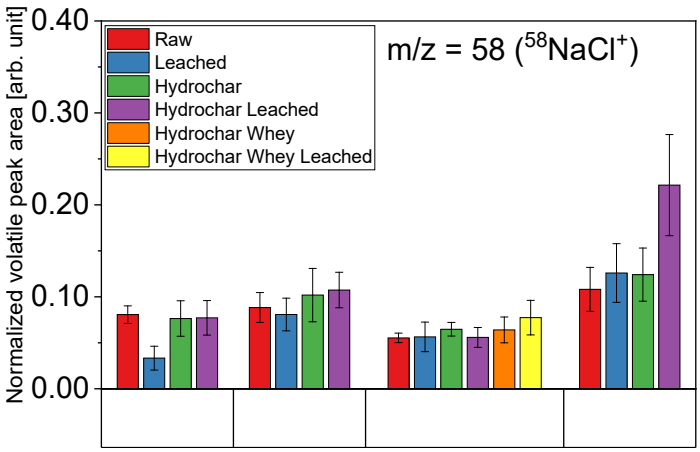

Figure 5.8: Averaged, normalized peak areas of NaCl released during devolatilization phase (n = 5).

Furthermore, with the exception of the Grape Bagasse Hydrochar (water-leached) sample, the values for the normalized volatile peak area are all close to each other. This indicates that the detection limit was reached here.

Unlike the potassium concentrations, the concentrations of the sulfur-containing compounds did not increase for the hydrochar samples (see Figure 5.9). For the Out-of-use woods samples, a H_2S-signal could only be evaluated in one case due to the low sulfur concentrations in the samples.

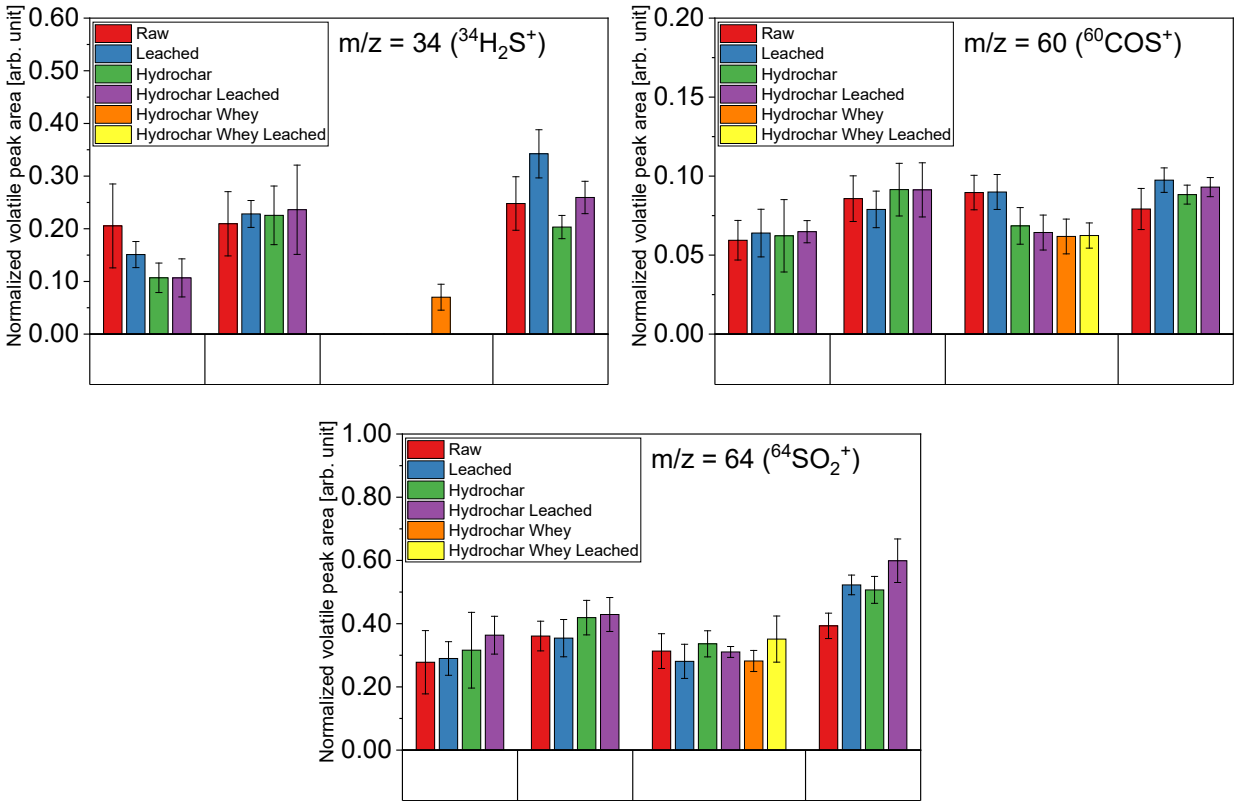

Figure 5.9: Averaged, normalized peak areas of sulfur species released during devolatilization phase (n = 5).

The release of $^{34}H_2S^+$ was the highest for Grape Bagasse samples and the lowest for the Out-of-use woods samples. This fits well with the concentrations in the sample material. Grapes are considered to be extremely sensitive fruits. Conventionally, pesticides, including sulfur, are used to protect the soft skin from weather and fungi infestation [148]. Fruit varieties such as grapes continue to draw attention due to traces of pesticides in samples.

5.1.4 Influence of CaO on the release behavior under gasification-like conditions

To mimic the release behavior of the GICO gasifier, the raw and hydrochar samples were mixed with CaO. The mass of the biomass sample was equal to the mass of the biomass samples from the previous chapter (50 mg). The CaO was added in the same amount (50/50 wt-%). CaO was obtained by calcining $CaCO_3$ at 920 °C for five hours.

Figure 5.10 shows the released potassium components $^{39}K^+$, $^{74}KCl^+$, and $^{113}K_2Cl^+$ of the CaO-mixture samples. The $^{39}K^+$ peak is not as sharp as the corresponding peak of the untreated biomass (see Figure 5.3). Other intensity-time profiles of the same sample indicate a second peak of similar height which overlap and form a broader peak.

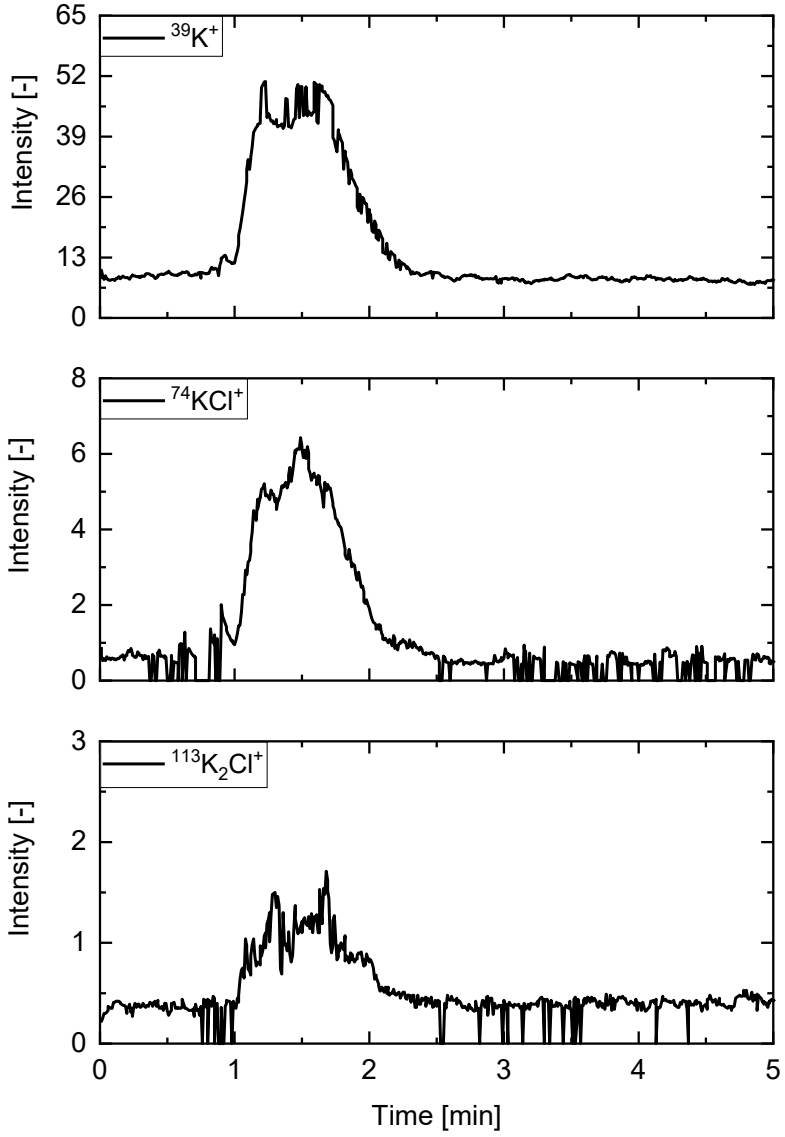

Figure 5.10: Intensity-time profiles of $^{39}K^+$ (m/z = 39), $^{74}KCl^+$ (m/z = 74), and $^{113}KCl^+$ (m/z = 113) of a CaO-Grape Bagasse mixture (50/50 wt-%) at 650 °C in 20 % H_2O and 80 % He ($\dot{V}_{tot}$ = 4 l/min).

Potassium is released into the gas phase in two steps [73]: First, organically bound potassium (e.g. in lignin, cellulose, and hemicellulose) is released at a low-temperature range of up to 500 °C. This stage is insensitive to the chlorine content in the fuel. In the second step, at temperatures above 500 °C, potassium is released at full rate, mostly in the form of KCl and KOH, depending on the chlorine content of the fuel. Since CaO has a direct influence on the concentration of HCl (see reaction 2.13), the release behavior of potassium might also be affected.

Since the experimental parameters of the release experiments samples were maintained (flow rate, gas composition, temperature), the difference in the intensity-time profiles is solely due to the CaO. XRD analyses were performed for all Grape Bagasse samples (untreated,water-leached, mixed with CaO) after the release experiments. For the raw biomass, three potassium-containing phases could be identified (, i.e. $KHCO_3$, $KH_4(CO_3)_3 \cdot 1.5H_2O$, and $K_2Ca(CO_3)_2$), for the CaO mixture only one (, i.e. $K_2Ca(CO_3)_2$).

For the other two potassium-rich samples, Green Waste and OFMSW, a similarly altered peak shape can be detected (see Figure A.2 and Figure A.3).

Figure 5.11 shows the release behavior of the mass 58, which in previous work was mainly due to $^{58}NaCl^+$. Similar to the release of the various potassium components, the formation of a second peak can also be observed here. The addition of CaO seems to promote the release of alkali components.

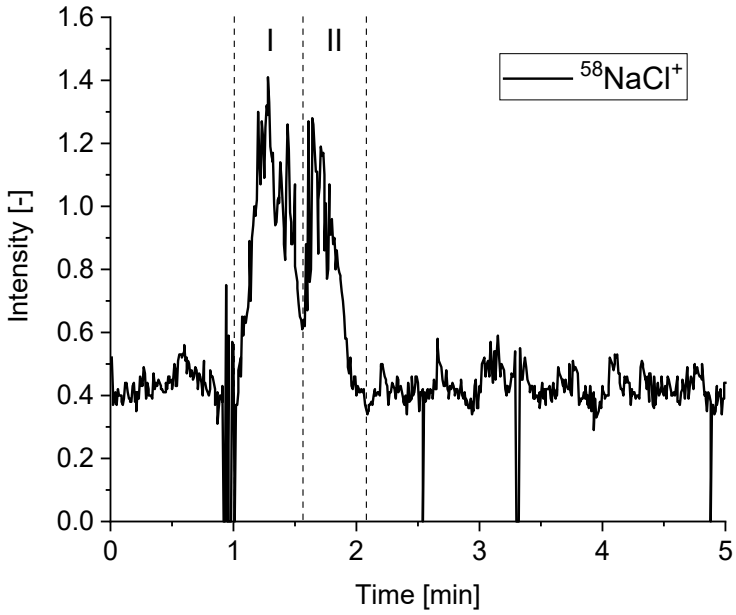

Figure 5.11: Intensity-time profile of $^{58}NaCl^+$ of a CaO-Grape Bagasse mixture (50/50 wt-%) at 650 °C in 20 % H_2O and 80 % He ($\dot{V}_{tot}$ = 4 l/min). I-Devolatilisation phase, II-Char-CaO reactions.

To allow a better comparison between the release behavior of the inorganic trace species of the untreated, water-leached, and HTC biomasses (l.) and the CaO-biomass mixtures (r.), the normalized peak areas of both experiments are placed side by side in Figure 5.12.

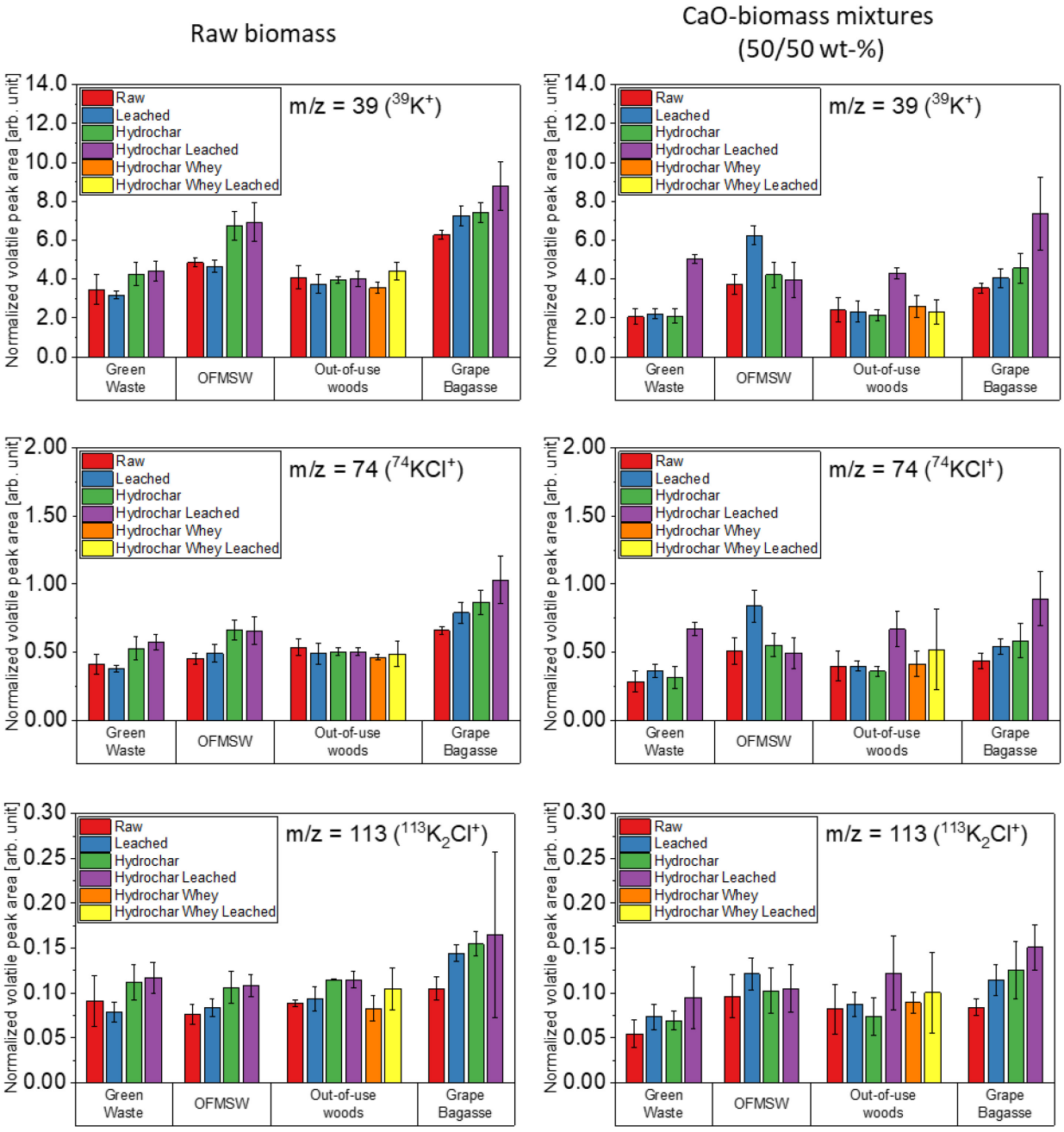

Figure 5.12: Averaged, normalized peak areas of potassium species released from biomass samples (l.) and CaO-biomass mixtures (50/50 wt-%) (r.) during devolatilization phase (n = 5).

It can be seen that the normalized peak areas of the potassium components in the CaO containing experiments are somewhat lower than in the release experiments without CaO. The measured HCl intensities of the CaO-biomass mixtures in the gas are also lower than the intensities measured for the pure biomass samples. CaO may have reacted with HCl to $CaCl_2$, so that the potassium release was inhibited, accordingly.

Similar effects may have occurred during the release of NaCl. Figure 5.13 shows a slight decrease in the peak areas.

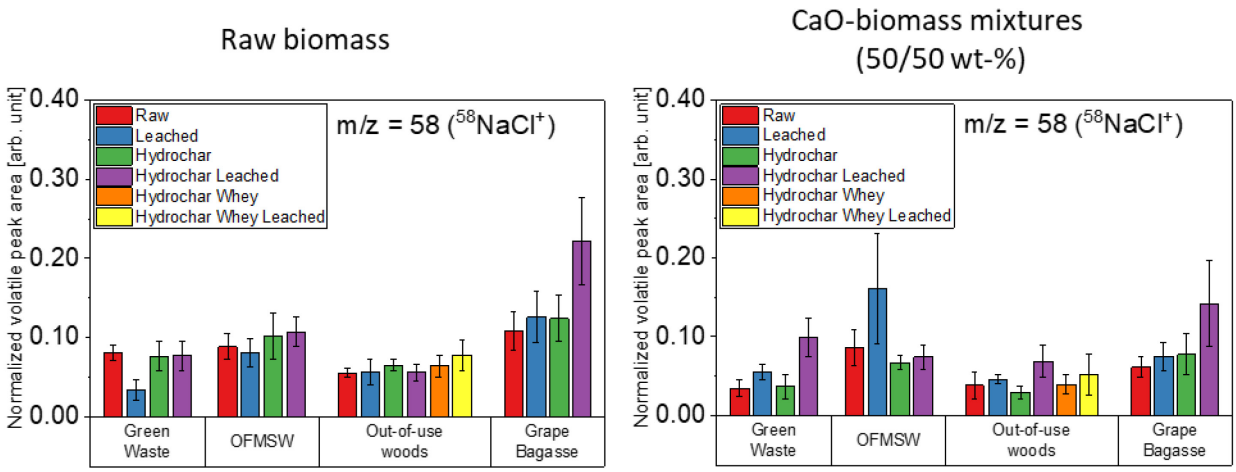

Figure 5.13: Averaged, normalized peak areas of NaCl released from biomass samples (l.) and from CaO-biomass mixtures (50/50 wt-%) (r.) during devolatilization phase (n = 5).

In contrast to water-leaching and HTC, the CaO-biomass mixtures show a clear difference in the concentrations of the detected sulfur species (H_2S, COS, and SO_2). CaO can react directly with both H_2S and SO_2 (see reactions 2.5 and 2.10) lowering their concentration. COS can also be decreased by the reduction of H_2S (see reaction 4.1).

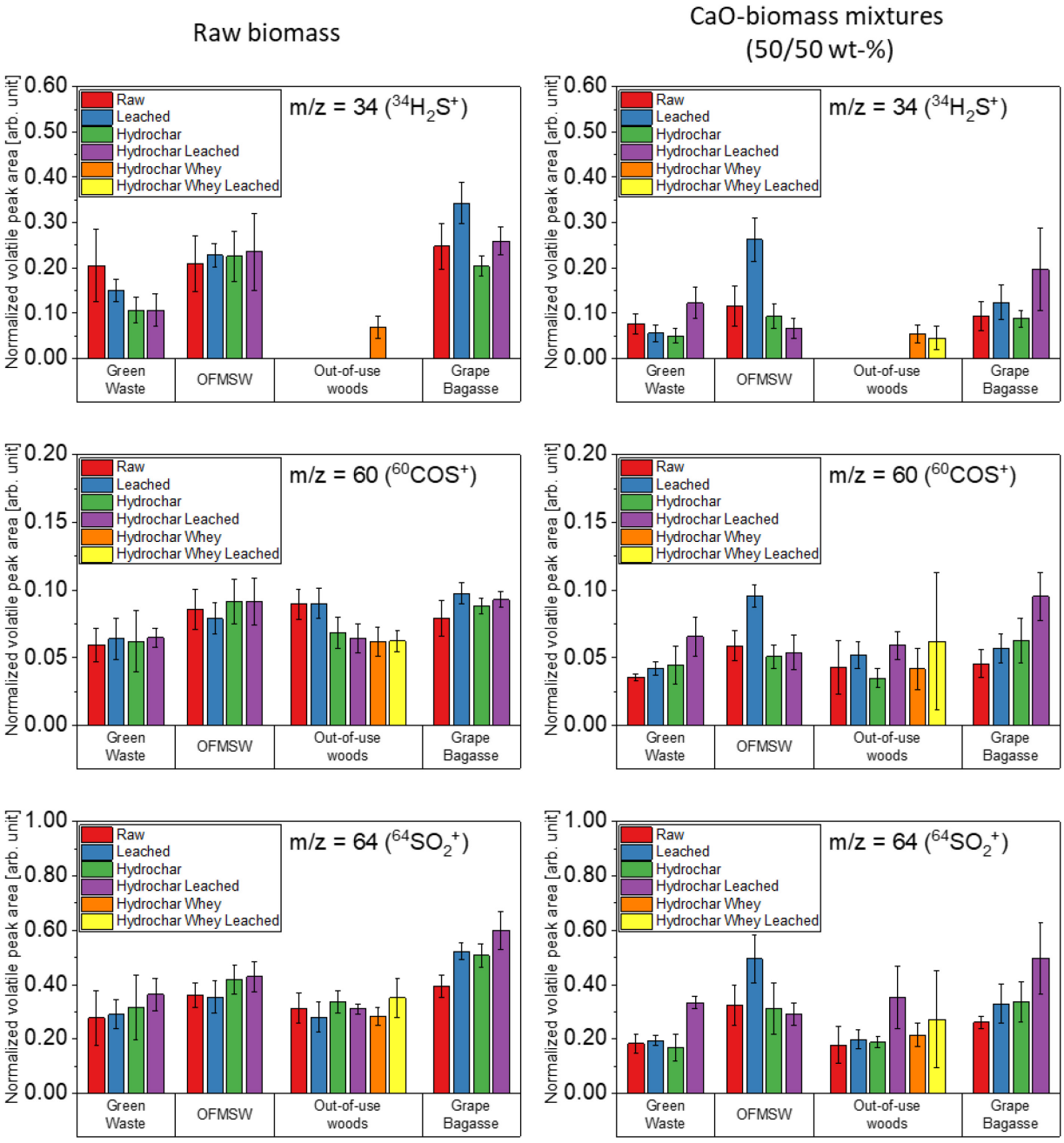

Figure 5.14: Averaged, normalized peak areas of sulfur species released from biomass samples (l.) and CaO-biomass mixtures (50/50 wt-%) (r.) during devolatilization phase (n = 5).

5.1.5 Mineral composition of ashes produced during gasification

Ashes produced during the release experiments were collected and investigated by XRD. The detected mineral phases are listed in Table 5.3.

The amount of KCl present in each sample series varies mainly due to the washing process of the fuel. The silicate phases are not directly affected by washing or thermal treatment. However, washing causes the materials to become denser, which shifts certain inorganic fractions, including SiO_2.

$BaSO_4$ and TiO_2 were detected in the Out-of-use woods samples. Synthetic $BaSO_4$ is used as a component of white pigments for paints. Titanium dioxide pigments are also used in products such as paints and coatings, including glazes, plastics, paper, printing inks, and fibers.

The main phases found in the Grape Bagasse and Grape Bagasse Hydrochar samples are $KHCO_3$, $K_2Ca(CO_3)_2$, $K_4H_2(CO_3)_3 \cdot 1.5H_2O$, $CaCO_3$, and SiO_2. However, these two samples are mostly amorphous (degree of crystallinity < 50 %). A reliable quantification is therefore not possible. By means of Rietveld analysis, only the ratio of the identified crystalline phases can be determined. However, this ratio has little significance because of the incomplete qualitative phase analysis. In addition, there is still the possibility of a misidentification with respect to the phase $K_4H_2(CO_3)_3 \cdot 1.5H_2O$.

Table 5.3: Overview of XRD-detected mineral phases in biomass ashes found to be stable under gasification-like conditions. Rough orientation values are presented: < 10 wt-% (−), 10 wt-% to 30 wt-% (+), 30 wt-% to 50 wt-% (++), and > 50 wt-% (+++).

Biomass	SiO_2	$CaCO_3$	$KAl_4Si_2O_9(OH)_3$	KCl	TiO_2	$Ca_5(PO_4)_3OH$	$BaSO_4$	$CaSO_4$
Green Waste	+++	+	+					
Green Waste	+++	+	+					
Hydrochar								
OFMSW	+	++		-		++		
OFMSW	+	++		-		++		
Hydrochar								
Out-of-use woods	+	++			++		-	+
Out-of-use woods	+++	+			++		+	+
(treated with whey)								
Out-of-use woods	+	+			++		+	+
(treated with water)								

5.2 Fixed bed sorption experiments under reducing conditions

To verify the main results of the modeling calculations made in Chapter 4 and to extend them with information about the reaction kinetics and sorption capacity of different sorbents, H_2S, HCl, and KCl sorption experiments were carried out.

In order to test commercial and new sorbents, tailor-made for GICO's specific needs, a test rig has been set up for sour gas sorption (H_2S+HCl) using different metal oxides in a fixed bed and an industrial mass spectrometer (MS).

Additionally, various aluminosilicates were tested under reducing conditions at 650 °C for KCl removal. To determine the capacities of these materials, a MBMS was used.

5.2.1 KCl sorption at 650 °C under reducing conditions

As described in Chapter 3.4.1, in all investigations for the KCl removal, a KCl-loaded syngas, was passed through a fixed bed. The achievable KCl concentration was determined in situ using a MBMS. Reaction 2.12 shows a dependence on the water content of the KCl concentration in the syngas. The gas mixture used in these experiments (83 % He, 10 % H_2, and 7 % H_2O) is thus a permissible simplification of the GICO syngas.

Figure 5.15 shows the KCl concentration profiles of different sorbents. All tested sorbents reduce the KCl concentration to as low as 0.4 ppm_v and thus, are suitable sorbents. The KCl concentrations when using Kaolin, Bentonite, Montmorillonite, and Clinoptilolite are below the detection limit.

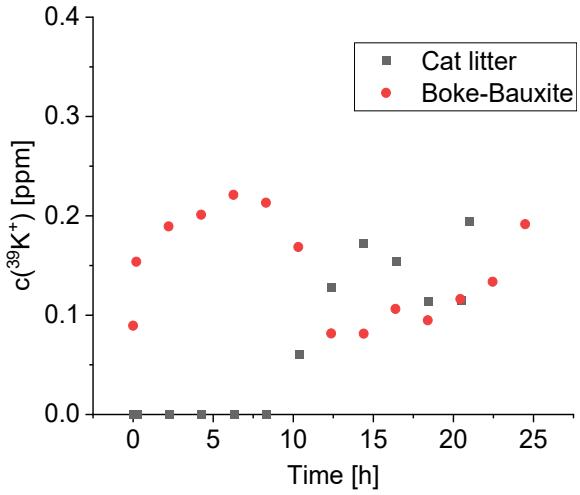

Figure 5.15: KCl concentration after streaming through a sorbent bed at 650 °C (inlet concentration: 83 % He, 10 % H_2, 7 % H_2O, and 25 ppm_v KCl, $\dot{V}_{tot}$ = 4 l/min, 30 g sorbent).

All sorbents were analyzed by XRD after the sorption experiments. An attempt was made to use mainly sorbent pellets that were on the gas inlet side during the experiments. This should increase the chance of detecting alkali-containing structures during XRD. For most sorbents, it is not possible to make a statement which silicate is present or whether an alkali-aluminosilicate has been formed. The strongly asymmetrical diffraction reflections (especially at 20°) indicate stacking faults in the silicate. However, a feldspar phase $(K,Na)AlSi_3O_8$ was detected for Clinoptilolite. However, since this phase was detectable before and after the sorption experiments, the integration of potassium into the alumino-silicate structure could therefore not be proven.

5.2.2 H_2S sorption at 650 °C under reducing conditions

In all investigations on H_2S cleaning, the syngases were passed through a fixed bed (see Chapter 3.4.4). The H_2S signal of the purified gas was recorded by mass spectrometry (MS). Stemmler reported considerable delays in his measurements since the H_2S molecule adsorbed well on surfaces [49]. Therefore, in this work the gas was fed into a separate circuit so that the surfaces of the gas pipes were saturated with H_2S until shortly before the glass reactor. To shorten the saturation time, the H_2S concentration in the gas was increased before opening the sorbent circuit. The experiment was started as soon as there was a steady-state signal.

In order to obtain a rough overview of the sorption behavior of the different sorbents, sorption experiments were carried out at a high flow rate (2 l/min). The most promising sorbents were then tested at a lower flow rate (200 ml/min) and with a longer sorption fill (100 g sorbent).

Figure 5.16 shows the H_2S concentrations during the first 20 minutes of the H_2S sorption experiments for different sorbents. The CO_2 intensity was also recorded.

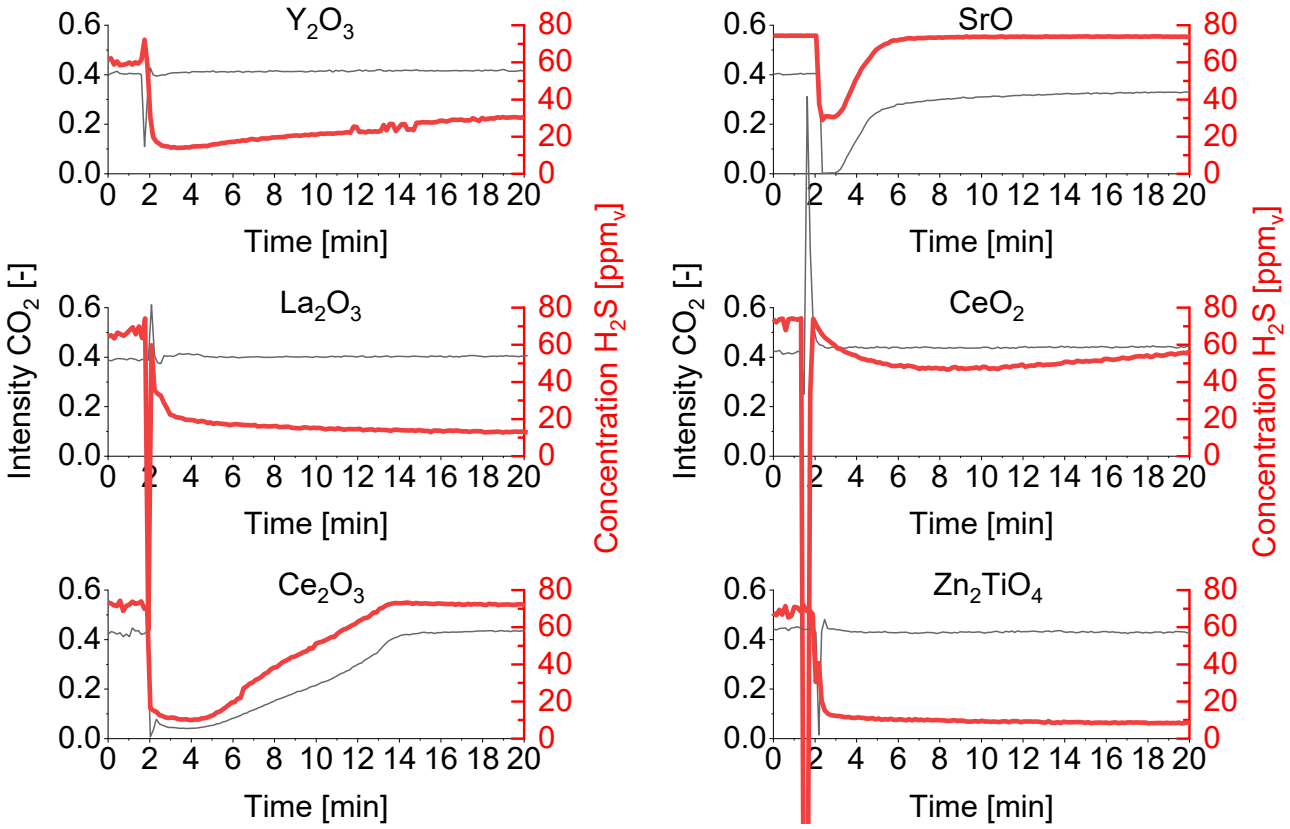

Figure 5.16: Results of the mass spectrometric investigations: CO_2 intensity and H_2S concentrations [ppm_v] of different sorbents (inlet concentration: 73 % H_2, 13 % Ar, 7 % H_2O, 1 % CO_2, 6 % CO (60 ppm_v H_2S), T = 650 °C, $\dot{V}_{tot}$ = 2 l/min, 30 g sorbent).

Although CO_2 leaves the gasifier with a low concentration of around 1 % due to the sorption with CaO (see Chapter 4.1), SrO, and Ce_2O_3 decrease the concentration even a little further. This is in accordance with the calculation results shown in Figure 4.11 in Chapter 4.2. However, a rise in the CO_2 signal can be observed after just a few minutes for these sorption materials. Parallelly, the H_2S concentration increases. Therefore, CO_2 can be seen as a limiting factor in the conducted H_2S-sorption experiments: SrO reacts with CO_2 to form a carbonate while the reduced cerium oxide (Ce_2O_3) oxidizes (CeO_2). Both the oxidation of the Ce_2O_3 and the carbonation of SrO take place quickly, which is the reason that H_2S can only be removed well for a short time.

For Zn_2TiO_4 no decrease of the CO_2 signal can be seen, as $ZnCO_3$ is only stable at temperatures up to approximately 300 °C. Zn_2TiO_4 lowers the H_2S concentration to single-digit ppm_v values for several hours despite a high flow rate. Because La_2O_3 has similar properties compared to Ce_2O_3 (molar mass, electronegativity), which according to the

literature has a good H_2S sorption effect [113,149,150], it was also used in the experiments. Since the 3-valent form of Lanthanum oxide (La_2O_3) and Yttria (Y_2O_3) are stable under gasification conditions, the CO_2 signals remain constant. However, H_2S concentrations for La_2O_3 are as low as for Zn_2TiO_4. Moreover, La_2O_2S was detected after the sorption experiment using XRD.

As the H_2S signal for SrO and Ce_2O_3 did not reach a plateau during sorption, it can be assumed that the gas has not yet reached its achievable purity. In order to give a better estimate of the sorption capacity, experiments were carried out with a reduced volume flow rate and a longer sorbent bed (100 g).

Furthermore, a stabilizing effect of CaO on SrO against carbonation was investigated by testing mixtures of 10 mole-% CaO, 90 mole-% SrO (10Ca90Sr), and 90 mole-% CaO, 10 mole-% SrO (90Ca10Sr). In addition, a 10 mole-% BaO, 90 mole-% CaO (90Ca10Ba) mixture was tested because it has achieved good results in Stemmler's work [49].

Figure 5.17 shows the H_2S concentration when cerium oxide (Ce_2O_3) is used. H_2S concentrations of less than 1 ppm_v can be achieved for more than 6 hours. After saturation, an extreme increase in the H_2S concentration (approximately 170 ppm_v) can be seen for a short time, which slowly decreases. This is due to the fact that H_2S is released again. The oxidized form (CeO_2) is more stable than the sulfides formed (Ce_2O_2S, Ce_2S_3).

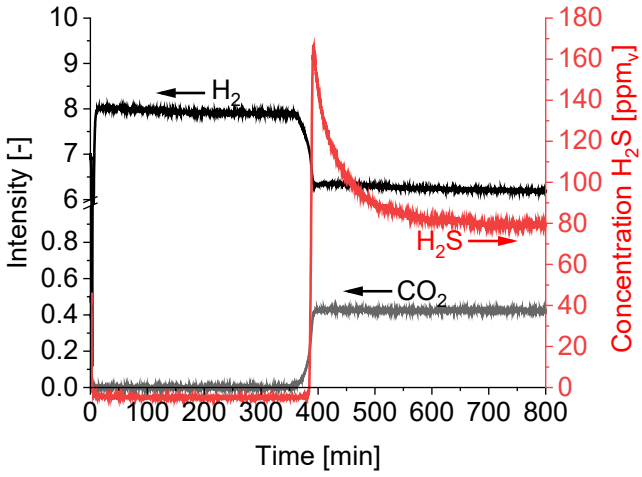

Figure 5.17: Results of the mass spectrometric investigations: CO_2 intensity and H_2S concentrations [ppm_v] of Ce_2O_3 (inlet concentration: 73 % H_2, 13 % Ar, 7 % H_2O, 1 % CO_2, 6 % CO (60 ppm_v H_2S), T = 650 °C, $\dot{V}_{tot}$ = 0,2 l/min, 100 g sorbent).

The XRD analysis of the sorption material after the sorption experiment show a single CeO_2 phase. No more sulfides or reduced cerium oxides could be detected.

The sorption with the BaO-sorbent (10Ba90Ca) also shows an increase in the H_2S concentration above the initial concentration of 60 ppm_v after deactivation of the sorption material (Figure 5.18). The sorbent is also able to keep the H_2S concentration below 1 ppm_v for approximately 3 h.

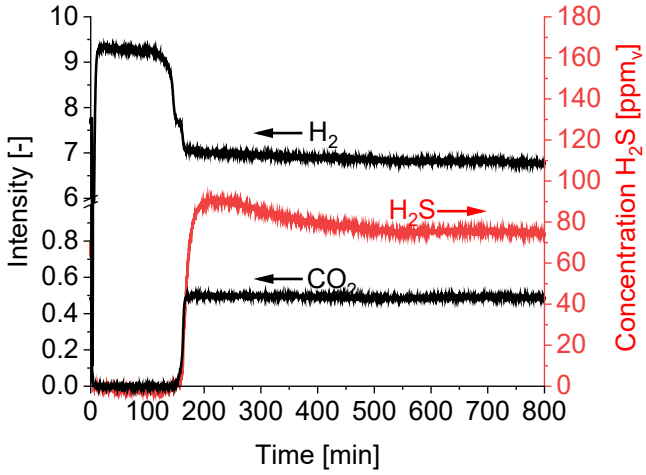

Figure 5.18: Results of the mass spectrometric investigations: CO_2 intensity and H_2S concentrations [ppm_v] of 10Ba90Ca (inlet concentration: 73 % H_2, 13 % Ar, 7 % H_2O, 1 % CO_2, 6 % CO (60 ppm_v H_2S), T = 650 °C, $\dot{V}_{tot}$ = 0,2 l/ min, 100 g sorbent).

Again, no sulfide can be detected due to the release of H_2S after sorption. However, the XRD analysis of the sorption material shows that the formation of $CaCO_3$ was suppressed and that only $BaCO_3$ and CaO (Lime) are present (see Figure 5.19). One assumption of the calculations in Chapter 4 was that the CO_2 concentration cannot be further reduced with CaO. BaO has reduced the CO_2 concentration even below 1 %. Since the gas composition is based on the calculation results at the gasification outlet, the modeling and experimental results are consistent with each other.

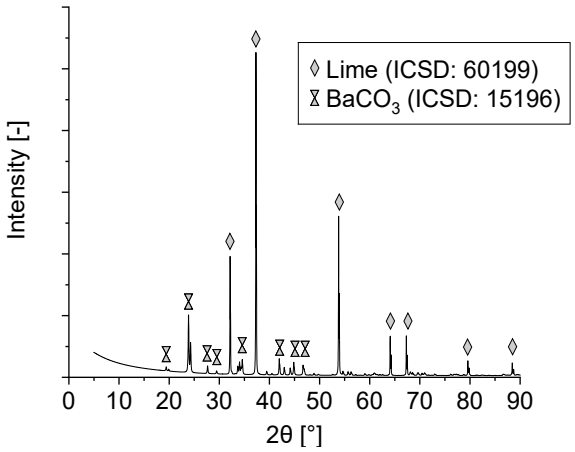

Figure 5.19: XRD spectrum of 10Ba90Ca after sorption experiment.

To gain a better understanding of the deactivation behavior of 10Ba90Ca over time, the sorption experiment was stopped after 50, 100, 150, and 600 minutes. At these times, the syngas was replaced by argon. After the furnace had cooled down, the fixed bed was divided into ten fractions of equal size. The samples were placed in the glovebox until elemental analysis.

Figure 5.20 shows the evaluation of the elemental analysis performed by ZEA 3 of Forschungszentrum Jülich. Sample position 1 refers to samples taken at the gas inlet side, while sample position 10 are samples taken at the gas outlet side.

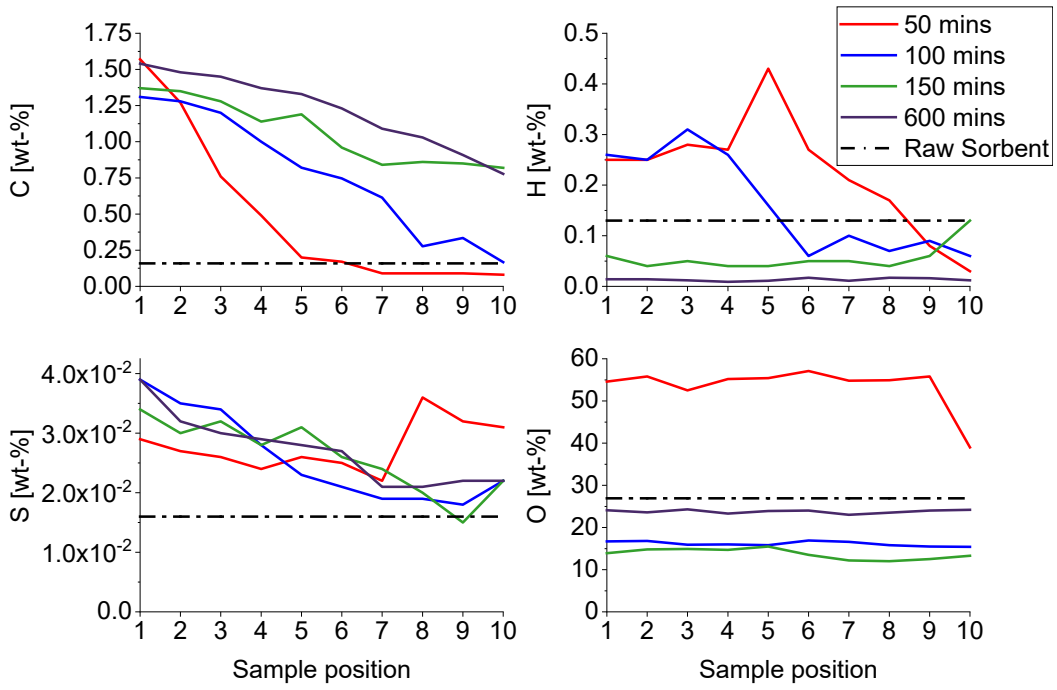

Figure 5.20: Elemental analysis of 10Ba90Ca after 50, 100, 150, and 600 minutes of sorption time.

It can clearly be seen that the C concentrations increase with increasing residence time in the reactor. Furthermore, higher C concentrations are observed at the reactor inlet. Both the determination of the components of the sorbent and the C-analysis of an unloaded reference sample show that hardly any carbonates are present after sorbent production.

Since only gases such as CO_2 and CO are present as carbon sources, the increase in C concentration is due to the formation of $BaCO_3$ ($CaCO_3$ is not formed under these conditions). The higher C concentrations at the reactor inlet (sample position 1) compared to the reactor outlet (sample position 10) are due to the higher CO_2 concentrations at the reactor inlet. Lower amounts of CO_2 arrive at the back of the reactor with a time delay. After 50 minutes, approximately 50 % of the sorption material has reacted to $BaCO_3$.

For the sulfur concentration, there is also a corresponding drop in concentration along the bed. Only after 50 minutes an increase of the sulfur concentration for the samples that were located close to the gas outlet (sample positions 8-10) can be observed. Since the sulfur concentration at positions 8-10 has decreased over time while the C concentration has increased, it is reasonable to assume that the carbonates are more stable than the sulfur compounds and that the sulfur components (BaS) are driven further to the gas outlet. However, the leaching of the sulfur components does not occur completely.

Figure 5.21 shows the H_2S sorption process when using SrO. The 1 ppm_v H_2S target cannot be achieved here. In contrast to Ce_2O_3 and the Ba-based sorption material, there is no extreme increase in the H_2S concentration after deactivation by the CO_2.

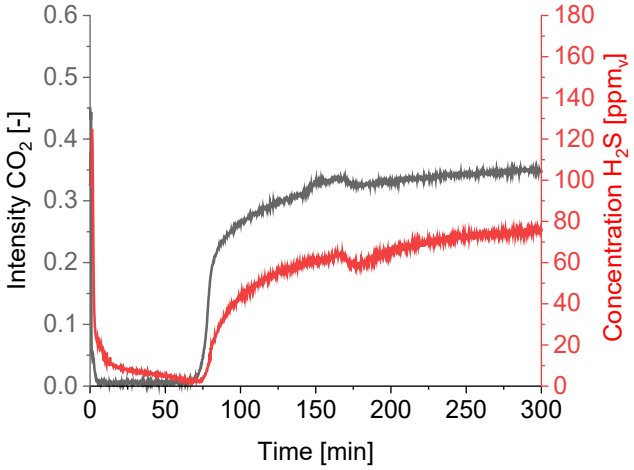

Figure 5.21: Results of the mass spectrometric investigations: CO_2 intensity and H_2S concentrations [ppm_v] of SrO (inlet concentration: 73 % H_2, 13 % Ar, 7 % H_2O, 1 % CO_2, 6 % CO (60 ppm_v H_2S), T = 650 °C, $\dot{V}_{tot}$ = 0,2 l/min, 100 g sorbent).

Figure 5.22 shows that $SrCO_3$ has been formed. Nevertheless, SrO can still be detected in the sample by XRD. Possibly only an external $SrCO_3$ layer has been formed. The inner part of the sorbent could still consist of SrO after the sorption experiment since the SrO sorbent has a small specific surface (0.209 m^2/g, see Table 3.9).

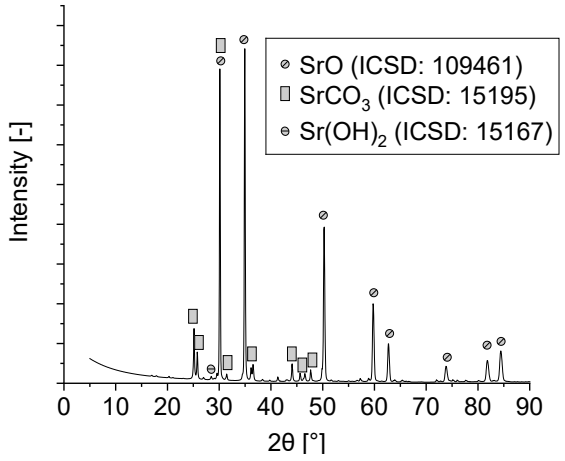

Figure 5.22: XRD spectrum of SrO after sorption experiment.

Figure 5.23 shows the effect of CaO in a CaO-SrO mixture on the H_2S concentration. It can be seen that in a CaO rich sorption material (90Ca10Sr) the CO_2 concentration increases after a few minutes. As explained earlier, CaO cannot reduce CO_2 any longer. Since CO_2 and H_2S intensities do not run parallel for both 90Ca10Sr and 10Ca90Sr, it is assumed that a mixed phase is present that reduces sulfur well. The XRD analysis of

90Ca10Sr (see Figure 5.24) shows that three $Ca_{1-x}Sr_xO_2$ mixed crystal phases are present, two rich in Ca with a=4.838 Å and 4.859 Å and one rich in Sr with a=5.112 Å.

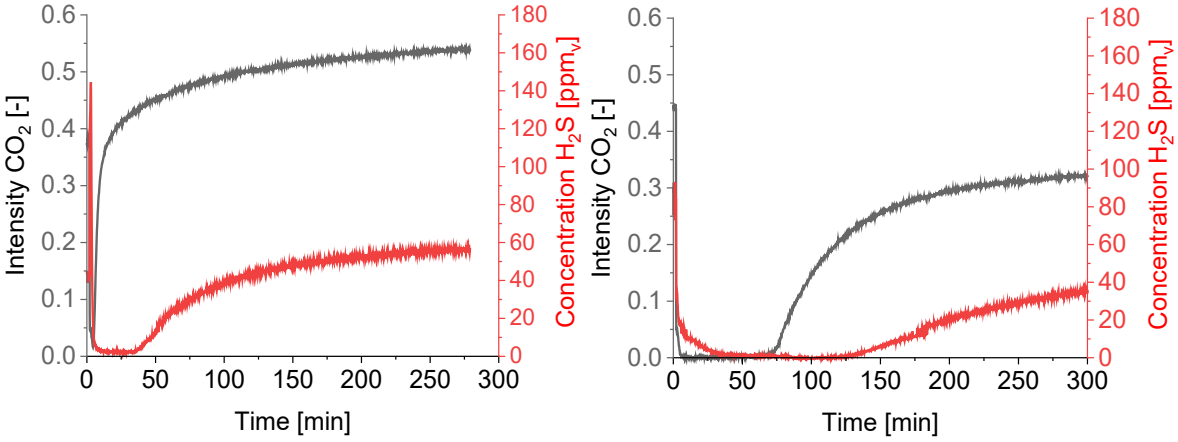

Figure 5.23: Results of the mass spectrometric investigations: Influence of CaO on the stabilization of the Sr-sorbent. CO_2 intensity and H_2S concentrations [ppm_v] of 90Ca10Sr (l.) and 10Ca90Sr (r.) (inlet concentration: 73 % H_2, 13 % Ar, 7 % H_2O, 1 % CO_2, 6 % CO (60 ppm_v H_2S), T = 650 °C, $\dot{V}_{tot}$ = 0,2 l/min, 100 g sorbent).

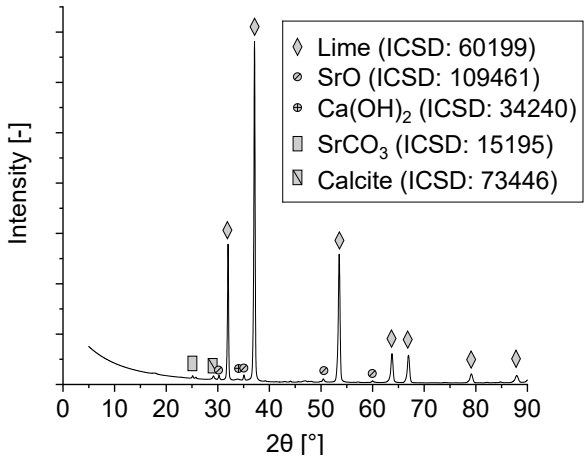

Figure 5.24: XRD spectrum of 90Ca10Sr after sorption experiment.

5.2.3 HCl sorption at 650 °C under reducing conditions

For the HCl sorption experiments the two sorbents with the lowest equilibrium concentration according to the model calculations (10Ba90Ca and SrO) were used. Similar to the KCl sorption experiments, the contamination was generated by evaporation of a source.

In order to prevent the BaO sorption material from being deactivated by CO_2 during the heating phase of the NH_4Cl, the heating tape was turned on 7 h before the gas was passed through the glass reactor. Thus, HCl concentrated in the reactor and the equilibrium plateau was reached after only a few minutes. Compared to the H_2S measurement (see Figure 5.18), the HCl sorption shows an earlier increase of CO_2 after only 20 minutes (see Figure 5.25).

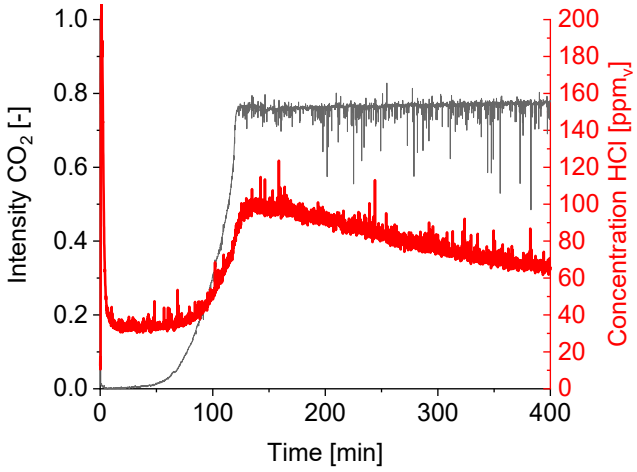

Figure 5.25: Results of the mass spectrometric investigations: CO_2 intensity and HCl concentrations [ppm_v] of 10Ba90Ca (inlet concentration: 73 % H_2, 13 % Ar, 7 % H_2O, 1 % CO_2, 6 % CO (50 ppm_v HCl), T = 650 °C, $\dot{V}_{tot}$ = 0,2 l/min, 100 g sorbent).

As in the H_2S sorption experiments, the sorption material in the HCl sorption experiments is deactivated by CO_2 in the syngas. The HCl signal in the 90Ca10Ba sorption measurement "shoots up" beyond the input concentration and decreases again. This is similar to the H_2S sorption measurement. It indicates that HCl is released.

The experimental procedure for SrO deviates a little. Here the heating tape, which was used for the evaporation of the NH_4Cl, was switched on two minutes before the glass reactor was opened. Since pure SrO was used here, the deactivation time was longer than for the Ba-based sorbent (see Figure 5.26).

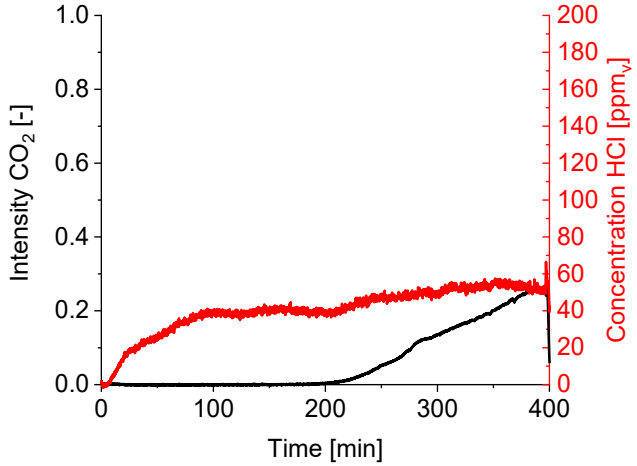

Figure 5.26: Results of the mass spectrometric investigations: CO_2 intensity and HCl concentrations [ppm_v] of SrO (inlet concentration: 73 % H_2, 13 % Ar, 7 % H_2O, 1 % CO_2, 6 % CO (50 ppm_v HCl), T = 650 °C, $\dot{V}_{tot}$ = 0,2 l/min, 100 g sorbent).

The tested sorbents are not able to noticeably reduce HCl concentrations. Both sorption materials can only reduce the HCl concentration for a short time by about 10-20 ppm_v: 10Ba90Ca lowers the HCl concentration for about 50 minutes from about 50 ppm_v (input concentration) to about 30 ppm_v, SrO for about 100 minutes from about 50 ppm_v (input concentration) to 40 ppm_v.

Moreover, neither for 10Ba90Ca, nor for SrO, Cl phases could be detected via XRD. This is due to the low HCl concentration in the syngas and the short deactivation time. Therefore, the samples were analyzed with EDXRF (see Figure A.4). Chlorine could be detected in all samples. However, only a semi-quantitative observation is possible. In contrast to the spectral lines of the other elements, the intensity of the chlorine K-alpha line varies strongly, indicating inhomogeneous chlorine distribution in the sample.

5.3 Filter candle-sorbents compatibility

This chapter summarizes the main results of the filter candles-sorbent studies. As described in Chapter 3.5, these consisted of the XRD investigations of the filter candle-sorbent pellets and the SEM/EDX analysis of the filter candle cross sections. The XRD spectra of all examined materials are shown in Figure A.5-Figure A.16.

Table 5.4 gives an overview of the phases formed with the sorbent during filter candle exposure. All sorbents except Zn_2TiO_4 and Ce_2O_3 reacted with the candles and thus, formed new phases.

Table 5.4: Overview of the detected phases depending on the sorbents and filter candles (XRD analysis).

Sorption material	Filter candle fiber	Formed phases
Zn_2TiO_4	Ca-Mg silicate	$Zn_2Ti_3O_8$
Ce_2O_3	Ca-Mg silicate	CeO_2
SrO	Ca-Mg silicate	Sr_2SiO_4, $SrCO_3$
90Sr10Ca	Ca-Mg silicate	Sr_2SiO_4, $SrCO_3$
BaO	Ca-Mg silicate	Ba_2SiO_4, $Ba_{1.3}Ca_{0.75}SiO_4$
90Ba10Ca	Ca-Mg silicate	Ba_2SiO_4, $Ba_{1.3}Ca_{0.75}SiO_4$
Zn_2TiO_4	Al-oxide silicate	$Zn_2Ti_3O_8$
Ce_2O_3	Al-oxide silicate	CeO_2
SrO	Al-oxide silicate	Sr_2SiO_4, $SrCO_3$, $Sr_3Al_2O_6$, $Sr(OH)_2(H_2O)$
90Sr10Ca	Al-oxide silicate	Sr_2SiO_4, $SrCO_3$, $Sr_3Al_2O_6$,
BaO	Al-oxide silicate	Ba_2SiO_4, $Ba_{1.3}Ca_{0.75}SiO_4$, $BaSiO_3$
90Ba10Ca	Al-oxide silicate	Ba_2SiO_4, $Ba_{1.3}Ca_{0.75}SiO_4$, $BaSiO_3$

The Ca-Mg silicate fiber filter candle formed silicates with the Sr- and Ba-based sorption materials (Sr_2SiO_4, Ba_2SiO_4). Ba-based sorbents additionally formed Ba-Ca silicates with the candles ($Ba_{1.3}Ca_{0.75}SiO_4$). The Al-oxide silicate fiber filter candle not only formed (Ca-) silicates with the Sr- and Ba-based sorbents (Sr_2SiO_4, Ba_2SiO_4), but also aluminates ($Sr_3Al_2O_6$).

The XRD analyses are compared with the SEM/EDX images in the following. Therefore, the transition zone between the sorption material and the filter candle (boundary layer) was examined. In particular, SEM/EDX images are shown of filter candles samples that have formed silicates with SrO or BaO.

Figure 5.27 and Figure 5.28 show the boundary layers of SrO, respectively BaO, and the Al-oxide silicate filter candle. Figure 5.29 and Figure 5.30, on the other hand, show the

boundary layers of SrO/BaO and the Ca-Mg silicate filter candle. The corresponding tables (Table 5.5-Table 5.7) show the composition in atom-% at the points marked in the figures.

Both Figure 5.27 and Figure 5.28 show a nucleus of Al-O-Si in the area of the boundary layer. Around the nucleus, there is another layer of Al-O-Si-Sr or Al-O-Si-Ba. Although the structure is round (possibly spherical), it is unlikely that one of the phases melted at 650 °C and caused this shape. The eutectic points of SiO_2 and BaO, respectively SiO_2 and SrO are well above 1000 °C. The round structure could be a cross-section of a single fiber. The sorption material may have been in excess locally and has completely overlapped the Si-O-Al nucleus and diffused into it.

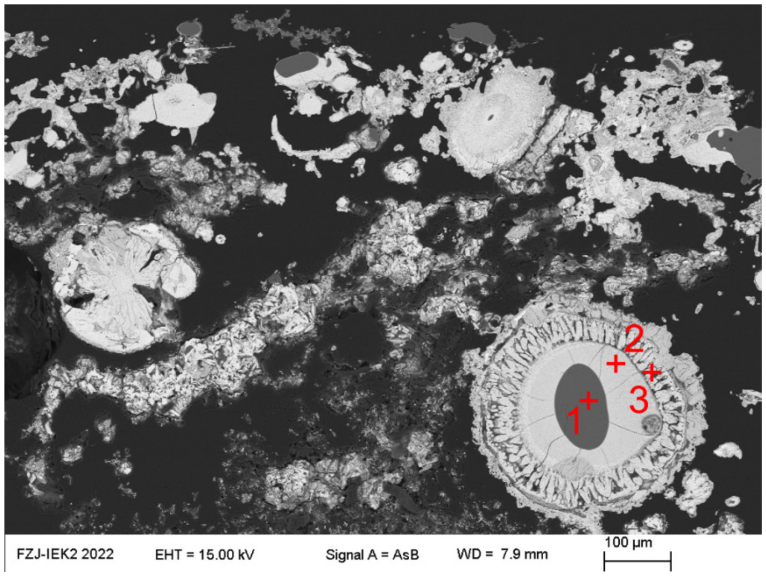

Figure 5.27: SEM of cross-section of the Al-oxide silicate fiber filter candle after exposure on SrO.

Table 5.5: Concentrations at spectrum labels of Figure 5.27 [atom-%].

Spectrum Label	O	Na	Mg	Al	Si	K	Ca	Sr
Spectrum 1	63.2	0.1	0.0	20.8	16.0	0.0	0.0	0.0
Spectrum 2	56.0	0.5	0.0	12.3	6.1	0.1	0.0	24.9
Spectrum 3	56.0	0.0	0.0	11.1	6.2	0.0	0.1	26.5

In the case of Ca-Mg silicate fiber filter candle, no round nucleus consisting of Al-O-Si can be detected. Instead, a sharper boundary has formed between sorbents and filter candle material (see Figure 5.29 and Figure 5.30).

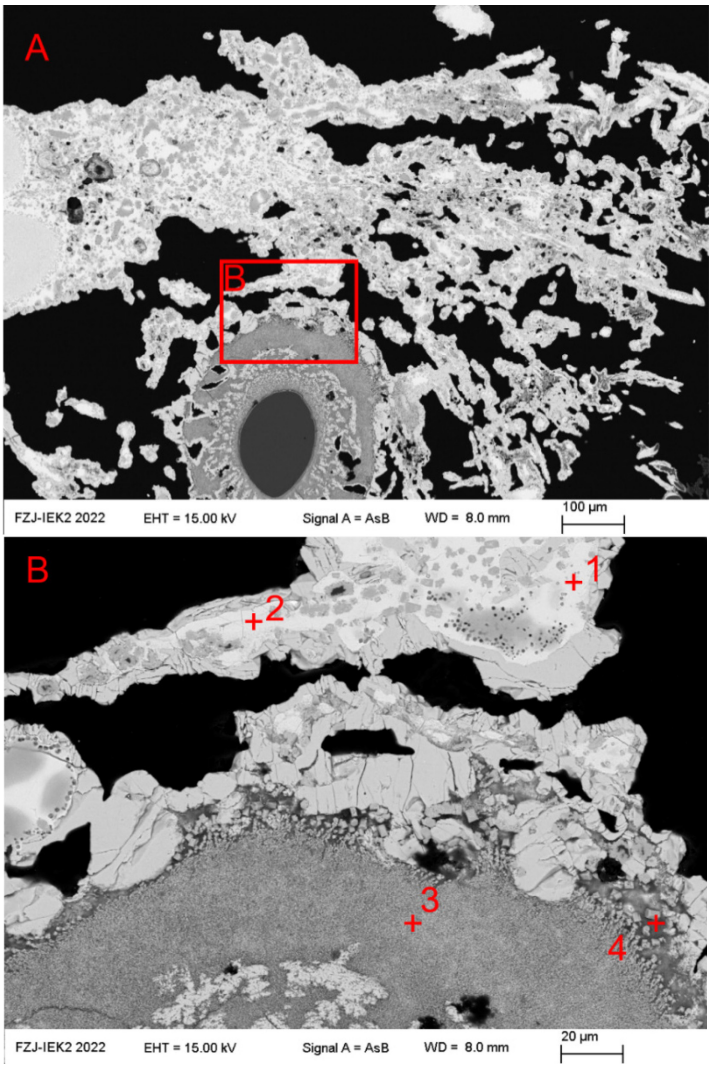

Figure 5.28: SEM of cross-section of the Al-oxide silicate fiber filter candle after exposure on BaO.

Table 5.6: Concentrations at spectrum labels of Figure 5.28 [atom-%].

Spectrum Label	O	Na	Mg	Al	Si	K	Ca	Ba
Spectrum 1	55.7	0.0	0.0	3.1	10.0	0.0	0.0	31.2
Spectrum 2	55.9	0.0	0.0	2.7	10.5	0.0	0.0	30.9
Spectrum 3	57.9	0.0	0.0	16.1	7.8	0.0	0.0	18.2
Spectrum 4	59.9	0.0	4.8	1.1	19.2	0.1	0.0	14.6

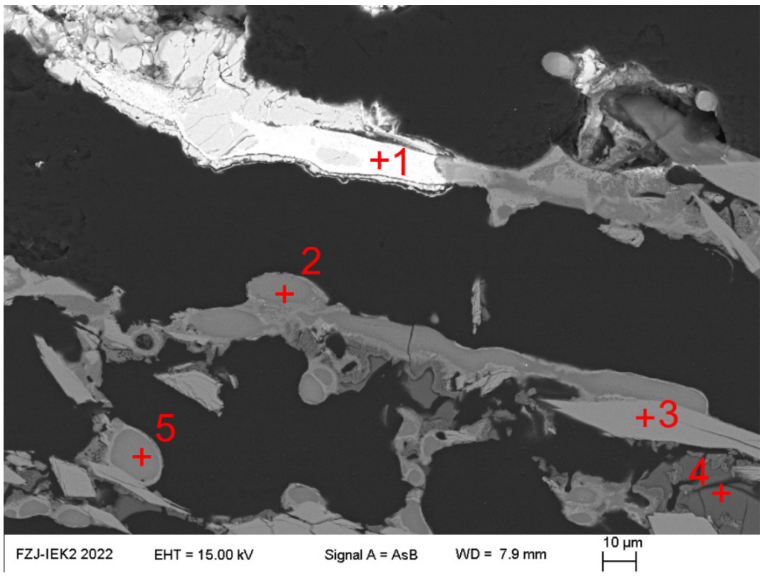

Figure 5.29: SEM of cross-section of the Ca-Mg silicate fiber filter candle after exposure on SrO.

Table 5.7: Concentrations at spectrum labels of Figure 5.29 [atom-%].

Spectrum Label	O	Na	Mg	Al	Si	K	Ca	Sr
Spectrum 1	56.2	0.0	0.0	3.1	10.5	0.0	0.6	29.1
Spectrum 2	58.3	7.0	3.4	8.4	15.8	0.5	4.5	0.0
Spectrum 3	59.8	0.0	0.0	0.0	19.7	0.0	20.3	0.0
Spectrum 4	66.5	0.1	0.0	0.0	33.2	0.1	0.1	0.0
Spectrum 5	58.4	6.2	2.8	8.5	15.7	0.6	6.0	0.0

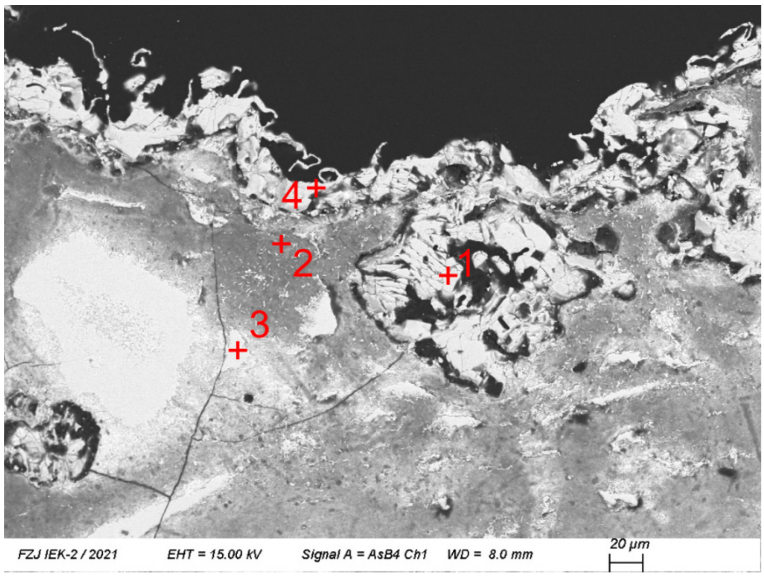

Figure 5.30: SEM of cross-section of the Ca-Mg silicate fiber filter candle after exposure on BaO.

Points 1, 2, and 4 in Figure 5.30 could not be quantified because of the high C content. This indicates an increased $BaCO_3$ content. Points 2 and 3 show a significant Al and Si content in addition to Ba.

Due to the different reactions occurring between BaO, respectively SrO, and the filter candles, these sorption materials should not be integrated directly into the filter candles. The gas flow through the filter candle could be blocked or the filter candle could suffer further damage such as cracks. However, Zn_2TiO_4 and Ce_2O_3 can be potentially integrated into the investigated filter candles, since XRD and EDX analysis did not show any new phases.

6 Discussion and recommendations

In this chapter, the key statements of the FactSage model are contrasted with the key statements of the laboratory experiments. Furthermore, the results of the modeling and the laboratory experiments (release, sorption, and exposure experiments) presented in this work are used to propose an HGC system for the GICO gasifier and calciner.

6.1 Comparison of the FactSage model with experimental observations

The model of the gasifier, calciner, and HGC presented in Chapter 3.2 is based on thermodynamic equilibrium calculations. The calculated values for the gas concentrations, which were used as a guide in the sorption experiments, should therefore only be regarded as well-founded theoretical values. Furthermore, the quality (e.g. degree of contamination with inorganics, H_2 yield, etc.) of the syngas depends on many parameters. Among others, the temperatures and pressures in the gasifier, the mixing of the bed material and the fuel, and the purity of the used biomasses have to be mentioned.

Since experiments were carried out for the gasifier side, key results of this work can be verified, namely the expected amount of ash produced during gasification, the type and amount of syngas contamination, and the functionality of the sorbents used in the HGC:

For the evaluation of the model regarding the degree of contamination during gasification, the biomass release experiments using MBMS are suitable. Using this method, it is possible to semi-quantitatively identify the inorganic trace substances. Furthermore, the model also makes statements about the amount of ash produced and its components.

Table 6.1 compares all trace substances appearing in the model and in the release experiments. Since the detection limit of the MBMS is in the ppb range, all inorganic components that have a concentration greater than 1 ppb in the model are listed.

Table 6.1 Comparison of the inorganic trace substances detected experimentally and by the model. Gas components in parentheses were not measured by MBMS (NH_3 and HCN), or could not be clearly detected or quantified due to overlays (HCl and KOH).

Biomass	Emerging trace substances	
	in model	in release experiments
Green Waste	H_2S, HCl, NaCl, KCl, COS, (NH_3, HCN)	H_2S, (HCl), NaCl, KCl, COS, (KOH), SO_2, PO_2, P_2
Green Waste Hydrochar	H_2S, HCl, NaCl, KCl, COS, (NH_3, HCN)	H_2S, (HCl), NaCl, KCl, COS, (KOH), SO_2, PO_2, P_2
OFMSW	H_2S, HCl, NaCl, KCl, COS, (NH_3, HCN)	H_2S, (HCl), NaCl, KCl, COS, (KOH), SO_2, PO_2, P_2
OFMSW Hydrochar	H_2S, HCl, NaCl, KCl, COS, (NH_3, HCN)	H_2S, (HCl), NaCl, KCl, COS, (KOH), SO_2, PO_2, P_2
Out-of-use woods	H_2S, HCl, NaCl, KCl, COS, NaOH, KOH, (NH_3, HCN)	(HCl), NaCl, KCl, COS, (KOH), SO_2, PO_2, P_2
Out-of-use woods Hydrochar (treated with water)	H_2S, HCl, NaCl, KCl, COS, (NH_3, HCN)	(HCl), NaCl, KCl, COS, (KOH), SO_2, PO_2, P_2
Out-of-use woods Hydrochar (treated with whey)	H_2S, HCl, NaCl, KCl, COS, NaOH, KOH, (NH_3, HCN)	H_2S, (HCl), NaCl, KCl, COS, (KOH), SO_2, PO_2, P_2
Grape Bagasse	H_2S, HCl, NaCl, KCl, COS, NaOH, KOH, (NH_3, HCN)	H_2S, (HCl), NaCl, KCl, COS, (KOH), SO_2, PO_2, P_2
Grape Bagasse Hydrochar	H_2S, HCl, NaCl, KCl, COS, NaOH, KOH, (NH_3, HCN)	H_2S, (HCl), NaCl, KCl, COS, (KOH), SO_2, PO_2, P_2

Since the sample material was added discontinuously, the gas components are not in equilibrium. Nevertheless, a large part of the model gases, e.g. H_2S, NaCl, KCl, and COS can be found in the gases in the release experiments. HCl and KOH were overlaid by water clusters and could not be quantified separately. Essentially, the model only differs from the experiments in the three gases, i.e. SO_2, PO_2, and P_2.

SO_2 was detected in the release experiments on mass 64. Even though a high gas volume flow rate (4 l/min) was used, a small amount of oxygen was present during the release leading to the oxidation of H_2S. The intensity of oxygen, which was measured on mass 32, is about ten times higher than that of H_2S in the empty tube (see Figure 3.5). The high 64 signal could also be explained by the presence of sulfur in the biomass as sulfate. The ash still contained sulfates after the release experiments, which support this conclusion (see Table 5.3).

Phosphorus could be determined by ICP-OES in three biomasses, i.e. OFMSW, OFMSW Hydrochar, and Grape Bagasse (see Table 5.1). In the other biomasses, phosphorus may be present but was below the detection limit of ICP-OES (0.2 wt-%). In the calculations, phosphorus appears mainly as a mineralized phase in the ash. Table 6.2 shows the phosphorus-containing phases appearing in the Factsage model and in the ash after the release experiment measured by XRD.

Table 6.2: Phosphorus phases and ash content in Factsage model and in ash after release experiment

Biomass	Phosphorus phases	
	FactSage model	Ash (see Table 5.3)
OFMSW	$KPMgO_4$, $CaK_4P_2O_8$ (19.1 wt-%)	$Ca_5(PO_4)_3OH$ (30-50 wt-%)
OFMSW Hydrochar	$Ca_7P_2Si_2O_{16}$, $KPMgO_4$, $CaKPO_4$ (46.2 wt-%)	$Ca_5(PO_4)_3OH$ (30-50 wt-%)
Grape Bagasse	$KPMgO_4$, $CaK_4P_2O_8$ (20.6 wt-%)	Quantification not possible

The mass fractions of the phosphorus-containing phases in the ashes are of the same order of magnitude in the FactSage model and in the XRD measurement. In this respect it can be stated that the model qualitatively correctly reflected an increased phosphorus concentration in the ash. However, the $Ca_5(PO_4)_3OH$ phase found in the ashes is not present in the database. As a result, alternative phosphorus-containing components have been adopted by the model.

Figure 6.1 shows the masses of the ashes produced relative to the raw biomass in the release experiments and in the computational model. Although the calculated and experimentally determined values do not match in most cases, a clear agreement in tendency can be seen. Green waste has the highest ash content in both observations, while Out-of-use woods has virtually no ash after gasification with steam.

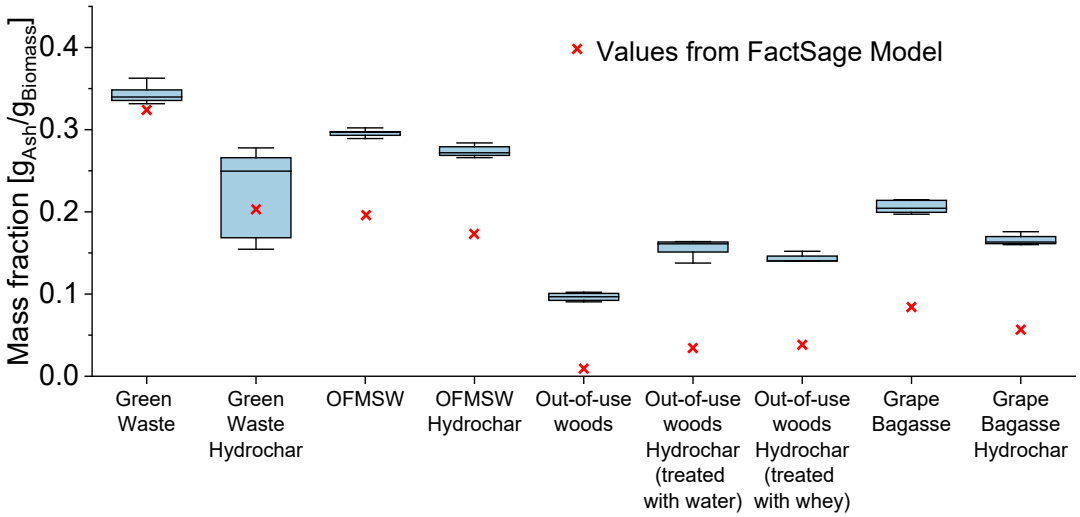

Figure 6.1: Comparison of the experimental ash fractions with the predicted ash fractions.

According to experimental and calculated results, the order of the remaining biomasses is also consistent. It is noticeable that in most cases, the calculated values deviate from the measured values quite exactly by 10 %. This can be explained by the fact that the state of equilibrium between the gas atmosphere and the sample has not yet been reached after 5 minutes in the furnace.

For the evaluation of the HGC model, the data obtained in the sorption experiments can be used: Aluminosilicates showed good reduction potential for the alkali compounds KCl and NaCl in the calculations. This can be confirmed by laboratory experiments with MBMS. The tested aluminosilicates reduced the KCl concentration to levels well below 1 ppm_v in the experiments.

Similar observations can be made for the H_2S sorption. According to the calculations, Ce_2O_3, BaO, and SrO can significantly reduce H_2S concentration below 1 ppm_v. This is also verified by the fixed bed sorption experiments. However, since the detection limit of the used mass spectrometer is about 1 ppm_v, no conclusions can be drawn about the actual purities of the gas for these three sorption materials. An increased H_2 concentration

was also predicted for all three sorbents, which was also experimentally demonstrated. In comparison to the materials mentioned above, Zn_2TiO_4 was used as a conventional sorbent. Calculations and experiments prove that there is no deactivation by CO_2 here. The H_2S concentration achieved in the sorption experiment is also within the range of the model (1-10 ppm_v).

Only the experiments for HCl sorption deviate strongly from the predictions. The tested sorbents could not really reduce HCl. This may be due to incorrect or insufficient data in the database and the non-consideration of kinematic effects, since only equilibria are covered by the model.

6.2 HGC concept for the GICO-Process

In this work, both calculations and experiments were carried out that show the potentials and risks of HGC. The HGC is an extremely complex topic and its good functioning depends on many influencing factors, a few of which are:

- Knowledge about the concentrations of S, Cl, K, Na in the used biomasses in order to be able to estimate the concentrations of inorganics in the syngas
- Good temperature control of reactor and pipes to prevent condensation of chlorides, oxides, sulfates, and sulfides
- Ensuring a low CO_2 concentration that potentially deactivates the presented sorbents by forming carbonates or oxidize them
- Ensuring enough H_2O for the integration of alkalis into the aluminosilicate structure
- Ensuring enough O_2 to ensure the formation of $CaSO_4$ and reduce the SO_2 concentration

If these factors are observed, then the concept presented, consisting of an alkali cleaning unit with aluminosilicates and a combined sour gas cleaning unit for both sides (gasification and calcination), can be possible in terms of thermodynamic feasibility and offer a few good trade-offs. Ba-based sorption materials may be expensive to purchase and manufacture, but can be used for both HGC sides, for example, as an oxide or as a carbonate. Carbonates can also be regenerated or used further to reduce the SO_2/HCl concentration on the calciner side.

6.2.1 HGC concept gasification side

Chapters 4.2 and 5.2.2 indicate that the reduction of H_2S at 650 °C using either Ce_2O_3, SrO or BaO is only possible if the syngas had a low CO_2 content, since these sorbents are deactivated by carbonation or oxidation. Therefore, a low CO_2 content is beneficial when utilizing Ce_2O_3, SrO or BaO for high-temperature sorption. However, the GICO experimental plant may not achieve this theoretical value in its fluidized bed. CO_2 concentrations between 3-5 % are expected [39].

To address this, a CO_2 polishing reactor that could decrease the CO_2 content can be added to the HGC unit of the gasifier side (see Figure 6.2). This reactor can be designed as a moving granular bed reactor intended to renew the spent sorbent continuously. Since aluminosilicates were able to reduce the alkali concentrations to the sub ppm_v range in the sorption experiments at 650 °C, the gas does not have to be cooled down before alkali cleaning. Since HCl is released during alkali binding into aluminosilicates (reaction 2.12), HCl cleaning must be carried out downstream in the process. A hot gas filter to remove particles is integrated after the alkali cleaning unit operating at 650 °C. It is important that the alkali cleaning is carried out before the filter so that it does not become clogged due to the condensation of alkali components. Afterwards, the gas reaches the H_2S sorption reactor. Since CaO in the CO_2 polishing reactor reacts not only with CO_2, but also with H_2S and HCl, a reduced concentration of around 20 ppm_v and 160 ppm_v (see Figure 4.7) can be assumed here.

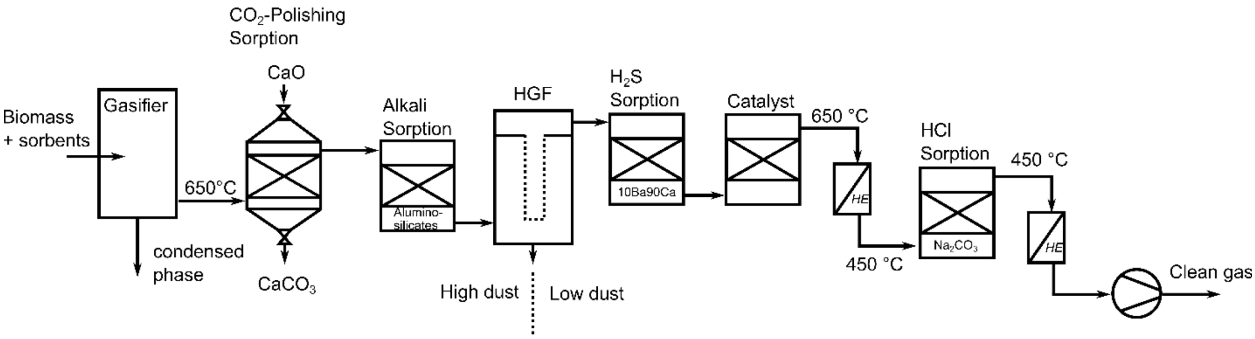

Figure 6.2: Layout of a high temperature HGC for syngas cleaning.

To ensure the cracking of tar, the gas is lead through another reactor operating at 650 °C. Preliminary stability tests conducted within the GICO-Project show complete tar conversion with a commercially available catalyst K57-7 from Johnson Matthey at 650 °C for a gas with 20 ppm_v H_2S and GHSV < 3000 h^{-1}. This means that the catalyst is still

active even if the H_2S cleaning unit fails. The HCl-stability of the tar cracking catalyst, however, has yet to be tested.

Since a sufficient HCl reduction by Ba- or Sr-based sorbents could not be confirmed experimentally (see Chapter 5.2.3), adsorption by alkali carbonates is proposed. For successful HCl purification with Na_2CO_3, the temperature has to be lowered to 450 °C in a heat exchanger. At temperatures above 550 °C the sorption of HCl is not feasible as Na-based sorbents will release some of the chlorine as NaCl. The gas temperature can then be adjusted in another heat exchanger, according to the conditions of the downstream equipment. The side-channel blower will extract the gas flow from the various gas cleaning steps and forward it to the downstream process.

The HGC can be designed to operate also at medium temperature (see Figure 6.3). Here, the alkali sorption is again carried out with aluminosilicates. ZnO or Zn_2TiO_4 can replace the expensive H_2S sorbents SrO and BaO in this variant. As ZnO has a higher vapor pressure (see Chapter 4.2.2), this version requires a lower temperature for H_2S sorption. The heat exchanger, which lowers the gas temperature from 650 °C to 450 °C, can be installed either upstream or downstream of the hot gas filter. Moreover, since ZnO does not react with CO_2 at 450 °C, this sorbent is not deactivated. A CO_2 polishing unit is not necessary.

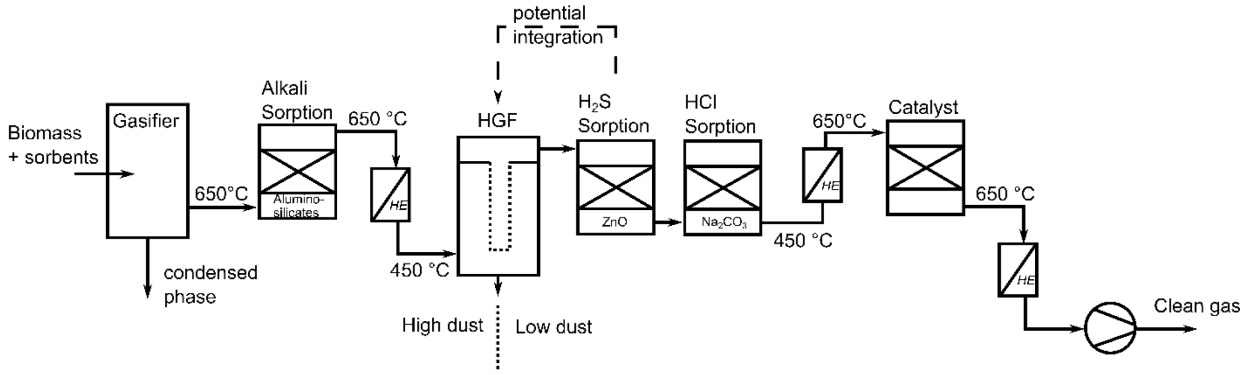

Figure 6.3: Layout of a medium temperature HGC for syngas cleaning.

An additional heat exchanger is necessary to reheat the gas before entering the catalytic tar cracking reactor. However, this solution might be more economical than the high-temperature version (see Figure 6.2) due to the fact that the hot gas filter is more cost-effective at lower gas temperatures [151]. In this version, the Zn-sorbent can be integrated

directly into the hot gas filter, which enables a space-saving design. According to Chapter 5.3, the formation of a new phase is not expected. The temperature reduction is determined by the maximum operating temperature of the H_2S and HCl sorption reactors.

The concepts presented in Figure 6.2 and Figure 6.3 basically only differ in the temperature at which the H_2S sorption unit is operated, as the syngas has to be cooled to 450 °C to remove the HCl in both variants. However, by using biomasses that are low in chlorine, e.g. Grape Bagasse, HCl purification may not be necessary even after alkali purification. This means that the syngas temperature can be maintained after H_2S purification. Therefore, it is essential to investigate the maximum HCl compatibility of the downstream equipment.

6.2.2 HGC concept calcination side

Figure 6.4 shows a potential layout of the HGC unit for the CO_2-rich calciner gas. The temperature of the flue gas leaving the calciner is set to 920 °C (see Figure 6.4). Since aluminosilicates have already proven themselves in this temperature range for alkali cleaning [49], they are used in the HGC on the calcination side.

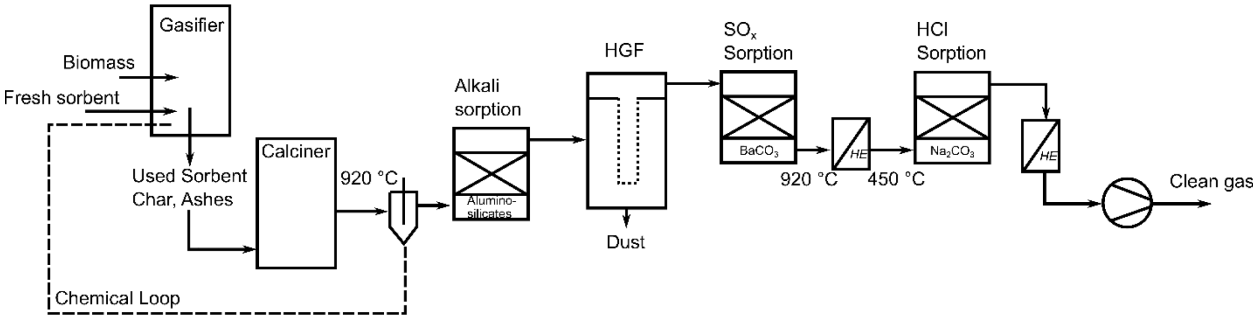

Figure 6.4: Layout of the HGC for calciner gas.

Similar to the HGC concept on the gasifier side, a hot gas filter is used after alkali cleaning to remove particles. $SrCO_3$, $BaCO_3$, and lime-based sorbents can be used to reduce SO_x whose concentration may already be low (see Figure 4.24). Again, a heat exchanger is needed to decrease the gas temperature for HCl removal. Similar to the HGC on the gasification side, Na-based sorbents can be used for HCl removal at 450 °C. The temperature of the gas leaving the HGC unit can be adapted to the demands of the downstream, e.g. the CO_2 storage tank and the plasma torch units, via an additional heat exchanger.

7 Summary and outlook

FactSage calculations have shown that the primary sorbent CaO has a supporting effect in hot gas cleaning and reduces the H_2S in the gasifier to 20 ppm_v and the HCl concentrations to 160 ppm_v. CaO, which reacts to CaS or $CaCl_2$, is deactivated for CO_2 capture and must be replaced. The calculations determine the percentage of CaO on the total bed material consisting of CaO, $CaSO_4$, and $CaCl_2$ after calcination to be between 99.01 wt-% (Green Waste) and 99.76 wt-% (Out-of-use woods).

Because slag-forming ash components pose a risk to the efficient operation of the gasifier and calciner, the ash composition of various project biomasses was determined. Based on this, the melting behavior was investigated. At 920 °C, however, all biomasses examined in the modeling show a slag phase. The lowest slag content in relation to the input biomass, namely 9 wt-%, is found in Out-of-use woods. Out-of-use woods also have a low ash content in relation to the biomass, which makes it the most suitable examined biomass for gasification in terms of slag minimization.

Extensive calculations were conducted for the HGC units of the gasifier and calciner, proving that Sr- and Ba-based sorbents not only sufficiently reduce the H_2S/SO_2, but also the HCl concentration into the sub ppm_v range. Additional condensation calculations stressed the need for temperature resistant H_2S sorbents, because conventional ones, such as zinc titanate, tend to evaporate leading to the condensation of unwanted salts and oxides. According to the calculations, used H_2S/HCl sorption material such as $BaCO_3$ and $SrCO_3$ can be reused as SO_2/HCl sorbents on the calciner side.

MBMS release experiments, focusing on the little-investigated medium temperature, showed that intensive water-leaching hardly affects the concentrations of trace substances, such as H_2S, SO_2, KCl or NaCl, released during gasification at 650 °C. The peak areas of the trace substances of the water-leached biomass samples tend to be lower than those of the untreated samples, however, the concentrations are within the standard deviation. The concentration of trace substances released from the HTC samples is higher than that of the untreated and water-leached biomass samples, although ICP-OES measurements show that there are significantly lower inorganic trace substance concentrations in the HTC samples. Biomass samples that have been mixed with CaO show a

reduced amount of inorganic trace compounds released overall, but also affect the release behavior of K and Na components: Besides a first volatile peak, a second peak, similar in size, occurs indicating the release of further alkali components.

Sorption experiments in lab-scale furnaces were conducted to determine if chemical hot gas cleaning concepts can effectively remove alkali and sour gas components from a gasification unit operating at 650 °C. Six aluminosilicates have been proven to be suitable for KCl reduction to values below 1 ppm_v, four of them reduced the concentrations to values below 400 ppb_v after 20 h. Zinc titanate, as the best tested conventional sulfur sorbent, only reduced the H_2S concentration to around 7 ppm_v. Ba-, Sr-, and Ce-containing sorbents achieved H_2S concentrations below 1 ppm_v, which should be sufficient to prevent poisoning of the nickel catalyst.

As shown in the exposure experiments, Sr- and Ba-sorbents react with the filter candles to form silicates, i.e. Sr_2SiO_4, Ba_2SiO_4, $Ba_{1.3}Ca_{0.75}SiO_4$, $BaSiO_3$, and aluminum phases, i.e. $Sr_3Al_2O_6$. It is therefore not recommended to integrate these sorbents directly into the filter candles. This could block the gas flow or cause further damage, such as cracks, to the filter candle. However, Zn_2TiO_4 and Ce_2O_3 could potentially be integrated into the investigated filter candles, as the XRD and EDX analysis did not reveal any new phases.

Last but not least, a chemical hot gas cleaning concept was proposed that could meet the needs of the GICO-Process which should now be tested continuously in a medium-sized test stand under realistic conditions. For this purpose, Calida Cleantech GmbH has built an HGC unit that can convey 2.5 m^3/h of gas (see Figure 7.1).

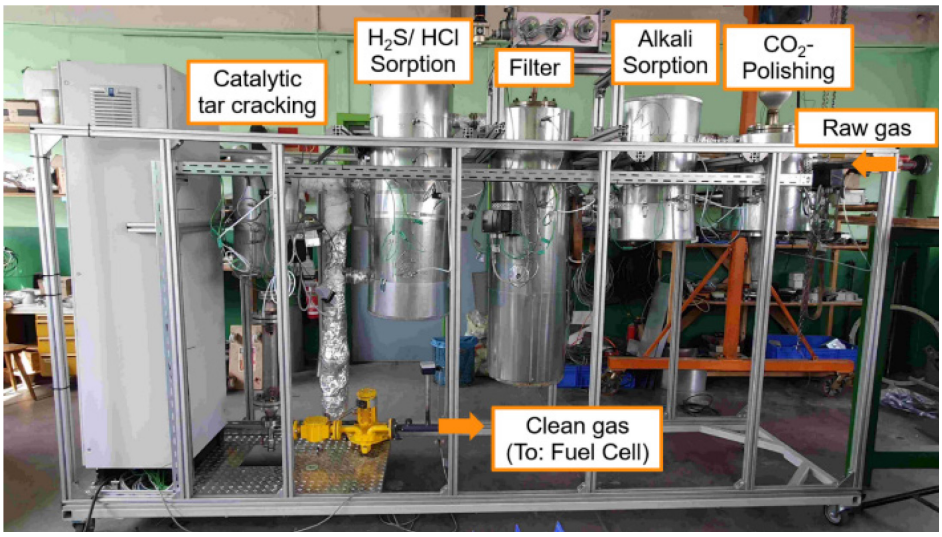

Figure 7.1: Front view of the assembled hot gas conditioning system.

This unit consists of a CaO-polishing unit, an aluminosilicate fixed bed, filter candles, a catalyst for tar cracking and a fixed bed reactor for the H_2S and HCl removal.

Following these experiments, economic considerations must now be made. The use of the rather more expensive temperature-resistant Sr- and Ba-based sorbents used in this work can only be justified if extremely low H_2S concentrations are required for the operation of downstream equipment or if they make the cooling of the synthesis gas, which is necessary for the use of conventional sorbents, obsolete. In order to increase the capacity of the sorbents, further studies aimed at increasing the specific surface area of the sorbents are desirable. The reuse of Sr- and Ba-based sorption materials in the carbonate form must also be included in the economic analysis. In particular, it must be clarified which HCl impurities on the calciner side are still tolerable with regard to reliable operation of the membrane.

8 References

[1] P. Fennell, B. Anthony (Eds.), Calcium and Chemical Looping Technology for Power Generation and Carbon Dioxide (CO_2) Capture, Elsevier Science & Technology; ProQuest, Cambridge, Ann Arbor, Michigan, 2015.

[2] M. Latif, Countdown. Unsere Zeit läuft ab - was wir der Klimakatastrophe noch entgegensetzen können, Herder, Freiburg, Basel, Wien, 2022.

[3] S. Boehm, C. Schumer, 10 Big Findings from the 2023 IPCC Report on Climate Change, 2023.

[4] P. Icha; T. Lauf, Energiebedingte Emissionen von Klimagasen und Luftschadstoffen, 2023. https://www.umweltbundesamt.de/daten/energie/energiebedingte-emissionen.

[5] Enerdata, Internet document. World Energy & Climate Statistics. Consumption. https://yearbook.enerdata.net/total-energy/world-consumption-statistics.html (11.12.2023).

[6] Bundesministerium für Ernährung und Landwirtschaft 2024, Internet document. Nutzen und Bedeutung der Bioenergie. Accessed 11.01.2024. https://www.bmel.de/DE/themen/landwirtschaft/bioeokonomie-nachwachsende-rohstoffe/bioenergie-nutzen-bedeutung.html (11.01.2024).

[7] European Union, Homepage GICO Project-GICO Process. Accessed 14.07.2024. https://www.gicoproject.eu/gico-process/ (14.07.2024).

[8] S. Hafner, M. Schmid, G. Scheffknecht, Parametric Study on the Adjustability of the Syngas Composition by Sorption-Enhanced Gasification in a Dual-Fluidized Bed Pilot Plant, Energies 14 (2021) 399.

[9] A. Pudi, M. Rezaei, V. Signorini, M.P. Andersson, M.G. Baschetti, S.S. Mansouri, Hydrogen sulfide capture and removal technologies: A comprehensive review of recent developments and emerging trends, Separation and Purification Technology 298 (2022) 121448.

[10] W. Duo, N.F. Kirkby, J. Seville, J. Kiel, A. Bos, H. den Uil, Kinetics of HCl reactions with calcium and sodium sorbents for IGCC fuel gas cleaning, Chemical Engineering Science 51 (1996) 2541–2546.

[11] M. Stemmler, A. Tamburro, M. Müller, Laboratory investigations on chemical hot gas cleaning of inorganic trace elements for the “UNIQUE” process, Fuel 108 (2013) 31–36.

[12] M. Stemmler, A. Tamburro, M. Müller, Thermodynamic modelling of fate and removal of alkali species and sour gases from biomass gasification for production of biofuels, Biomass Conv. Bioref. 3 (2013) 187–198.

[13] T. Shimizu, T. Hirama, H. Hosoda, K. Kitano, M. Inagaki, K. Tejima, A Twin Fluid-Bed Reactor for Removal of CO_2 from Combustion Processes, Chemical Engineering Research and Design 77 (1999) 62–68.

[14] J. Blamey, E.J. Anthony, J. Wang, P.S. Fennell, The calcium looping cycle for large-scale CO_2 capture, Progress in Energy and Combustion Science 36 (2010) 260–279.

[15] C.C. Dean, J. Blamey, N.H. Florin, M.J. Al-Jeboori, P.S. Fennell, The calcium looping cycle for CO_2 capture from power generation, cement manufacture and hydrogen production, Chemical Engineering Research and Design 89 (2011) 836–855.

[16] C. Han, D.P. Harrison, Simultaneous shift reaction and carbon dioxide separation for the direct production of hydrogen, Chemical Engineering Science 49 (1994) 5875–5883.

[17] R. Barker, The reversibility of the reaction $CaCO_3 \rightleftarrows CaO+CO_2$, J. Appl. Chem. 23 (1973) 733–742.

[18] S.K. Bhatia, D.D. Perlmutter, Effect of the product layer on the kinetics of the CO_2-lime reaction, AIChE Journal 29 (1983) 79–86.

[19] J.S. Dennis, R. Pacciani, The rate and extent of uptake of CO_2 by a synthetic, CaO-containing sorbent, Chemical Engineering Science 64 (2009) 2147–2157.

[20] S. Scaccia, S. Stendardo, G. Vanga, L. Pagliari, S. Cassani, M. Nobili, G. Messina, A. Assettati, G. Guidarelli, S. Attanasi, C. Stringola, A. Grasso, I. Cassani, A. Calabró, P.U. Foscolo, The Italian ZECOMIX Platform: CO_2 Capture on Calcined Dolomite in Fluidized Bed Carbonator Unit, Natural Resources (2014) 433–441.

[21] A.M. Kierzkowska, L.V. Poulikakos, M. Broda, C.R. Müller, Synthesis of calcium-based, Al_2O_3-stabilized sorbents for CO_2 capture using a co-precipitation technique, International Journal of Greenhouse Gas Control 15 (2013) 48–54.

[22] H. Lu, E.P. Reddy, P.G. Smirniotis, Calcium Oxide Based Sorbents for Capture of Carbon Dioxide at High Temperatures, Ind. Eng. Chem. Res. 45 (2006) 3944–3949.

[23] Y. Dai, P. Lu, Z. Cao, C.T. Campbell, Y. Xia, The physical chemistry and materials science behind sinter-resistant catalysts, Chemical Society Reviews 47 (2018) 4314–4331.

[24] J.A. Conkling, C.J. Mocella, Chemistry of pyrotechnics. Basic principles and theory, CRC Press; Taylor & Francis Group, Boca Raton (Fla.), London, New York, 2019.

[25] A. Silaban, M. Narcida, D.P. Harrison, Characteristics of the reversible reaction between CO_2 (g) and calcined dolomite, Chemical Engineering Communications 146 (1996) 149–162.

[26] J. Fuchs, J.C. Schmid, S. Müller, H. Hofbauer, Dual fluidized bed gasification of biomass with selective carbon dioxide removal and limestone as bed material: A review, Renewable and Sustainable Energy Reviews 107 (2019) 212–231.

[27] N. Hanchate, S. Ramani, C.S. Mathpati, V.H. Dalvi, Biomass gasification using dual fluidized bed gasification systems: A review, Journal of Cleaner Production 280 (2021) 123–148.

[28] J. Corella, J.M. Toledo, G. Molina, A Review on Dual Fluidized-Bed Biomass Gasifiers, Ind. Eng. Chem. Res. 46 (2007) 6831–6839.

[29] H. Guan, X. Fan, B. Zhao, L. Yang, R. Sun, Application and Discussion of Dual Fluidized Bed Reactor in Biomass Energy Utilization, IOP Conf. Ser.: Earth Environ. Sci. 108 (2018).

[30] J. Baeyens, L. Shuo, R. Dewil, H. Zhang, Y. Deng, Fluidized Bed Technology: Challenges and Perspectives, IOP Conf. Ser.: Earth Environ. Sci. 952 (2022) 12010.

[31] C. Srinivasakannan, N. Balasubramanian, Variations in the Design of Dual Fluidized Bed Gasifiers and the Quality of Syngas from Biomass, Energy Sources, Part A: Recovery, Utilization, and Environmental Effects 33 (2010) 349–359.

[32] J.C. Schmid, U. Wolfesberger, S. Koppatz, C. Pfeifer, H. Hofbauer, Variation of feedstock in a dual fluidized bed steam gasifier—influence on product gas, tar content, and composition, Env Prog and Sustain Energy 31 (2012) 205–215.

[33] A. Aghaalikhani, J.C. Schmid, D. Borello, J. Fuchs, F. Benedikt, H. Hofbauer, F. Rispoli, U.B. Henriksen, Z. Sárossy, L. Cedola, Detailed modelling of biomass steam gasification in a dual fluidized bed gasifier with temperature variation, Renewable Energy 143 (2019) 703–718.

[34] J.C. Abanades, E.J. Anthony, J. Wang, J.E. Oakey, Fluidized bed combustion systems integrating CO_2 capture with CaO, Environ. Sci. Technol. 39 (2005) 2861–2866.

[35] M. Strelow, C. Schlitzberger, F. Röder, S. Magda, R. Leithner, CO_2 Separation by Carbonate Looping Including Additional Power Generation with a CO_2-H_2O Steam Turbine, Chemical Engineering & Technology 35 (2012) 431–439.

[36] J.C. Abanades Garcia; B. Arias Rozada; Diego de Paz, María Elena; I. Martínez Berges, System for CO_2 capture from a combustion flue gas using a $CaO/CaCO_3$ chemical loop. European Patent, EP13382206.4A (03.12.2014).

[37] D. Barisano, S. Stendardo, E. Savuto, U. Laverdura, A. Di Carlo, E. Ciro Zuleta, M. Kopsch, D.2.7. SEG (Sorption Enhanced Gasification) experiments in test rigs: measurement of process parameters and syngas quality. EU GICO-Project Report (restricted), Rome, 2023.

[38] S. Stendardo, I. Luisetto, U. Laverdura, A. Tacconi, E. Savuto, A. Di Carlo, D. Maury, D. Quaranta, M. Kopsch, D.2.3. CO_2 sorbent and reforming catalyst agent. EU GICO-Project Report (restricted), Rome, 2022.

[39] T.A. Centeno, M.A. Díez, L. Del Zotto, E. Bocci, S. Stendardo, D. Barisano, A. Di Carlo, M. Kopsch, D.2.1. Selection of feedstocks and their characterization. EU GICO-Project Report (public), Spain, 2021.

[40] A. Susastriawan, H. Saptoadi, Purnomo, Small-scale downdraft gasifiers for biomass gasification: A review, Renewable and Sustainable Energy Reviews 76 (2017) 989–1003.

[41] K. Cummer, Ancillary equipment for biomass gasification, Biomass and Bioenergy 23 (2002) 113–128.

[42] D. Monarca, A. Colantoni, M. Cecchini, L. Longo, L. Vecchione, M. Carlini, A. Manzo, Energy Characterization and Gasification of Biomass Derived by Hazelnut Cultivation: Analysis of Produced Syngas by Gas Chromatography, Mathematical Problems in Engineering 2012 (2012) 1–9.

[43] E. Bocci, M. Sisinni, M. Moneti, L. Vecchione, A. Di Carlo, M. Villarini, State of Art of Small Scale Biomass Gasification Power Systems: A Review of the Different Typologies, Energy Procedia 45 (2014) 247–256.

[44] M. Jaleta Dirbeba, J. Werkelin, Challenging Biomass Feedstocks for Energy and Chemicals, Biomass, Biorefineries and Bioeconomy (2022).

[45] E. Björkman, B. Strömberg, Release of Chlorine from Biomass at Pyrolysis and Gasification Conditions 1, Energy & Fuels 11 (1997) 1026–1032.

[46] J.G. Olsson, J.B.C. Pettersson, N. Padban, I. Bjerle, Alkali Metal Emission from Filter Ash and Fluidized Bed Material from PFB Gasification of Biomass, Energy & Fuels 12 (1998) 626–630.

[47] Y. Neubauer, Strategies for tar reduction in fuel-gases and synthesis-gases from biomass gasification, Journal of Sustainable Energy & Environment Special Issue (2011) 67–71.

[48] M. Ma, M. Müller, Investigation of various catalysts for partial oxidation of tar from biomass gasification, Applied Catalysis A: General 493 (2015) 121–128.

[49] M. Stemmler, Chemische Heißgasreinigung bei Biomassevergasungsprozessen. Fakultät für Maschinenwesen. RWTH Aachen University, PhD-Thesis, Aachen, 2010.

[50] H. Marschner, Mineral nutrition of higher plants, Academic Press, Amsterdam, 2002.

[51] G.S. Bañuelos, H.A. Ajwa, Trace elements in soils and plants: An overview, Journal of Environmental Science and Health, Part A 34 (1999) 951–974.

[52] D. Porbatzki, M. Stemmler, M. Müller, Release of inorganic trace elements during gasification of wood, straw, and miscanthus, Biomass and Bioenergy 35 (2011) S79-S86.

[53] D. Fan, Y. Lan, P.G. Tratnyek, R.L. Johnson, J. Filip, D.M. O'Carroll, A. Nunez Garcia, A. Agrawal, Sulfidation of Iron-Based Materials: A Review of Processes and Implications for Water Treatment and Remediation, Environmental Science & Technology 51 (2017) 13070–13085.

[54] R.W. Bryers, Fireside slagging, fouling, and high-temperature corrosion of heat-transfer surface due to impurities in steam-raising fuels, Progress in Energy and Combustion Science 22 (1996) 29–120.

[55] P. Kofstad, G. Akesson, Sulfate-induced high-temperature corrosion of nickel, Oxid Met 14 (1980) 301–323.

[56] C. Leyens, B.A. Pint, I.G. Wright, Hot Corrosion of Nickel-Base Alloys in Biomass-Derived Fuel Simulated Atmosphere, ElevatedTemperature Coatings: Science and Technology III (1999).

[57] C.M. Chun, J.D. Mumford, T.A. Ramanarayanan, Mechanisms of Metal Dusting Corrosion of Iron, J. Electrochem. Soc. 149 (2002) B348.

[58] J.C. Nava Paz, H.J. Grabke, Metal dusting, Oxid Met 39 (1993) 437–456.

[59] R.L. Bain, D.C. Dayton, D.L. Carpenter, S.R. Czernik, C.J. Feik, R.J. French, K.A. Magrini-Bair, S.D. Phillips, Evaluation of Catalyst Deactivation during Catalytic Steam Reforming of Biomass-Derived Syngas, Ind. Eng. Chem. Res. 44 (2005) 7945–7956.

[60] L. Lisi, G. Lasorella, S. Malloggi, G. Russo, Single and combined deactivating effect of alkali metals and HCl on commercial SCR catalysts, Applied Catalysis B: Environmental 50 (2004) 251–258.

[61] C.H. Bartholomew, Mechanisms of catalyst deactivation, Applied Catalysis A: General 212 (2001) 17–60.

[62] I.V. Mishakov, A.A. Vedyagin, Y.I. Bauman, A.R. Potylitsyna, A.S. Kadtsyna, V.V. Chesnokov, A.Y. Nalivaiko, A.A. Gromov, R.A. Buyanov, Two Scenarios of Dechlorination of the Chlorinated Hydrocarbons over Nickel-Alumina Catalyst, Catalysts 10 (2020) 1446.

[63] M. Aho, E. Ferrer, Importance of coal ash composition in protecting the boiler against chlorine deposition during combustion of chlorine-rich biomass, Fuel 84 (2005) 201–212.

[64] Q. Chen, J. Zhou, B. Liu, Q. Mei, Z. Luo, Influence of torrefaction pretreatment on biomass gasification technology, Chin. Sci. Bull. 56 (2011) 1449–1456.

[65] J.J. Chew, V. Doshi, Recent advances in biomass pretreatment – Torrefaction fundamentals and technology, Renewable and Sustainable Energy Reviews 15 (2011) 4212–4222.

[66] G. Wang, Y. Luo, J. Deng, J. Kuang, Y. Zhang, Pretreatment of biomass by torrefaction, Chin. Sci. Bull. 56 (2011) 1442–1448.

[67] A.N. Anoopkumar, R. Reshmy, E.M. Aneesh, A. Madhavan, L.L. Kuriakose, M.K. Awasthi, A. Pandey, P. Binod, R. Sindhu, Progress and challenges of Microwave-assisted pretreatment of lignocellulosic biomass from circular bioeconomy perspectives, Bioresource Technology 369 (2023) 128459.

[68] I. Barmina, L. Goldsteins, R. Valdmanis, M. Zake, Improvement of Biomass Gasification/Combustion Characteristics by Microwave Pretreatment of Biomass Pellets, Chem. Eng. Technol. 44 (2021) 2018–2025.

[69] Z. Hu, X. Ma, E. Jiang, The effect of microwave pretreatment on chemical looping gasification of microalgae for syngas production, Energy Conversion and Management 143 (2017) 513–521.

[70] Z. Ge, X. Cao, Z. Zha, Y. Ma, M. Zeng, Y. Wu, H. Zhang, The influence of a two-step leaching pretreatment on the steam gasification properties of cornstalk waste, Bioresource Technology 358 (2022) 127403.

[71] S. Link, S. Arvelakis, A. Paist, T. Liliedahl, C. Rosén, Effect of leaching pretreatment on the gasification of wine and vine (residue) biomass, Renewable Energy 115 (2018) 1–5.

[72] C. Yu, P. Thy, L. Wang, S.N. Anderson, J.S. VanderGheynst, S.K. Upadhyaya, B.M. Jenkins, Influence of leaching pretreatment on fuel properties of biomass, Fuel Processing Technology 128 (2014) 43–53.

[73] F. Lebendig, M. Müller, Effect of pre-treatment of herbaceous feedstocks on behavior of inorganic constituents under chemical looping gasification (CLG) conditions, Green Chem. 24 (2022) 9643–9658.

[74] K.O. Davidsson, J.G. Korsgren, J. Pettersson, U. Jäglid, The effects of fuel washing techniques on alkali release from biomass, Fuel 81 (2002) 137–142.

[75] F. Lebendig, I. Funcia, R. Pérez-Vega, M. Müller, Investigations on the Effect of Pre-Treatment of Wheat Straw on Ash-Related Issues in Chemical Looping Gasification (CLG) in Comparison with Woody Biomass, Energies 15 (2022) 3422.

[76] K. Meesters, W. Elbersen, P. van der Hoogt, H. Hristov, Biomass pre-treatment for bioenergy. Case study 5: Leaching as a biomass pre-treatment method for herbaceous biomass. Sugar cane trash and palm oil mill residues., IEA Bioenergy (2018) 1.

[77] T. Wigley, A.C. Yip, S. Pang, Pretreating biomass via demineralisation and torrefaction to improve the quality of crude pyrolysis oil, Energy 109 (2016) 481–494.

[78] Y. Zhu, Y. Niu, H. Tan, X. Wang, Short Review on the Origin and Countermeasure of Biomass Slagging in Grate Furnace, Front. Energy Res. 2 (2014).

[79] P. Sommersacher, T. Brunner, I. Obernberger, Fuel Indexes: A Novel Method for the Evaluation of Relevant Combustion Properties of New Biomass Fuels, Energy & Fuels 26 (2012) 380–390.

[80] P. Zhao, Y. Shen, S. Ge, Z. Chen, K. Yoshikawa, Clean solid biofuel production from high moisture content waste biomass employing hydrothermal treatment, Applied Energy 131 (2014) 345–367.

[81] D. Gupta, S.M. Mahajani, A. Garg, Effect of hydrothermal carbonization as pretreatment on energy recovery from food and paper wastes, Bioresource Technology 285 (2019) 121329.

[82] A. Funke, F. Ziegler, Hydrothermal carbonization of biomass: A summary and discussion of chemical mechanisms for process engineering, Biofuels, Bioprod. Bioref. 4 (2010) 160–177.

[83] K. McGaughy, M. Toufiq Reza, Hydrothermal carbonization of food waste: simplified process simulation model based on experimental results, Biomass Conv. Bioref. 8 (2018) 283–292.

[84] M.T. Reza, J. Andert, B. Wirth, D. Busch, J. Pielert, J.G. Lynam, J. Mumme, Hydrothermal Carbonization of Biomass for Energy and Crop Production, Applied Bioenergy 1 (2014).

[85] M. Sevilla, A.B. Fuertes, The production of carbon materials by hydrothermal carbonization of cellulose, Carbon 47 (2009) 2281–2289.

[86] N.D. Berge, K.S. Ro, J. Mao, J.R.V. Flora, M.A. Chappell, S. Bae, Hydrothermal carbonization of municipal waste streams, Environmental Science & Technology 45 (2011) 5696–5703.

[87] I.-H. Hwang, H. Aoyama, T. Matsuto, T. Nakagishi, T. Matsuo, Recovery of solid fuel from municipal solid waste by hydrothermal treatment using sub-critical water, Waste management (New York, N.Y.) 32 (2012) 410–416.

[88] D. Ma, Q. Feng, B. Chen, X. Cheng, K. Chen, J. Li, Insight into chlorine evolution during hydrothermal carbonization of medical waste model, Journal of Hazardous Materials 380 (2019) 120847.

[89] C.I. Aragón-Briceño, A.K. Pozarlik, E.A. Bramer, L. Niedzwiecki, H. Pawlak-Kruczek, G. Brem, Hydrothermal carbonization of wet biomass from nitrogen and phosphorus approach: A review, Renewable Energy 171 (2021) 401–415.

[90] A. Siciliano, C. Limonti, G.M. Curcio, R. Molinari, Advances in Struvite Precipitation Technologies for Nutrients Removal and Recovery from Aqueous Waste and Wastewater, Sustainability 12 (2020) 7538.

[91] T. Ngo, K.Y. Chiang, C.F. Liu, Y.H. Chang, H.-P. Wan, Hydrogen production enhancement using hot gas cleaning system combined with prepared Ni-based catalyst in biomass gasification, International Journal of Hydrogen Energy 46 (2021) 11269–11283.

[92] V. Marcantonio, M. Müller, E. Bocci, A Review of Hot Gas Cleaning Techniques for Hydrogen Chloride Removal from Biomass-Derived Syngas, Energies 14 (2021) 6519.

[93] P.R. Buchireddy, D. Peck, M. Zappi, R.M. Bricka, Catalytic Hot Gas Cleanup of Biomass Gasification Producer Gas via Steam Reforming Using Nickel-Supported Clay Minerals, Energies 14 (2021) 1875.

[94] G. Straczewski, K. Koutera, U. Gerhards, K. Garbev, H. Leibold, Development of catalytic ceramic filter candles for tar conversion, Fuel Communications 7 (2021) 100021.

[95] M. Nacken, L. Ma, K. Engelen, S. Heidenreich, G.V. Baron, Development of a Tar Reforming Catalyst for Integration in a Ceramic Filter Element and Use in Hot Gas Cleaning, Ind. Eng. Chem. Res. 46 (2007) 1945–1951.

[96] K. Engelen, Y. Zhang, G.V. Baron, Development of a Catalytic Candle Filter for One-Step Tar and Particle Removal in Biomass Gasification Gas, International Journal of Chemical Reactor Engineering 1 (2003).

[97] L.K. Wang, J.R. Taricska, Y.-T. Hung, J.E. Eldridge, K.H. Li, Wet and Dry Scrubbing, Air Pollution Control Engineering (2004) 197–305.

[98] R. Legg, Air Filters, Air Conditioning System Design (2017) 213–223.

[99] T.J. Gennrich, Gas Cleaning at High Temperatures. High Temperature Ceramic Fiber Filter Bags, Springer Science+Business Media Dordrecht (1993) 307–320.

[100] D. Peck, M. Zappi, D. Gang, J. Guillory, R. Hernandez, P. Buchireddy, Review of Porous Ceramics for Hot Gas Cleanup of Biomass Syngas Using Catalytic Ceramic Filters to Produce Green Hydrogen/Fuels/Chemicals, Energies 16 (2023) 2334.

[101] P.R. Westmoreland, D.P. Harrison, Evaluation of candidate solids for high-temperature desulfurization of low-Btu gases, Environ. Sci. Technol. 10 (1976) 659–661.

[102] E. Furimsky, M. Yumura, Solid adsorbents for removal of hydrogen sulphide from hot gas (1985).

[103] D. Vamvuka, C. Arvanitidis, D. Zachariadis, Flue Gas Desulfurization at High Temperatures: A Review, Environmental Engineering Science 21 (2004) 525–548.

[104] G.D. Focht, P.V. Ranade, D.P. Harrison, High-temperature desulfurization using zinc ferrite: Reduction and sulfidation kinetics, Chemical Engineering Science 43 (1988) 3005–3013.

[105] L.F.d. Diego, F. García-Labiano, J. Adánez, J.M. Palacios, Factors Affecting the H 2 S Reaction with Noncalcined Limestones and Half-Calcined Dolomites, Energy Fuels 13 (1999) 146–153.

[106] H. Katalambula, A. Bawagan, S. Takeda, Mineral attachment to calcium-based sorbent particles during in situ desulfurization in coal gasification processes, Fuel Processing Technology 73 (2001) 75–93.

[107] T. Akiti, K. Constant, L. Doraiswamy, T. Wheelock, Development of an advanced calcium-based sorbent for desulfurizing hot coal gas, Advances in Environmental Research 5 (2001) 31–38.

[108] H. Katalambula, M.M. Escallón, S. Takeda, Influence of Ca-Based Sorbent Particle Size on the Occurrence of Solid−Solid Reactions during in-Situ Desulfurization of the Coal-Derived Gas, Energy Fuels 15 (2001) 317–323.

[109] M. Hartman, K. Svoboda, O. Trnka, J. Čermák, Reaction between Hydrogen Sulfide and Limestone Calcines, Ind. Eng. Chem. Res. 41 (2002) 2392–2398.

[110] R. Álvarez-Rodríguez, C. Clemente-Jul, Hot gas desulphurisation with dolomite sorbent in coal gasification, Fuel 87 (2008) 3513–3521.

[111] S.V. Sotirchos, A.R. Smith, Performance of Porous CaO obtained from the decomposition of calcium-enriched bio-oil as Sorbent for SO_2 and H_2S Removal, Ind. Eng. Chem. Res. 43 (2004) 1340–1348.

[112] Y. Zeng, S. Kaytakoglu, D. Harrison, Reduced cerium oxide as an efficient and durable high temperature desulfurization sorbent, Chemical Engineering Science 55 (2000) 4893–4900.

[113] M. Flytzani-Stephanopoulos, M. Sakbodin, Z. Wang, Regenerative adsorption and removal of H_2S from hot fuel gas streams by rare earth oxides, Science (New York, N.Y.) 312 (2006) 1508–1510.

[114] V. Marcantonio, E. Bocci, J.P. Ouweltjes, L. Del Zotto, D. Monarca, Evaluation of sorbents for high temperature removal of tars, hydrogen sulphide, hydrogen chloride and ammonia from biomass-derived syngas by using Aspen Plus, International Journal of Hydrogen Energy 45 (2020) 6651–6662.

[115] A. Hatunoglu, V. Marcantonio, E. Ciro, L. Del Zotto, E. Bocci, V. Guglielmotti, A. Carlo, E. Savuto, A. Dell'Era, D.2.4. High temperature secondary sorbents selection for inorganic compounds removal and related lab scale fixed bed reactor performance. EU Blaze Project Report, L'Aquila, 2021.

[116] K. Han, X. Li, J. Qi, Y. Zhu, S. Long, H. Li, S. Niu, S. Li, Y. Xu, Synergistic effect of additives and blend on sulfur retention, on release and ash fusibility

during combustion of biomass briquettes, International Journal of Green Energy 18 (2021) 187–202.

[117] M. Gehrig, M. Wöhler, S. Pelz, J. Steinbrink, H. Thorwarth, Kaolin as additive in wood pellet combustion with several mixtures of spruce and short-rotation-coppice willow and its influence on emissions and ashes, Fuel 235 (2019) 610–616.

[118] W.A. Punjak, F. Shadman, Aluminosilicate sorbents for control of alkali vapors during coal combustion and gasification, Energy Fuels 2 (1988) 702–708.

[119] B. Dou, W. Shen, J. Gao, X. Sha, Adsorption of alkali metal vapor from high-temperature coal-derived gas by solid sorbents, Fuel Processing Technology 82 (2003) 51–60.

[120] M. Uberoi, W.A. Punjak, F. Shadman, The kinetics and mechanism of alkali removal from flue gases by solid sorbents, Progress in Energy and Combustion Science 16 (1990) 205–211.

[121] Y. Zheng, P.A. Jensen, A.D. Jensen, A kinetic study of gaseous potassium capture by coal minerals in a high temperature fixed-bed reactor, Fuel 87 (2008) 3304–3312.

[122] T. de Riese, D. Eckert, L. Hakim, S. Fendt, H. Spliethoff, Modelling the Capture of Potassium by Solid Al-Si Particles at Pulverised Fuel Conditions, Fuel 328 (2022) 125321.

[123] S. Fujita, K. Suzuki, T. Mori, Y. Shibasaki, A New Technique to Remove Hydrogen Chloride Gas at High Temperature Using Hydrogrossular, Ind. Eng. Chem. Res. 42 (2003) 1023–1027.

[124] K.F. Khaled, S.S. Abdel-Rehim, G.B. Sakr, On the corrosion inhibition of iron in hydrochloric acid solutions, Part I: Electrochemical DC and AC studies, Arabian Journal of Chemistry 5 (2012) 213–218.

[125] N. Verdone, P. de Filippis, Reaction kinetics of hydrogen chloride with sodium carbonate, Chemical Engineering Science 61 (2006) 7487–7496.

[126] Y. Li, Y. Wu, J. Gao, Study on a New Type of HCl-Removal Agent for High-Temperature Cleaning of Coal Gas, Ind. Eng. Chem. Res. 43 (2004) 1807–1811.

[127] C.-S. Chyang, Y.-L. Han, Z.-C. Zhong, Study of HCl Absorption by CaO at High Temperature, Energy & Fuels 23 (2009) 3948–3953.

[128] J. Abbasian, J.R. Wangerow, A.H. Hill, Effect of HCl on sulfidation of calcium oxide, Chemical Engineering Science 48 (1993) 2689–2695.

[129] S. Fujita, K. Suzuki, Y. Shibasaki, T. Mori, Synthesis of hydrogarnet from molten slag and its hydrogen chloride fixation performance at high temperature, J Mater Cycles Waste Manag 4 (2002) 70–76.

[130] S. Fujita, K. Suzuki, M. Ohkawa, Y. Shibasaki, T. Mori, Reaction of Hydrogrossular with Hydrogen Chloride Gas at High Temperature, Chem. Mater. 13 (2001) 2523–2527.

[131] M. Stemmler, M. Müller, D.4.1. Report on sorbents for alkali and sour gas removal. EU GreenSyngas-Project Report, Jülich, 2010.

[132] C.W. Bale, E. Bélisle, P. Chartrand, S.A. Decterov, G. Eriksson, A.E. Gheribi, K. Hack, I.-H. Jung, Y.-B. Kang, J. Melançon, A.D. Pelton, S. Petersen, C. Robelin, J. Sangster, P. Spencer, M.-A. van Ende, FactSage thermochemical software and databases, 2010–2016, Calphad 54 (2016) 35–53.

[133] G. Eriksson, K. Hack, ChemSage—A computer program for the calculation of complex chemical equilibria, Metall Mater Trans B 21 (1990) 1013–1023.

[134] E. Yazhenskikh, T. Jantzen, K. Hack, M. Müller, A new multipurpose thermodynamic database for oxide systems, Rasplavy (2019) 116–124.

[135] K.J. Wolf, A. Smeda, M. Müller, K. Hilpert, Investigations on the Influence of Additives for SO_2 Reduction during High Alkaline Biomass Combustion, Energy & Fuels 19 (2005) 820–824.

[136] M. Bläsing, M. Müller, Mass spectrometric investigations on the release of inorganic species during gasification and combustion of German hard coals, Combustion and Flame 157 (2010) 1374–1381.

[137] K.J. Wolf, M. Müller, K. Hilpert, L. Singheiser, Alkali Sorption in Second-Generation Pressurized Fluidized-Bed Combustion, Energy & Fuels 18 (2004) 1841–1850.

[138] I. Escobar, M. Müller, Alkali Removal at about 1400 °C for the Pressurized Pulverized Coal Combustion Combined Cycle. 2. Sorbents and Sorption Mechanisms, Energy & Fuels 21 (2007) 735–743.

[139] K.J. Wolf, Untersuchungen zur Freisetzung und Einbindung von Alkalimetallen bei der reduzierenden Druckwirbelschichtverbrennung. Fakultät für Maschinenwesen. RWTH Aachen University, PhD-Thesis, Aachen, 2003.

[140] W. van der Kemp, J.G. Blok, P.R. van der Linde, H. Oonk, A. Schuijff, M.L. Verdonk, Binary alkaline earth oxide mixtures: Estimation of the excess thermodynamic properties and calculation of the phase diagrams, Calphad 18 (1994) 255–267.

[141] G. Brauer (Ed.), Handbuch der präparativen anorganischen Chemie. In drei Bänden, Enke, Stuttgart, 1978.

[142] S.N. Lunawat, Mixed metal oxide and mixed metal oxide supported -ion exchanged zeolite sorbents for hot gas desulfurization. University of Alberta Libraries, Master-Thesis, Alberta, 2012.

[143] M. Bläsing, M. Zini, M. Müller, Influence of Feedstock on the Release of Potassium, Sodium, Chlorine, Sulfur, and Phosphorus Species during Gasification of Wood and Biomass Shells, Energy & Fuels 27 (2013) 1439–1445.

[144] M. Bläsing, T. Melchior, M. Müller, Influence of the Temperature on the Release of Inorganic Species during High-Temperature Gasification of Hard Coal, Energy & Fuels 24 (2010) 4153–4160.

[145] M. Bläsing, T. Melchior, M. Müller, Influence of temperature on the release of inorganic species during high temperature gasification of Rhenish lignite, Fuel Processing Technology 92 (2011) 511–516.

[146] B. Zhang, B.K. Biswal, J. Zhang, R. Balasubramanian, Hydrothermal Treatment of Biomass Feedstocks for Sustainable Production of Chemicals,

Fuels, and Materials: Progress and Perspectives, Chemical reviews 123 (2023) 7193–7294.

[147] Z. Zhang, J. Yang, J. Qian, Y. Zhao, T. Wang, Y. Zhai, Biowaste hydrothermal carbonization for hydrochar valorization: Skeleton structure, conversion pathways and clean biofuel applications, Bioresource Technology 324 (2021) 124686.

[148] K. Simpkins, Internet document. Toward more sustainable wine: Scientists can now track sulfur from grapes to streams. Accessed 16.12.2023. https://www.colorado.edu/today/2022/05/24/toward-more-sustainable-wine-scientists-can-now-track-sulfur-grapes-streams (16.12.2023).

[149] A.D. Mayernick, R. Li, K.M. Dooley, M.J. Janik, Energetics and Mechanism for H_2S Adsorption by Ceria-Lanthanide Mixed Oxides: Implications for the Desulfurization of Biomass Gasifier Effluents, J. Phys. Chem. C 115 (2011) 24178–24188.

[150] D.R. Mullins, T.S. McDonald, Adsorption and reaction of hydrogen sulfide on thin-film cerium oxide, Surface Science 601 (2007) 4931–4938.

[151] J. Sitzmann, D.2.4. Realization and optimization of catalytic ceramic hot gas system. EU GICO-Project Report (restricted), Nürnberg, 2023.

Appendix

Table A.1: Adjustments of the MBMS.

Parameter	Value
Scan time requested	0.5 s
Electron Emission Voltage	-50 V
Electron Emission Current	0.8 mA
Ion Region	14 V
Extractor	-50 V
Lens 1/3	-219 V
Lens 2	26 V
Multiplier Voltage	1300-1400 V
Dynode Voltage	5000 V
Dynode Polarity	negative voltage

Figure A.1: Original shape of the filter candles used in the exposure experiments. Ca-Mg silicate fiber filter candle (l.) and Al-oxide silicate fiber filter candle (r.).

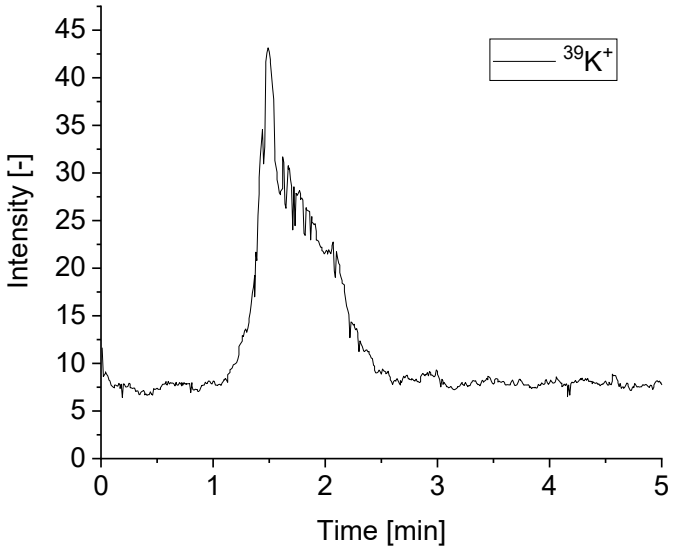

Figure A.2: Intensity-time profiles of $^{39}K^+$ (m/z = 39 of a CaO-Green Waste mixture at 650 °C in 20 % H_2O and 80 % He ($\dot{V}_{tot}$ = 4 l/min).

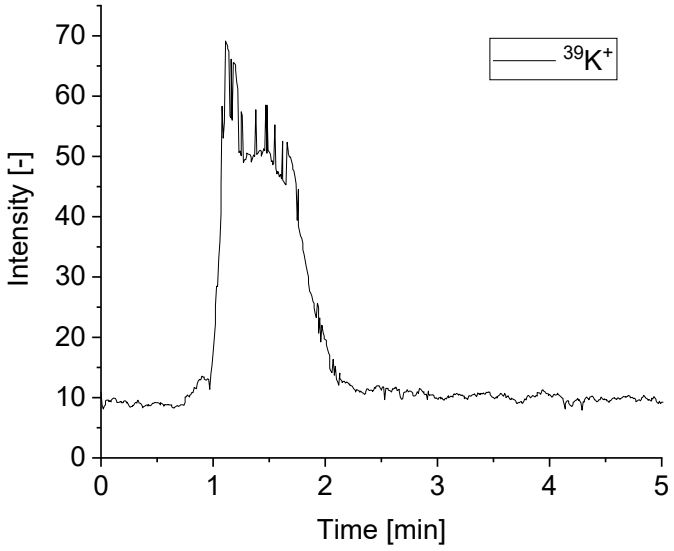

Figure A.3: Intensity-time profiles of $^{39}K^+$ (m/z = 39) of a CaO-OFMSW mixture at 650 °C in 20 % H_2O and 80 % He ($\dot{V}_{tot}$ = 4 l/min).

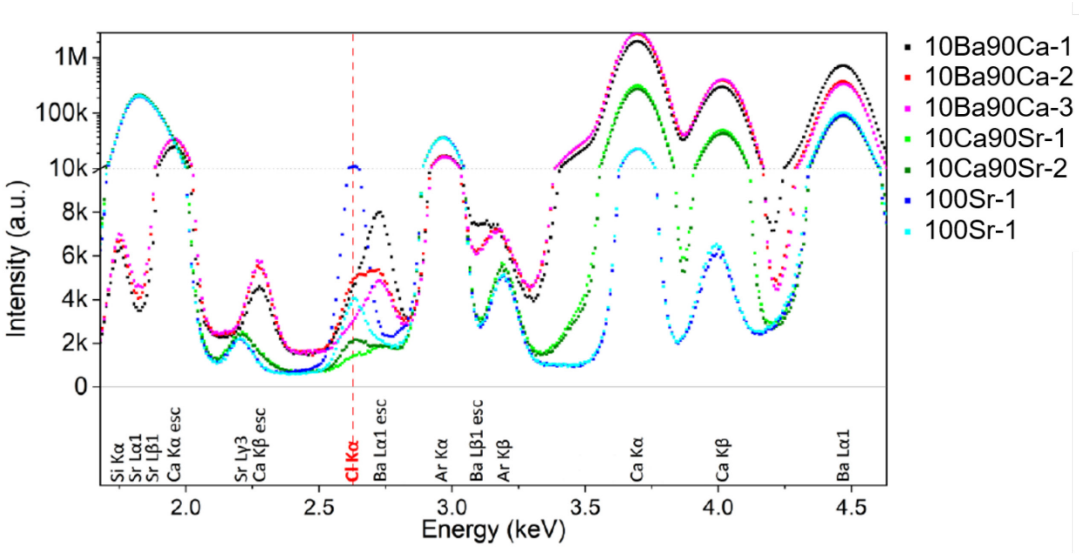

Figure A.4: EDXRF spectra, powder samples placed on 3.6 µm Mylar foil

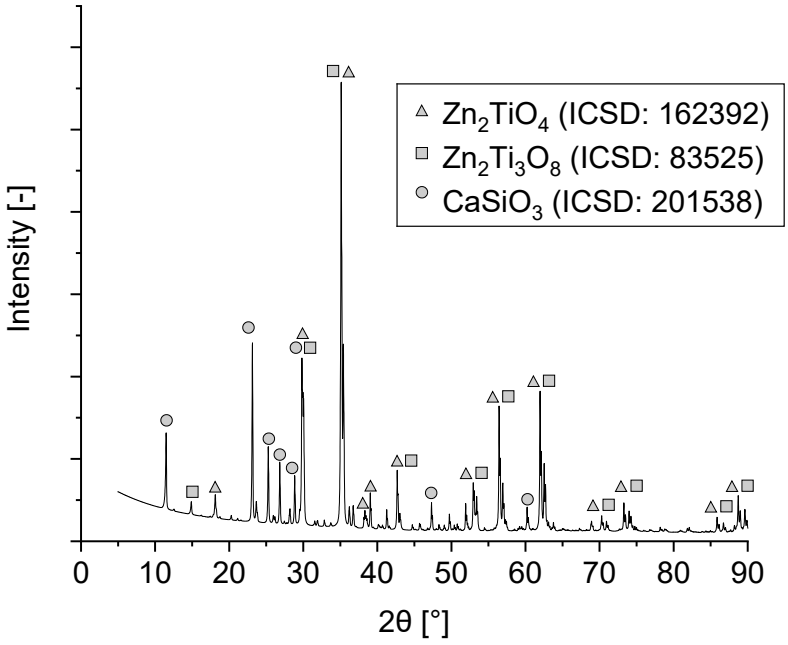

Figure A.5: XRD spectrum of Ca-Mg silicate fiber filter candle and Zn_2TiO_4 after exposure.

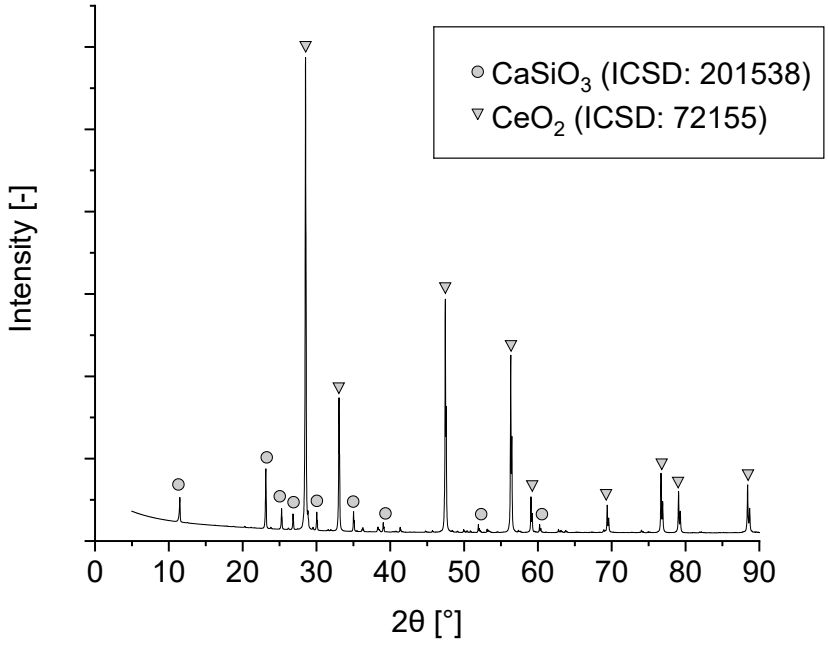

Figure A.6: XRD spectrum of Ca-Mg silicate fiber filter candle and Ce_2O_3 after exposure.

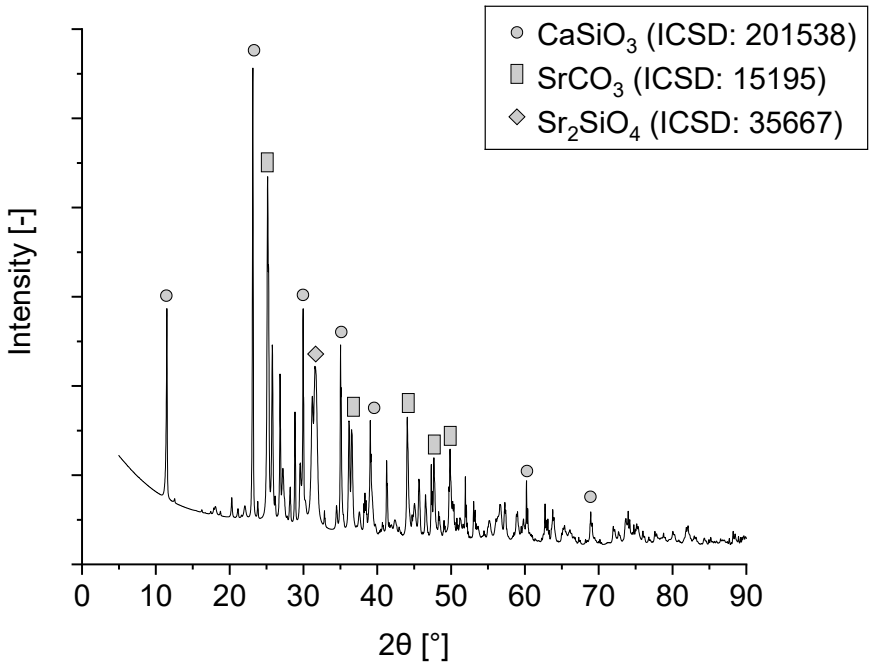

Figure A.7: XRD spectrum of Ca-Mg silicate fiber filter candle and SrO after exposure.

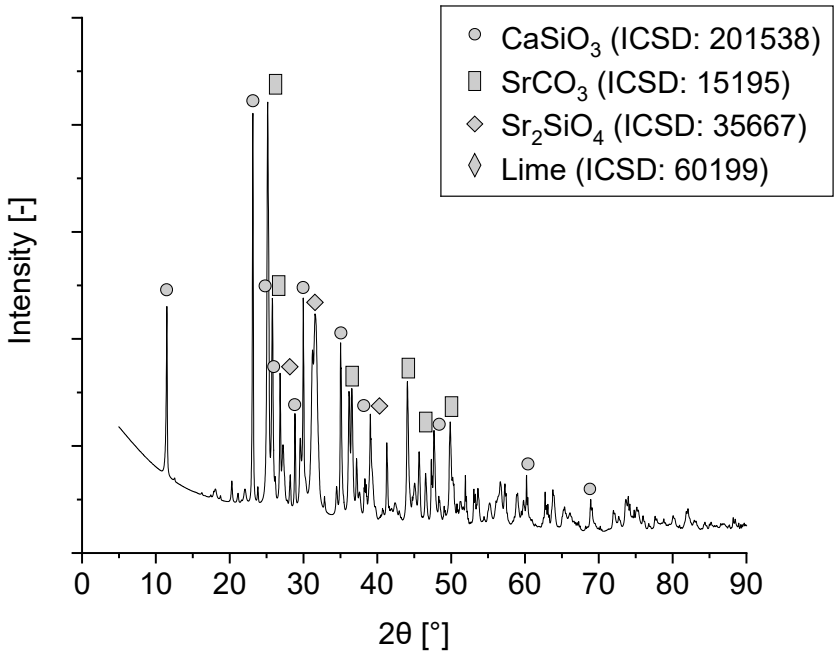

Figure A.8: XRD spectrum of Ca-Mg silicate fiber filter candle and 90Sr10Ca after exposure.

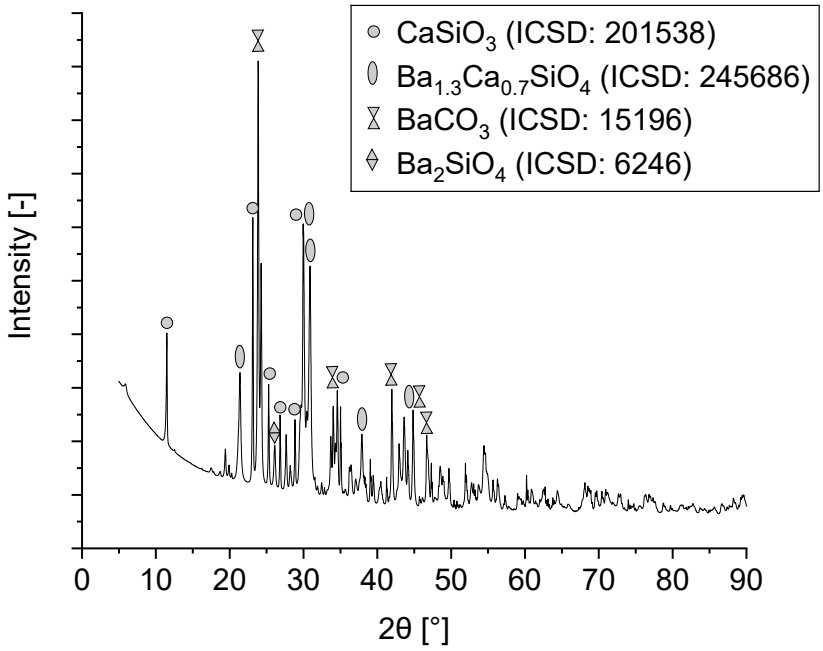

Figure A.9: XRD spectrum of Ca-Mg silicate fiber filter candle and BaO after exposure.

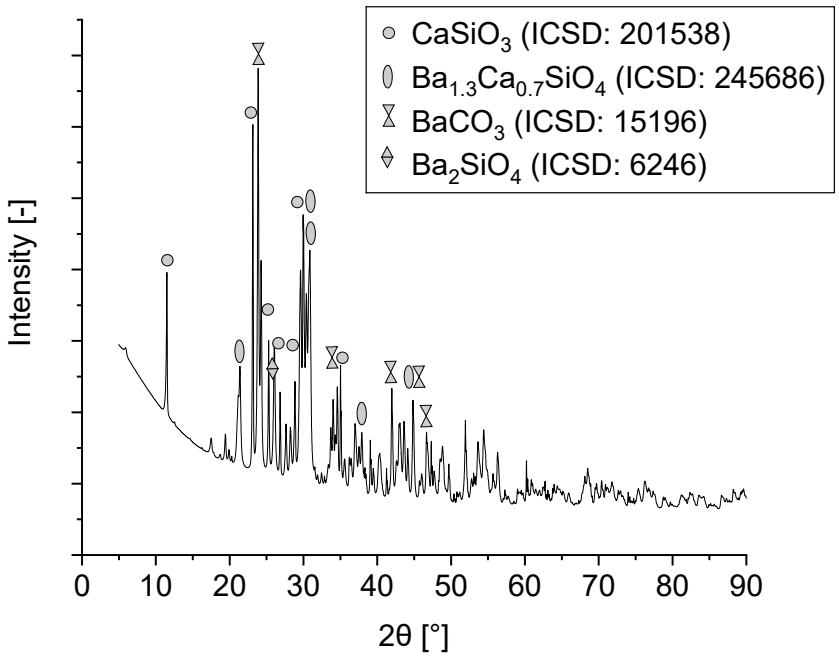

Figure A.10: XRD spectrum of Ca-Mg silicate fiber filter candle and 90Ba10Ca after exposure.

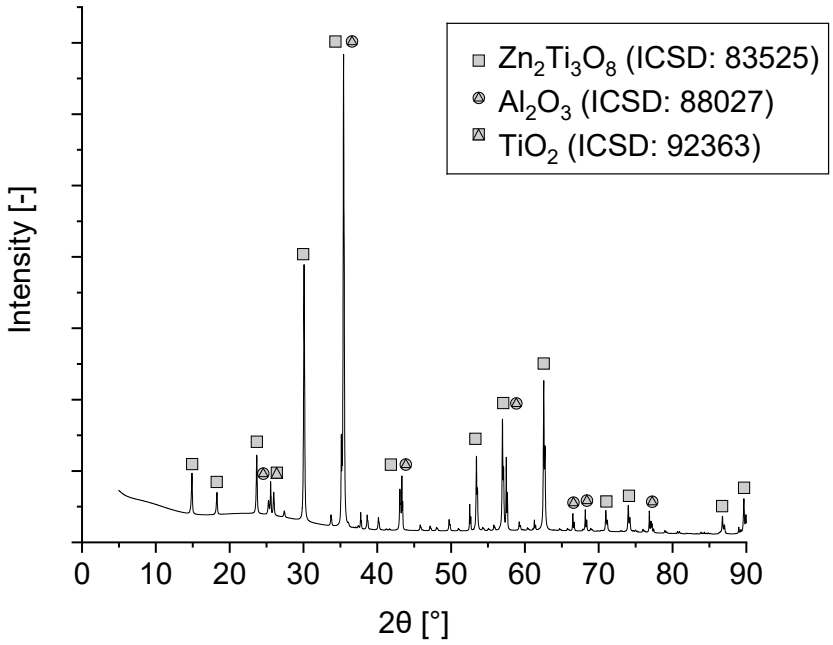

Figure A.11: XRD spectrum of Al-oxide silicate fiber filter candle and Zn_2TiO_4 after exposure.

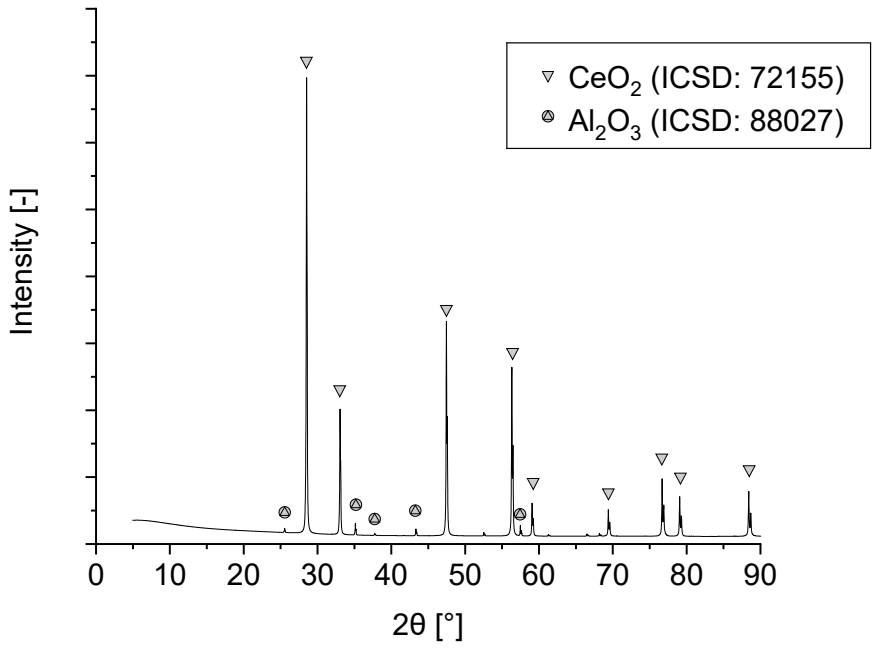

Figure A.12: XRD spectrum of Al-oxide silicate fiber filter candle and Ce_2O_3 after exposure.

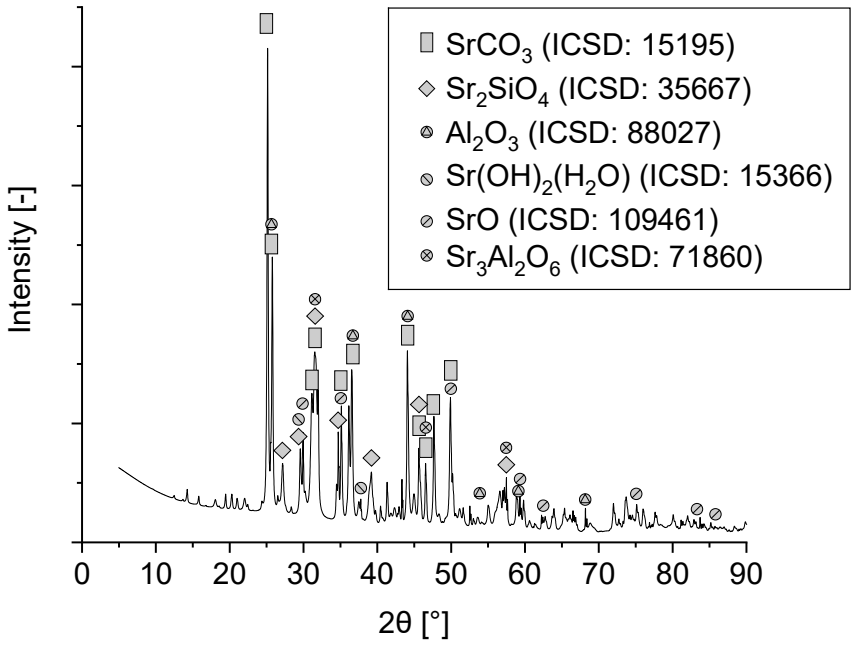

Figure A.13: XRD spectrum of Al-oxide silicate fiber filter candle and SrO after exposure.

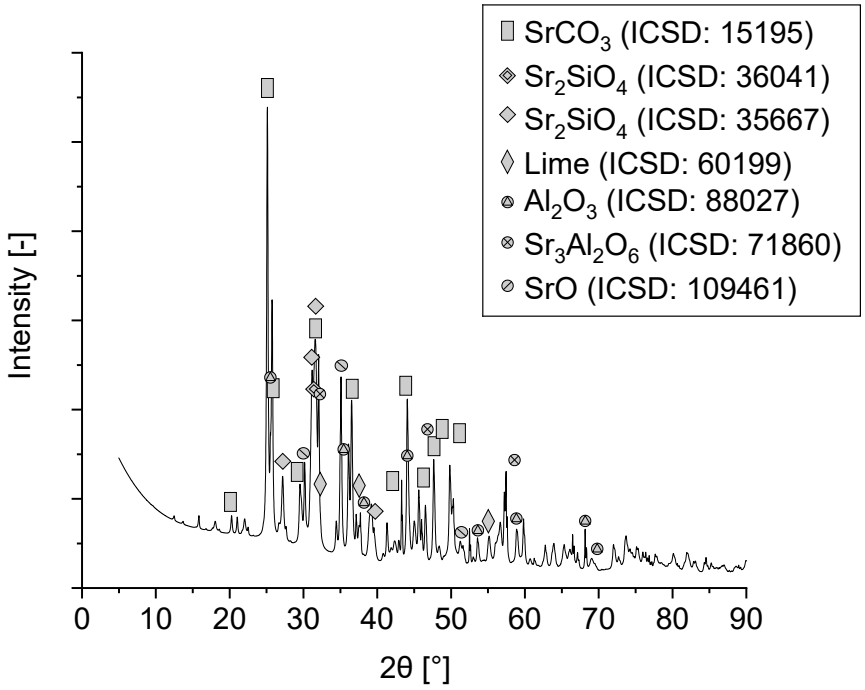

Figure A.14: XRD spectrum of Al-oxide silicate fiber filter candle and 90Sr10Ca after exposure.

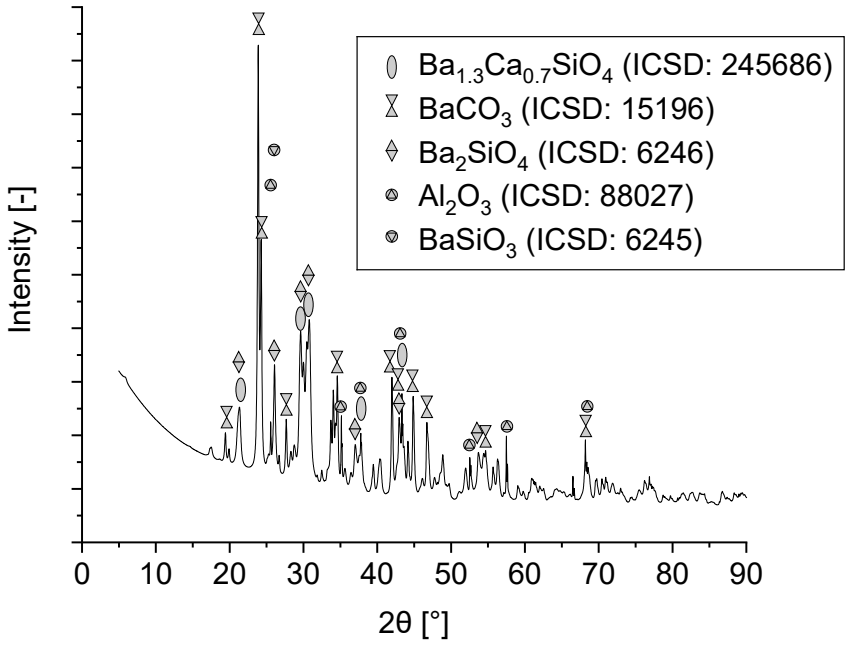

Figure A.15: XRD spectrum of Al-oxide silicate fiber filter candle and BaO after exposure.

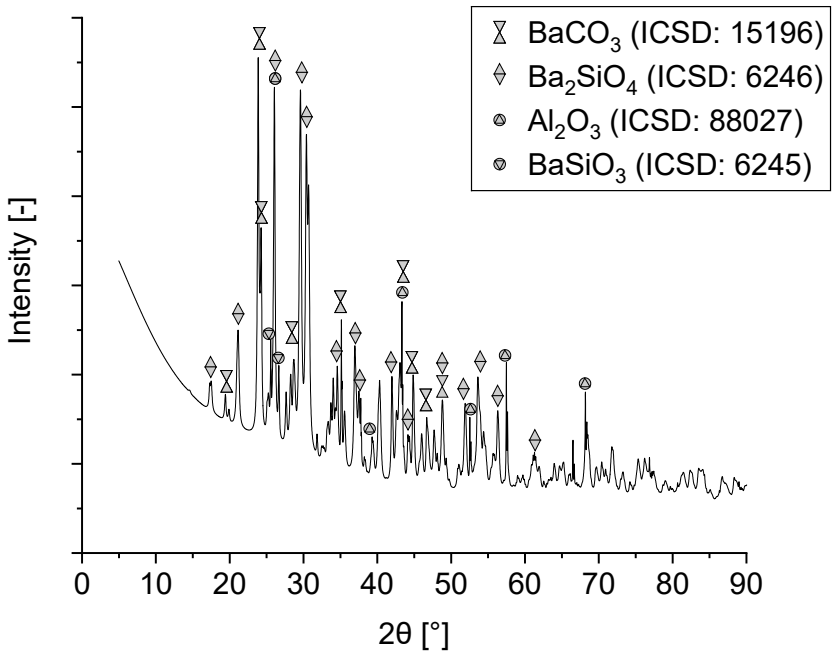

Figure A.16: XRD spectrum of Al-oxide silicate fiber filter candle and 90Ba10Ca after exposure.

Acknowledgements

Dear readers,

I am incredibly grateful to finally share my dissertation with all of you. This research project, which was a years-long labor of love, would not have been possible without the help and support of many people, and I wanted to take a moment to express my appreciation.

Firstly, I want to thank PD Dr. Michael Müller, for his unwavering guidance throughout the entire research process. His expertise and insightful feedback helped shape this dissertation into its final form. Especially I want to thank him for his trust and the high degree of freedom during my PhD.

I am also grateful for the support of my colleagues and peers, who have provided invaluable feedback, advice, and inspiration. In particular I want to thank the Thermochemistry Group: Darya Ewaznezhad Fard, Patrick Schuster, Amedeo Morsa, Engy Zain, Marcel Siepmann, Jeraldine Lastam, Viktoria Keller, Jia Qi, Shivani Gonde, Dr. Rhys Jacob, Ralf Küppers, Inge Dreger, Dr. Elena Yazhenskikh, and Dr. Dmitry Sergeev. Their expertise helped me to think more deeply and comprehensively about my research topic and to refine my writing.

I also want to thank Dr. Egbert Wessel, Dr. Daniel Grüner, Jörg Bartsch, Max Borzikov, Christoph Bütow, Mirko Ziegner, Manuel Hucko, Ramadan Sanli, Katrin Leipertz, Florian Lebendig, and Volker Gutzeit for the scientific and technical support.

Special thanks also go to Dr. Jürgen Sitzmann, with whom I had many interesting discussions on the practical application of our hot gas cleaning concept. Your willingness to make our concept a reality has filled me with pride.

I want to express my love and appreciation to my family and friends, who have supported me throughout my academic journey and have been an endless source of encouragement and motivation. Your encouragement reminded me to keep pressing forward, even when the research felt challenging or overwhelming.

Thank you to everyone who has played a role in the creation of this dissertation. I am honored and humbled to be able to share this work with you all.

Sincerely,

Markus Alexander Kopsch